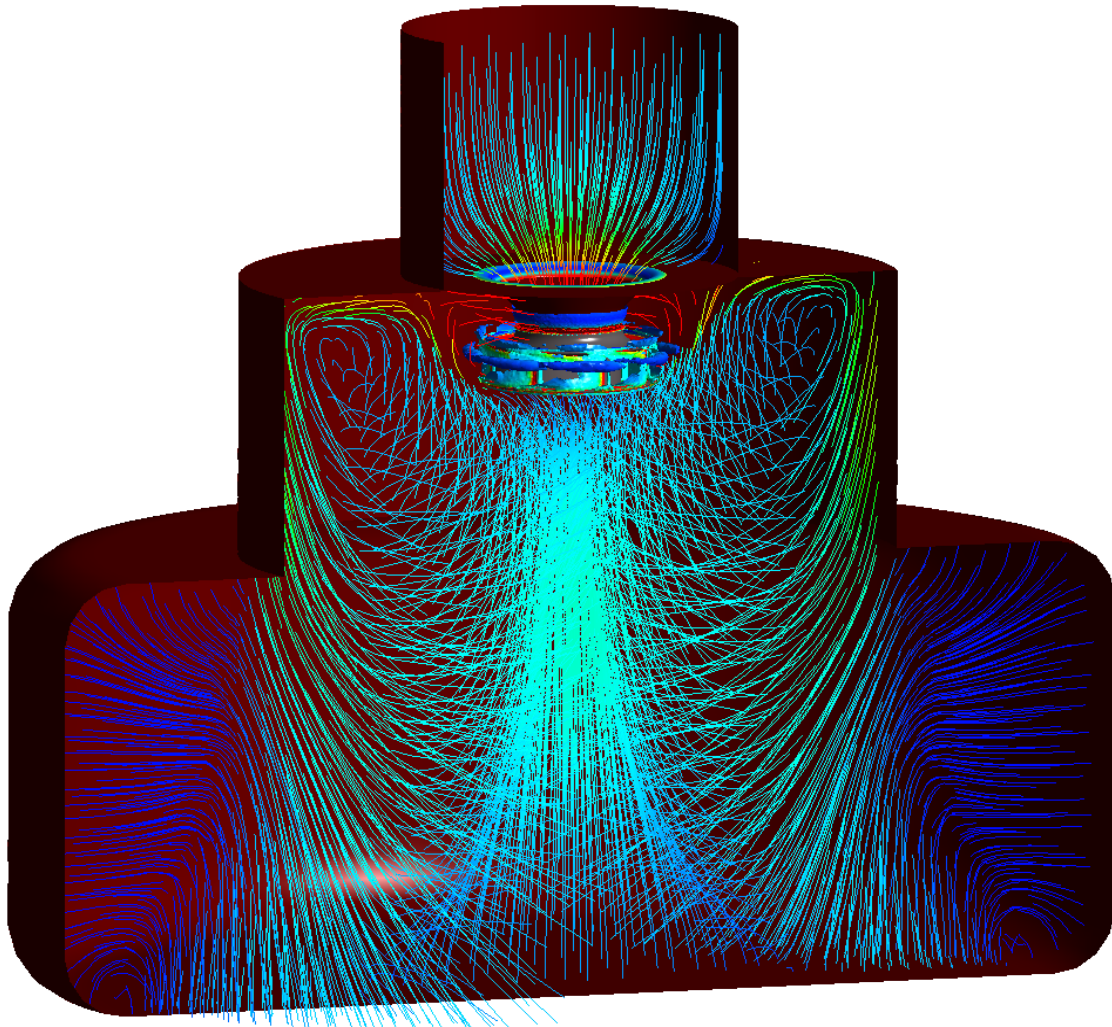




CHALMERS
UNIVERSITY OF TECHNOLOGY



Numerical Estimation of the Aerodynamic Tones Radiated From a Centrifugal Fan

An Aeroacoustic Study with Computational Fluid Dynamics

Master's thesis in Applied Mechanics

Erik Sjösvärd

Department of Applied Mechanics
CHALMERS UNIVERSITY OF TECHNOLOGY
Gothenburg, Sweden 2016

MASTER'S THESIS IN APPLIED MECHANICS

**Numerical Estimation of the Aerodynamic
Tones Radiated From a Centrifugal Fan**

An Aeroacoustic Study with Computational Fluid Dynamics

ERIK SJÖSVÄRD

Department of Applied Mechanics
Division of Fluid Mechanics
CHALMERS UNIVERSITY OF TECHNOLOGY
Gothenburg, Sweden 2016

Numerical Estimation of the Aerodynamic Tones Radiated From a Centrifugal Fan
An Aeroacoustic Study with Computational Fluid Dynamics
ERIK SJÖSVÄRD

© ERIK SJÖSVÄRD, 2016.

Supervisors: Marcus Berggren, Federico Ghirelli and Jonas Klein, Semcon
Examiner: Professor Lars Davidsson, Applied Mechanics

Master's Thesis 2016:56
ISSN 1652-8557
Department of Applied Mechanics
Division of Fluid Mechanics
Chalmers University of Technology
SE-412 96 Gothenburg
Telephone +46 31 772 1000

Cover: Isosurface showing turbulent structures through the Q invariant at 10000 [$1/s^2$]
coloured by velocity curl in range 200 – 2000 [$1/s$], and streamlines coloured by velocity
magnitude in range 0 – 10 [m/s].

Printed by [Chalmers Reproservice]
Gothenburg, Sweden 2016

Numerical Estimation of the Aerodynamic Tones Radiated From a Centrifugal Fan
An Aeroacoustic Study with Computational Fluid Dynamics

Erik Sjösvärd

Department of Applied Mechanics

Division of Fluid Mechanics

Chalmers University of Technology

Abstract

Different types of sounds are always present in everyday life. When the sound is too loud or has annoying frequencies serious health issues can arise, and minimisation of sound is therefore always of great interest. Centrifugal fans are commonly used in ventilation applications and induce a high level of flow-induced sound, which fan designers are constantly trying to reduce. By performing aeroacoustical simulations, different fan models can be evaluated at an early design stage resulting in a quicker and more cost efficient development.

In the current study, a turbulent unsteady flow through a three dimensional centrifugal fan has been simulated with the commercial Computational Fluid Dynamics (CFD) software FLUENT. The pressure field from the unsteady simulation was then coupled with the acoustic analogy of Ffowcs William & Hawkings (FW-H) to propagate the radiated sound into the far field. Both the aerodynamic and acoustical properties were investigated by changing different model parameters and comparing with experimental measurements. The parameter study included: comparison between a full domain model and a sector model, two turbulence models – the realizable $k - \varepsilon$ and the $k - \omega$ SST model, two pressure discretizations – PRESTO and 2^{nd} order Central Difference (CD) scheme and finally a comparison between compressible and incompressible flow.

The numerical results show that the aerodynamic properties correspond well to experimental measurements for all numerical cases. By using a full domain model, the sound pressure level at the blade passage frequency can be predicted within 0.7 [dB] from the experimental measurement, and by using a sector model the same tone is over predicted by approximately 10 [dB]. The higher harmonics are not captured by the full domain model whereas they are predicted with relative accuracy for the sector model. The radiated sound is only partially affected by changing turbulence model, whereas pressure discretization and incompressible flow assumption significantly alter the characteristics of the radiated sound.

Keywords: Aeroacoustics, FW-H, Centrifugal Fan, URANS, Computational Fluid Dynamics, Sound Prediction, FLUENT, Sector Domain

Preface

This study was performed during the spring of 2016 and represents the final step in obtaining a Master's Degree in Applied Mechanics at Chalmers University of Technology. The study has been carried out for the Swedish ventilation manufacturer Swegon in collaboration with the engineering consultancy company SEMCON, at the Simulation Department in Gothenburg.

The industrial supervisors were Marcus Berggren and Federico Ghirelli for assistance within Computational Fluid Dynamics, and Jonas Klein for assistance within acoustics. The examiner and academic supervisor has been Professor Lars Davidson, the Head of the Fluid Mechanics Division at the department of Applied Mechanics.

Acknowledgements

First of all, I would like to express my gratitude to Swegon for the opportunity to be part of such an interesting project with such a clear link to reality and actual engineering issues. Many thanks to Marcus Berggren, Federico Ghirelli and Jonas Klein who all have shown great knowledge and patience with all my questions ranging from small and insignificant to large and important. I wish also, to thank the employees at the Simulation department at SEMCON for being very welcoming and supportive, making me feel as a part of the group from week one. At Chalmers, I wish to thank Professor Lars Davidson for sharing his valuable knowledge within fluid dynamics. I also wish to give Doctor Huadong Yao at the Division of Fluid Mechanics a special thanks for his many hours of assistance within aeroacoustics.

Erik Sjösvärd, Gothenburg, June 2016

Nomenclature

Greek Symbols

β^*	Modelling constant for the $k - \omega$ turbulence model
δ_{ij}	Dirac delta function
ε	Turbulent dissipation rate
ϵ_{ijk}	Permutation symbol
η	Lagrangian coordinate system following a surface surrounding a sound source
γ	Heat capacity ratio
λ	Wave length
μ	Dynamic viscosity
ν	Kinematic viscosity
ν_t	Turbulent viscosity
ω	Specific dissipation rate
ω_i	Vorticity in tensor notation
ρ	Density
ρ_0	Constant reference density
σ^*	Modelling constant for the $k - \omega$ turbulence model
σ_ϵ	Modelling constant for the $k - \epsilon$ turbulence model
σ_k	Modelling constant for the $k - \epsilon$ turbulence model
σ_{ji}	Compressive stress tensor
τ	Retarded time, $\tau = t - R/a_0$
τ_{ij}	Reynolds stress tensor, $-\overline{u'_i u'_j}$
τ_w	Wall shear stress
ϕ	Angle between two element sides in ANSA

Roman Symbols

a	Speed of sound
a_0	Constant reference speed of sound
C	CFL number

C_μ	Modelling constant for the $k - \varepsilon$ turbulence model
$c_{\varepsilon,1}$	Modelling constant for the $k - \varepsilon$ turbulence model
$c_{\varepsilon,2}$	Modelling constant for the $k - \varepsilon$ turbulence model
e	Internal energy
e_{ij}	Viscous stress tensor
F	Dipole sound source
F_l	Blending factor in the $k - \omega$ SST model
f	Frequency, region surface in Ffowcs-William & Hawkings equation
f_i	External load vector in tensor notation
f_s	Sampling frequency
f_{max}	Highest frequency in sample
Δf	Frequency resolution
H	Heaviside function
I	Turbulent intensity
k	Thermal conductivity, turbulent kinetic energy
L	Characteristic length of the flow
L_p	Sound pressure level
L_s	Characteristic length of sound source
L_w	Sound power level
ℓ	Turbulent length scale
M	Mach number
M_i	Mach number of integration surface, $M_i = \frac{v_i}{a_0}$
M_r	Component of M_i in direction of r_i , $M_r = M_i \cdot r_i$
\dot{m}	Mass flow rate
n_i	Unit vector in wall normal direction
P_{Mech}	Mechanical energy level
P_{Sound}	Sound energy level
p	Pressure
\bar{p}	Averaged pressure
p'	Fluctuating pressure
p'_L	Pressure fluctuations from loading noise
p'_T	Pressure Fluctuations from thickness noise
p_{ref}	Audible pressure at 1000 Hz
p_{rms}	Root mean square of pressure
Q	Monopole sound source, volume flow rate

R	Specific gas constant, distance between sound source and far-field observer
r_i	Unit vector in radiation direction
S_{ij}	Strain rate tensor or rate of deformation tensor
\overline{S}_{ij}	Averaged strain rate tensor or rate of deformation tensor
T	Temperature
T_{ij}	Lighthill's stress tensor
T_s	Sample time
t	Time
Δt	Time step
U	Characteristic velocity of the flow
u_i	Instantaneous velocity component in tensor notation
u_n	Fluid velocity normal to integration surface
u_p	First wall normal cell velocity
\overline{u}_i	Averaged velocity component in tensor notation
u'_i	Fluctuating velocity component in tensor notation
v_i	Surface velocity in x_i direction
v_n	Surface velocity normal to integration surface
W_d	Dipole sound power
W_m	Monopole sound power
W_q	Quadrupole sound power
W_{ref}	Reference acoustic power
x_i	Position vector in tensor notation
Δx	Grid size
y	Wall normal distance
y^+	Dimensionless wall distance
Δy_p	First wall normal cell distance

Other Symbols

\square^2	d'Alembertian operator
-------------	------------------------

Abbreviations

BPF	Blade Passage Frequency
BSL	Baseline
CAA	Computational Aeroacoustics
CAD	Computer Aided Design

CD	Central Difference
CFD	Computational Fluid Dynamics
CFL	Courant Freidrich-Lewy
DES	Detached Eddy Simulation
DNS	Direct Numerical Simulation
FFT	Fast Fourier Transform
FW-H	Ffowcs William & Hawkings
LES	Large Eddy Simulation
MRF	Moving Reference Frame
PANS	Partially Averaged Navier Stokes
PID	Part Identity
PRESTO	PREssure STaggering Option
RMSE	Root Mean Square Error
SAS	Scale Adaptive Simulations
SLS	Selective Laser Sintering
SPL	Sound Pressure Level
SST	Shear Stress Transport
URANS	Unsteady Reynolds Averaged Navier Stokes

Contents

Nomenclature	ix
1 Introduction	1
1.1 Background	1
1.2 Objectives	2
1.3 Delimitations	2
2 Theory of Fluid Mechanics	3
2.1 Governing Equations	3
2.2 Dimensionless Numbers	4
2.2.1 Reynolds Number	4
2.2.2 Mach Number	5
2.3 Turbulence Modelling	5
2.3.1 Reynolds Averaged Navier Stokes	5
2.3.2 Turbulence Models	6
2.3.2.1 k - ϵ Models	6
2.3.2.2 k - ω Models	7
2.4 Computational Fluid Dynamics	8
2.4.1 Wall Treatment	8
2.4.2 Courant–Friedrich–Lewy Number	9
2.4.3 Moving Mesh Techniques	9
2.4.3.1 Moving Reference Frame	9
2.4.3.2 Sliding Mesh	10
3 Theory of Acoustics	11
3.1 General Acoustics	11
3.1.1 Sound Levels	12
3.1.2 Sound Sources	12
3.1.2.1 Monopole	12
3.1.2.2 Dipole	12
3.1.2.3 Quadrupole	13
3.1.3 Aerodynamic Sound	13
3.2 Computational Aeroacoustics	14
3.2.1 Direct Method	14
3.2.2 Hybrid Method	14
3.2.2.1 Lighthill’s Acoustic Analogy	15
3.2.2.2 Ffowcs Williams & Hawking’s Acoustic Analogy	16
3.3 Signal Treatment	17
3.3.1 Fourier Transform	17
3.3.2 Sampling Rate	17

4	Methodology	19
4.1	Softwares	19
4.2	Creation of the Computational Domain	19
4.2.1	Computational Domian	20
4.2.2	Mesh Generation	21
4.3	Numerical Simulation	23
4.3.1	Aerodynamics	24
4.3.1.1	Pressure Velocity Coupling	24
4.3.1.2	Time Step	24
4.3.1.3	Discretization	25
4.3.1.4	Turbulence models	26
4.3.1.5	Boundary Conditions	26
4.3.1.6	Turbulence Boundary Conditions	26
4.3.1.7	Wall Treatment	26
4.3.1.8	Convergence	27
4.3.1.9	Aerodynamic Evaluation	27
4.3.1.10	Summary of Cases	28
4.3.2	Acoustic Prediction	28
4.4	Post-Processing	30
4.4.1	Contour Plots	31
4.4.2	Frequency Resolution	31
5	Results	33
5.1	Aerodynamic Results	33
5.1.1	Time Averaged Pressure - Case A, Case B and Case D1	35
5.2	Acoustic Results	39
5.2.1	Comparison Between the Numerical Grids	39
5.2.2	Comparison Between Case D1 and Case D2	42
5.2.3	Comparison Between Case E1 and Case E2	45
5.2.4	Comparison Between Case F1 and Case F2	48
5.2.5	Pressure Discretization	51
5.2.6	Compressibility	54
6	Discussion	57
6.1	Methodology Related	57
6.1.1	Sector Model	57
6.1.2	Pressure Sampling on Parallel Processors	58
6.2	Results Related	58
6.2.1	Aerodynamic	58
6.2.1.1	Time Averaged Pressure	59
6.2.2	Acoustic	60
6.2.2.1	Full Domain Models and Sector Model	60
6.2.2.2	Turbulence Models	62
6.2.2.3	Pressure Discretization	62
6.2.2.4	Compressibility	63
6.3	Sources Of Error	63
7	Conclusion	65
8	Future Work	67

Bibliography	69
A Appendix 1	I
A.1 Flow Settings for Compressible Flow	I
A.2 Flow Settings for Incompressible Flow	II
A.3 Closure Coefficients	II

1

Introduction

In this study the aeroacoustical effects of a centrifugal fan are investigated through Computational fluid dynamics. The following chapter gives an introduction to why such a study is relevant, what the specific objectives are and what lies beyond the scope of the current study.

1.1 Background

Centrifugal fans are extensively used in ventilation systems where they are used to supply industries and office facilities with a fresh supply of air. During operation, the centrifugal fan gives rise to high levels of sound, where the main sound contributor is aerodynamic sound [1].

Aerodynamic sound consists of two sound types, a tonal and a broadband part. For centrifugal fans, the tones are produced by the centrifugal fan displacing air, or by the forces exerted by the centrifugal fan on the air and produces clear tones at the blade passage frequency and its higher harmonics [1]. The broadband sound is mainly produced by turbulence interacting with the centrifugal fan, e.g. boundary layers, vortex shedding and general turbulent fluctuating quantities in the flow, and results in multiple frequencies of equal magnitude [2].

The sound radiated from ventilation fans can propagate throughout the ventilation system and disturb the perceivers on the other side of the duct. By keeping the sound levels at a minimum, a high competitive edge towards other fan producers can be established. At Swegon (a Swedish ventilation manufacturer), the methodology to obtain the sound characteristics of their fans involves 3D-printing a fan prototype using Selective Laser Sintering (SLS), and testing the printed prototype in a sound test facility. This methodology is time consuming and costly, and by performing aeroacoustical simulations the sound characteristics of different fan models could be obtained earlier in the development process resulting in both quicker and cheaper development.

The field of computational aeroacoustics can generally be divided into two different approaches, the *Direct Approach* and the *Hybrid Approach*. The direct approach is considered the most accurate approach and resolves all the aerodynamic and acoustic variables from the sound source up to the far field observer, which requires large computational resources [3]. In the hybrid approach, the sound is decoupled from the flow field such that the near field flow can be solved without considering the acoustics of the far field. The obtained flow variables then serve as input in a separate computation regarding the far field acoustics [3]. Since only the near field needs to be resolved accurately the computational cost for the hybrid approach is substantially lower compared to the direct approach.

Since the turbulence is a major contributor to the aerodynamic sound, the turbulence must be accurately modelled for complete resolution of the acoustic field. Turbulence is generally treated through techniques such as *Direct Numerical Simulation* (DNS), *Large Eddy Simulation* (LES), *Detached Eddy Simulation* (DES) or *Unsteady Reynolds Averaged Navier Stokes* (URANS) [3]. The techniques are mentioned in order of computational cost and accuracy with the most accurate and costly first. In practical applications regarding solid boundaries, DNS and LES are usually not feasible due to the high degree of spatial resolution required close to the solid boundaries, making DES and URANS the only affordable techniques [4]. URANS is by far the cheapest method for dealing with turbulence, but is usually deemed to blunt for aeroacoustics. This is due to the strict empirical limits on the flow physics that are not resolved by increasing the spatial or temporal resolution [3]. However, there are multiple studies [5, 6, 7], indicating that the large scale fluctuations related to the tonal sounds at the blade passage frequency and the higher harmonics can be captured by the means of URANS.

1.2 Objectives

The main objective for this study is to create a basis of an industrialised methodology regarding computational aeroacoustics and centrifugal fans for Swegon. The goal is to predict the fundamental frequencies and approximate sound pressure levels of those frequencies up to 1700 [Hz]. To reach the goal,

- Full domain models will be compared to sector models.
- Turbulence will be treated through different models and the effect will be studied.
- Different discretization schemes for pressure will be used.
- The acoustical effect of treating the flow as incompressible will be investigated.
- Various surfaces of the centrifugal fan will be used as sound sources.

1.3 Delimitations

- **Time**
 - To be able to complete the project, knowledge within both computational fluid dynamics and acoustics is needed. It is performed by one student during 20 weeks which can be considered a short time for a project of this magnitude.
- **Computational Resources**
 - In industry, the time and computational resources are limited, and the simulation methodology must be adapted to this constraint. Therefore the turbulence will be treated solely through URANS turbulence models.

2

Theory of Fluid Mechanics

The following chapter presents a theoretical background regarding fluid mechanics with a further continuation into the governing equations, dimensionless numbers, turbulence modelling and computational fluid dynamics relevant for this study.

2.1 Governing Equations

Viscous fluids can be described through coupled equations for mass, motion and energy which denotes the governing equations [8]. Conservation of mass or the continuity equation, ensures that the mass flow entering a system equals to the mass flow leaving and can be written as [8]

$$\frac{d\rho}{dt} + \rho \frac{\partial u_i}{\partial x_i} = \frac{\partial \rho}{\partial t} + \frac{\partial(\rho u_i)}{\partial x_i} = 0 \quad (2.1)$$

The equation of motion or the Navier Stokes equation ensures an equilibrium between motion and forces and can be written as [8]

$$\frac{\partial(\rho u_i)}{\partial t} + \frac{\partial(\rho u_i u_j)}{\partial x_j} = \frac{\partial \sigma_{ji}}{\partial x_j} + \rho f_i \quad (2.2)$$

in which σ_{ji} is the compressive stress tensor consisting of the pressure p , and the viscous stress tensor e_{ij} , as

$$\sigma_{ji} = -p\delta_{ij} + \underbrace{2\mu S_{ij} - \frac{2}{3}\mu S_{ij}\delta_{ij}}_{e_{ij}} \quad (2.3)$$

where

$$S_{ij} = \frac{1}{2} \left(\frac{\partial u_i}{\partial x_j} + \frac{\partial u_j}{\partial x_i} \right)$$

and denotes the rate of deformation or the strain rate tensor [8].

The energy equation is derived from the first law of thermodynamics and relates internal energy, velocity, temperature and pressure and can be written as [8]

$$\frac{d(\rho e)}{dt} = -p \frac{\partial u_i}{\partial x_i} + 2\mu S_{ij} S_{ij} - \frac{2}{3}\mu S_{kk} S_{ii} + \frac{\partial}{\partial x_i} \left(k \frac{\partial T}{\partial x_i} \right) \quad (2.4)$$

So far, there are seven unknowns: four thermodynamical quantities (pressure, density, internal energy and temperature) plus the three velocity components, but only five equations. By assuming thermodynamic equilibrium, the thermodynamic variables are related through the equation of state such that [9]

$$p = p(\rho, T) \qquad e = e(\rho, T)$$

If the fluid can be assumed to be a calorically perfect gas the equation of state can be written as [9]

$$p = \rho RT \qquad e = C_v T \qquad (2.5)$$

in which R denotes the ideal gas constant, and C_v denotes the specific heat capacity at constant volume.

Equations (2.1)-(2.5) together contain six equations and six unknowns, three velocity components together with pressure, density and temperature. The equations are intricately coupled and must be solved simultaneously. However, by assuming incompressible flow, several simplifications can be made. The continuity equation can be reduced to Equation (2.6), which further implies that $(\star) = 0$ in Equation (2.3), reducing the Navier Stokes to equation (2.7).

$$\frac{\partial u_i}{\partial x_i} = 0 \qquad (2.6)$$

$$\frac{\partial u_i}{\partial t} + u_j \frac{\partial u_i}{\partial x_j} = -\frac{1}{\rho} \frac{\partial p}{\partial x_i} + \frac{\partial}{\partial x_j} \left[\nu \frac{\partial u_i}{\partial x_j} \right] + f_i \qquad (2.7)$$

When there are no density variations the energy equation is decoupled from the Navier-Stokes and continuity equation, resulting in four equations and four unknowns, three velocity components and pressure. The energy equation only needs to be solved in problems regarding heat transfer where the temperature is a desired quantity [9].

2.2 Dimensionless Numbers

In fluid mechanics there are many different dimensionless numbers, the relevant ones for this project is presented in this section.

2.2.1 Reynolds Number

The Reynolds number is the quotient between inertia and viscosity and is given as [10]

$$Re = \frac{\rho LU}{\mu} \qquad (2.8)$$

in which, L and U are characteristic length and velocity scales of the flow field. High Reynolds numbers are an indication of turbulent flow while low Reynolds numbers points at laminar flow [10].

2.2.2 Mach Number

The Mach number is defined as the flow velocity over the local speed of sound and is given as [11]

$$M = \frac{u}{a} \quad (2.9)$$

The Mach number can be used as an indication if the flow can be treated as incompressible or compressible. If $M \leq 0.3$ density changes due to pressure are negligible and the flow is thereby said to be incompressible [11].

2.3 Turbulence Modelling

The behaviour of fluids are either laminar or turbulent. In laminar flow, the flow behaves orderly and flows in adjacent layers while for turbulent flows, the flow acts random with a high degree of unsteadiness [9]. There is no exact definition for turbulence but, reference [12], states the main characteristics as

- **Irregular**
 - Turbulent flows are highly irregular, and may even seem random but they are governed by the Navier Stokes equation.
- **Diffusive**
 - The diffusivity increases in turbulent flows. Turbulence thereby increases the transfer of momentum while reducing the separation at bluff bodies.
- **High Reynolds numbers**
- **Three Dimensional**
 - Turbulence is partly created and sustained by the interactions between the velocity gradients and vorticity. These interactions are called *Vortex Stretching* and *Vortex Tilting* and are governed by

$$\omega_i = \varepsilon_{ijk} \frac{\partial v_k}{\partial x_j}$$

in which ω_i is the vorticity vector in tensor notation and ε_{ijk} is a permutation symbol and is per definition three dimensional.

- **Dissipative**
 - The turbulent energy is extracted by the large scale eddies from the mean flow, and transferred down to the small scale eddies (Kolmogorov scales) through the *cascade process* where finally the turbulent energy is transformed into heat, this transformation is known as dissipation.

2.3.1 Reynolds Averaged Navier Stokes

An approach to treat turbulence was given by Osbourne Reynolds [13], his approach is known as Reynolds Decomposition. In which he suggested that the flow field can be divided into a averaged part and a fluctuating part. In the case of incompressible flow, the velocity and pressure components can be divided as

$$u_i = \bar{u}_i + u'_i \quad p = \bar{p} + p' \quad (2.10)$$

in which, the bar denotes an average value and prime a fluctuating value. The average can be expressed in many different ways with time and Favré averages as examples [14]. By applying the Reynolds decomposition to the governing equations for incompressible flow the following equations are obtained

$$\begin{aligned} \frac{\partial \bar{u}_i}{\partial x_i} &= 0 \\ \frac{\partial \bar{u}_i}{\partial t} + \frac{\partial}{\partial x_j}(\bar{u}_i \bar{u}_j) &= -\frac{1}{\rho} \frac{\partial \bar{p}}{\partial x_i} + \frac{\partial}{\partial x_j} \left[\nu \frac{\partial \bar{u}_i}{\partial x_j} - \overline{u'_i u'_j} \right] \end{aligned} \quad (2.11)$$

where the extra term $-\overline{u'_i u'_j}$ exists on the right hand side of the momentum equation and is denoted as the Reynolds stress tensor (the external force vector has been omitted). The Reynolds stress tensor is responsible for the momentum transfer due to turbulent fluctuations [15]. In three dimensions, the Reynolds stress tensor consists of six independent components resulting in 10 unknowns, but only four equations. This predicament is known as the *Closure Problem* and is solved by modelling the Reynolds stresses [12].

2.3.2 Turbulence Models

Essentially, turbulence modelling comes down to model the Reynolds stresses and this can be done in a variety of different ways. One of the easier methods of doing this is through the *Boussinesq Assumption*, where a linear relation between the turbulent shear stresses and the averaged strain rate is assumed, as is the case in laminar flow [15]. With the Boussinesq assumption the Reynolds stresses can be written as

$$\overline{u'_i u'_j} = -\nu_t \overline{S_{ij}} + \frac{2}{3} k \delta_{ij} \quad (2.12)$$

where k is the turbulent kinetic energy and $\overline{S_{ij}}$ is the averaged strain rate

$$\begin{aligned} k &= \frac{1}{2} \overline{u'_i u'_i} \equiv \frac{1}{2} [\overline{u'_1 u'_1} + \overline{u'_2 u'_2} + \overline{u'_3 u'_3}] \\ \overline{S_{ij}} &= \frac{1}{2} \left(\frac{\partial \bar{u}_i}{\partial x_j} + \frac{\partial \bar{u}_j}{\partial x_i} \right) \end{aligned}$$

The term ν_t is denoted turbulent viscosity and characterises the turbulence [12], it is therefore not dependent on the fluid but on the flow. It has the same dimensions as viscosity and is expressed in terms of the turbulent velocity and the turbulent length scale [12]. Through this assumption, six unknown stresses are replaced with only parameter namely the turbulent viscosity, naturally this is a major simplification [12].

Models based on the Boussinesq assumption are usually categorised on the number of extra transport equations needed to obtain the turbulent viscosity, e.g. zero-equation models, one-equation models and two-equation models [16].

2.3.2.1 $k-\varepsilon$ Models

The $k - \varepsilon$ model proposed by [17, 18], is a two equation model and contains transport equations for both k and ε , where ε denotes the turbulent dissipation rate. These quantities are used to model the turbulent viscosity and turbulent scales [14]. Since the model

contains two variables the model is said to be complete and no prior knowledge of the turbulent structures are needed. The standard $k - \varepsilon$ model is given by [17, 18]

$$\begin{aligned} \rho \frac{\partial k}{\partial t} + u_j \rho \frac{\partial k}{\partial x_j} &= \frac{\partial}{\partial x_j} \left[\frac{\mu_t}{\sigma_k} \frac{\partial k}{\partial x_j} \right] + \mu_t \left(\frac{\partial \bar{u}_i}{\partial x_j} + \frac{\partial \bar{u}_j}{\partial x_i} \right) \frac{\partial \bar{u}_i}{\partial x_j} - \rho \varepsilon \\ \rho \frac{\partial \varepsilon}{\partial t} + u_j \rho \frac{\partial \varepsilon}{\partial x_j} &= \frac{\partial}{\partial x_j} \left[\frac{\mu_t}{\sigma_\varepsilon} \frac{\partial \varepsilon}{\partial x_j} \right] + c_{\varepsilon,1} \frac{\varepsilon}{k} \mu_t \left(\frac{\partial \bar{u}_i}{\partial x_j} + \frac{\partial \bar{u}_j}{\partial x_i} \right) \frac{\partial \bar{u}_i}{\partial x_j} - c_{\varepsilon,2} \rho \frac{\varepsilon^2}{k} \end{aligned} \quad (2.13)$$

The turbulent viscosity is obtained by dimensional analysis of the two quantities of the model as seen in Equation (2.14), for closure coefficients and more information see [17, 18].

$$\mu_t = C_\mu \rho \frac{k^2}{\varepsilon} \quad (2.14)$$

The $k - \varepsilon$ model performs poorly in flows with adverse pressure gradients [14], for which there exists a continuation on the standard model that imposes realizability constraints on the Reynolds stresses, hence the name realizable $k - \varepsilon$ model. The realizable $k - \varepsilon$ model was proposed by [19], where it was found that the performance of the realizable $k - \varepsilon$ model was higher in several simulation cases such as *rotating homogeneous shear flows*, *boundary-free shear flows* and *backward facing step flows*. The realizability constrains are [19]

$$\begin{aligned} \overline{u'_i u'_i} &\geq 0 \text{ no summation over } i \\ \frac{|\overline{u'_i u'_j}|}{\left[\overline{u'^2_i} \overline{u'^2_j} \right]^{1/2}} &\leq 1 \text{ no summation over } i \text{ and } j, i \neq j \end{aligned}$$

The constrains are ensured by modifying the turbulent viscosity through a varying C_μ and solving another transport equation for ε . For more details regarding the realizable $k - \varepsilon$ model see [19].

2.3.2.2 $k-\omega$ Models

The $k - \omega$ model proposed by [20] is also a two equation model and uses k and ω as variables for defining the turbulence, where $\omega = k/(\beta^* \varepsilon)$ and denotes the specific dissipation rate. The $k - \omega$ model for compressible flows with heat transfer omitted is given by [20]

$$\begin{aligned} \frac{\partial}{\partial t}(\rho k) + \frac{\partial}{\partial x_j}(\rho u_j k) &= \tau_{ij} \frac{\partial u_i}{\partial x_j} + \frac{\partial}{\partial x_j} \left[(\mu + \sigma^* \mu_t) \frac{\partial k}{\partial x_j} \right] - \beta^* \rho \omega k \\ \frac{\partial}{\partial t}(\rho \omega) + \frac{\partial}{\partial x_j}(\rho u_j \omega) &= \gamma \frac{\omega}{k} \tau_{ij} \frac{\partial u_i}{\partial x_j} + \frac{\partial}{\partial x_j} \left[(\mu + \sigma \mu_t) \frac{\partial \omega}{\partial x_j} \right] - \beta \rho \omega^2 \end{aligned} \quad (2.15)$$

The turbulent viscosity is given by equation (2.16), and for closure coefficients see [20].

$$\mu_t = k \rho / \omega \quad (2.16)$$

An advantage with the $k - \omega$ model is that it does not require any damping functions close to the wall for the low Reynolds number area as the $k - \varepsilon$ models does. But instead the

free stream boundary condition for ω causes issues as both $k \rightarrow 0$ and $\omega \rightarrow 0$ resulting in μ_t being undetermined or $\mu_t \rightarrow \infty$ [9].

To circumvent this problem Menter [21], proposed the $k - \omega$ Baseline (BSL) turbulence model that blends the $k - \varepsilon$ and $k - \omega$ model so that the $k - \omega$ model is used in the near wall region (viscous sublayer and logarithmic layer) and gradually blends into the $k - \varepsilon$ model in the fully turbulent region far from the wall. Menter further improved the $k - \omega$ BSL model to the $k - \omega$ Shear Stress Transport (SST) model by changing the definition for the eddy viscosity. The new definition of the viscosity gives the shear stresses obtained through his two equation model a higher resemblance with the shear stresses obtained through more advanced Reynolds Stress models [21]. The viscosity for the $k - \omega$ SST model is given by

$$\mu_t = \frac{a_1 k \rho}{\max[a_1 \omega; \Omega F_2]} \quad (2.17)$$

where

$$\begin{aligned} a_1 &= 0.31 \\ F_2 &= \tanh(\arg_2^2) \\ \arg_2 &= \max\left(2 \frac{\sqrt{k}}{0.09 \omega y}; \frac{500y}{y^2 \omega}\right) \end{aligned}$$

The $k - \omega$ BSL and SST model uses the same equation for k as the standard $k - \omega$ model but with different closure coefficients. But for the ω -equation a new source term appears on the right hand side due to cross diffusion and is seen below, the ω equation also contains new closure coefficients [21].

$$Source = 2\rho(1 - F_l)\sigma_{\omega 2} \frac{1}{\omega} \frac{\partial k}{\partial x_j} \frac{\partial \omega}{\partial x_j}$$

In the above equation $F_l \in [0, 1]$ and denotes the blending factor. In the near wall region $F_l = 1$ and as the wall distance increases $F_l \rightarrow 0$ [21].

2.4 Computational Fluid Dynamics

Computational Fluid Dynamics (CFD) is the combined discipline of physics, mathematics and computer science used to model and simulate fluid flows [15]. This section contains relevant aspects about CFD used in this project.

2.4.1 Wall Treatment

Turbulent boundary layers consists of four different regions and these regions can be explained through an analogy with the Reynolds number.

If one forms the Reynolds number and uses the wall distance as characteristic length for turbulent flows it can be found that for large distances from the wall the flow has high a Reynolds number and is thereby turbulent. But as the wall distance decreases, the Reynolds number decreases as well and eventually the viscous forces are of equal magnitude as the inertial forces. Even closer to the wall the viscous forces are of higher magnitude than the inertial forces indicating of a laminar flow. The boundary layer thereby consists

of a large region where the flow is dominated by inertia (*logarithmic region* and *outer region*), a region where the flow is governed as much by inertia as of viscosity (*buffer region*) and a thin layer where the flow is governed by viscosity (*viscous sublayer*) [9].

To determine where the transitions between the regions occur the dimensionless wall distance y^+ can be used, where y^+ is defined as [9]

$$y^+ = \frac{y}{\nu} \sqrt{\frac{\tau_w}{\rho}} = \frac{\Delta y_p}{\nu} \sqrt{\frac{\tau_w}{\rho}} \quad (2.18)$$

in which Δy_p is the distance between the solid boundary and the first cell centre in the wall normal direction. τ_w is the wall shear stress and is defined as

$$\tau_w = \mu \left. \frac{\partial u}{\partial y} \right|_{y=0} = \mu \frac{u_p}{\Delta y_p}$$

To completely resolve a turbulent boundary layer with all regions, a great spatial resolution is needed [9]. But instead of resolving the complete boundary layer a method known as wall functions can be used which empirically gives the velocity in the first cell depending on the y^+ value [9].

2.4.2 Courant–Friedrich–Lewy Number

The Courant–Friedriches–Lewy (CFL) number is a dimensionless number that relates the number of cells information travels during one time step while time marching in unsteady numerical simulations. The CFL number is given by [15]

$$C \geq \frac{u \Delta t}{\Delta x} \quad (2.19)$$

where C is the CFL number, i.e. the number of cells travelled in one time step. Δt and Δx are the time step and mesh size respectively, while u is the speed at which information travels through the computational domain. Low CFL numbers are good for stability and convergence while large CFL numbers gives faster time marching. Explicit time schemes require $C \leq 1$ to ensure convergence while implicit time schemes are unconditionally stable and can therefore have CFL numbers larger than one and still converge [15].

2.4.3 Moving Mesh Techniques

Fans are highly non stationary and the movement of the fans needs to be captured to adequately resolve the surrounding flow. Two ways of doing this are explained in the following subsections.

2.4.3.1 Moving Reference Frame

Moving Reference Frame (MRF) or frozen rotor approach is a procedure trying to incorporate rotational or translational effects into a steady simulation. In other words, a steady solution can be computed even though the flow is inherently unsteady. With the MRF solution procedure, the geometry is stationary and the fluid motion is augmented through

additional source terms in the momentum equation such as coriolis and centripetal acceleration. Since the MRF approach is stationary and the unsteady effects are added as source terms, the solution procedure assumes that the unsteady interaction between the moving and stationary frames are relatively weak. If there are strong unsteady interactions, these can only be captured by treating the flow as transient, in which a sliding mesh approach is more suited [22, 23].

2.4.3.2 Sliding Mesh

In the MRF approach, the motion is modelled through source terms in the momentum equation. For the sliding mesh technique, the motion of the geometry is not modelled but the geometry is actually moving with each time step, i.e. only applicable for transient simulations. With the sliding mesh technique, the entire computational domain is divided into a stationary and a non-stationary domain, with specific sliding interfaces between the domains. As the non-stationary domain moves in time, physical quantities are interpolated across the sliding interfaces to reflect the new position in the stationary domain. Since there is no modelling of the motion, the technique can handle problems with very strong transient effects, and doesn't suffer from the same modelling assumptions as the MRF approach [22, 23].

3

Theory of Acoustics

The following chapter presents a theoretical background regarding acoustics with further continuation into general acoustics, aeroacoustics, and some signal processing relevant for this study.

3.1 General Acoustics

Sound can be defined as pressure fluctuations propagating through any medium, for ventilation fans the medium is air [1]. The propagation can be derived from the continuity equation (2.1) and the Navier Stokes equation (2.2) under the assumptions that the fluid is quiescent with no external loads, and by neglecting molecular diffusion and relaxation. With the mentioned assumptions the sound propagation can be written as a homogeneous wave equation as [24, 25]

$$\begin{aligned}\frac{1}{a^2} \frac{\partial^2 p}{\partial t^2} - \frac{\partial^2 p}{\partial x_i \partial x_i} &= \square^2 p = 0 \\ \frac{\partial^2 \rho}{\partial t^2} - a_0^2 \frac{\partial^2 \rho}{\partial x_i \partial x_i} &= \square^2 \rho = 0\end{aligned}\tag{3.1}$$

depending on the acoustic variable and where \square^2 denotes d'Alembertian operator. The absence of molecular diffusion implies that the entropy remains constant for a fluid element [24]. With entropy constant, the change in density is related to the change in pressure through the propagation speed or the speed of sound a . For an ideal gas this relation can be written as [26]

$$a = \sqrt{\frac{\partial p}{\partial \rho}} = \sqrt{\gamma RT}\tag{3.2}$$

or

$$p = a^2 \rho\tag{3.3}$$

The wave length of specific tones are obtained by dividing the propagation speed with the frequency of the tone as [27]

$$\lambda = \frac{a}{f}\tag{3.4}$$

and if the wave length is much smaller then the sound source i.e.

$$\frac{L_s}{\lambda} \ll 1\tag{3.5}$$

the sound source is said to be acoustically compact [4].

3.1.1 Sound Levels

The human ear perceives pressure fluctuations within a large range from 20 [μPa] as the lower and 200 [Pa] as the upper limit for frequencies in the range of a few hertz up to 20 [kHz] [25]. At 1000 [Hz] there is a heightened perception and it is at this frequency that the lowest audible pressure fluctuation of 20 [μPa] is perceived and is known as the reference pressure in air p_{ref} [28]. Both the *Sound Pressure level* (SPL) and the *Sound Power Level* (SWL) are used to quantify the emitted sound, and are defined as [1]

$$L_p(dB) = 20 \cdot \log_{10} \left(\frac{p_{rms}}{p_{ref}} \right) \quad (3.6)$$

$$L_W(dB) = 10 \cdot \log_{10} \left(\frac{W}{W_{ref}} \right) \quad (3.7)$$

where W is the sound power of the noise source, and the reference acoustic power $W_{ref} = 10^{-12}$ [W].

3.1.2 Sound Sources

The right hand side of equation (3.1) can be non zero resulting in an inhomogeneous wave equation with the terms on the right hand being called sound sources. In aeroacoustics, three basic sound sources exists namely monopole, dipole and quadrupole sources and these are briefly explained in the following section.

3.1.2.1 Monopole

Monopole or simple source is the most fundamental sound source. It can be described as a pulsating sphere where the volume is changing with respect to time resulting in a mass flow rate or mass injection [28]. A pulsating sphere is symmetric and thus, the radiation can be said to be equally good in all directions [24]. If the mass injection is represented by $\frac{\partial Q}{\partial t}$, the wave equation can be written as [27]

$$\square^2 p = \frac{\partial Q}{\partial t}$$

For monopole sound sources the propagated sound power scales as

$$W_m \propto \frac{\rho_0 d^2 U^4}{a} \quad (3.8)$$

where for fans, U is the tangential velocity and d is the circumference divided by the number of blades [29].

3.1.2.2 Dipole

Dipoles can be described as two monopoles superimposed in antiphase, i.e. when the first monopole is expanding the second monopole is contracting [28]. For two monopoles in antiphase to be called a dipole the distance between them must be small compared to the wave length of the produced sound, i.e. compact [28]. Due to the antiphase, the radiation

has its absolute value at the axis of the two monopoles, which reduces to zero at an angle perpendicular to the axis [24]. The antiphase is also responsible for producing a net force on the fluid instead of net volume flow [24], and the wave equation can therefore be written as

$$\square^2 p = -\frac{\partial F_i}{\partial x_i}$$

The propagated sound power for dipoles scales with [29]

$$W_d \propto \frac{\rho_0 d^2 U^6}{a^3} \quad (3.9)$$

By comparing equation (3.9) and (3.8) it can be seen that the scaling difference in generated sound power between monopole and dipole sound sources can be written as [29]

$$\frac{W_d}{W_m} \propto M^2$$

resulting in inefficient generation for low mach numbers and efficient radiation for high mach numbers.

3.1.2.3 Quadrupole

Quadrupoles can be described as two dipoles of equal strength but at opposite locations and can be either in a longitudinal or lateral state depending if the two dipoles have a common axis or are located side by side [25]. Quadrupoles are the main sound source in air flows in which there are no solid boundaries, and occurs mainly due to the transfer of momentum in air flows [28]. According to Lighthill [30], the wave equation for quadrupoles could be written as

$$\square^2 p = -\frac{\partial^2 T_{ij}}{\partial x_i \partial x_j}$$

and will be showed more thoroughly in Section 3.2.2.1. The sound power for quadrupoles scales with [29]

$$W_q \propto \frac{\rho_0 d^2 U^8}{a^5} \quad (3.10)$$

comparison between equation (3.9) and (3.10) gives

$$\frac{W_q}{W_d} \propto M^2$$

indicating that quadrupoles are very inefficient radiators for low mach numbers but very efficient at high [29].

3.1.3 Aerodynamic Sound

The generated sound produced by ventilation fans can be divided into

- Aerodynamic
- Electromagnetic
- Mechanical

where the aerodynamic sound is the largest contributor of the overall sound [1]. The aerodynamic sound can be categorised as either tonal or broadband. Tonal sounds (clear tones) have distinct dominant frequencies while broadband sounds contain multiple frequencies of the same magnitude spread through out the entire frequency spectra (random) [1]. Distinct frequencies or tones are produced by the fan blades displacing air (monopole source) and the fan blades interacting with the flow (dipole source). The broadband sound is produced by turbulence interfering with the solid boundaries [2], and consists of both dipole (vortex shedding and boundary layers) and quadrupole sources (air turbulence) [1]. The distinct tones produced by the monopole and dipole sources are radiated at the blade passage frequency and the higher harmonics [1].

3.2 Computational Aeroacoustics

Computational Aeroacoustics (CAA), is the combined field of computational aerodynamics and acoustics and deals with flow induced sound, in which the sound sources are predicted and the sound propagated numerically [31]. In CAA there are conceptually two different approaches on how to deal with the propagation of sound characteristics to the far field, the *Direct Method* and the *Hybrid Method* [3].

3.2.1 Direct Method

The Direct method can be considered the most exact aeroacoustical simulation, the fully compressible unsteady Navier Stokes equation is solved in a computational domain that stretches from the sound source to the far field observer. The spatial and temporal resolution must be high to fully resolve all aerodynamic and acoustic variables, combined with a long distance from the sound source to the far field observers generates a large amount of cells and time steps resulting in a very computational heavy simulation [3, 31]. Acoustic waves are non dissipative and non diffusive, but many current numerical schemes in computational fluid dynamics are highly dissipative and diffusive resulting in acoustic waves being distorted and damped before reaching the far-field [3, 31]. There are no numerical schemes that produce accurate results for both CFD and acoustics and trade offs are often necessary [3, 31].

3.2.2 Hybrid Method

With the hybrid method, the far-field acoustics are decoupled from the aerodynamic near-field sound resulting in two separate computations. By decoupling the near-field and far-field sound, the stringent demands can be relaxed since the two computations can be tailored for each individual task. The first step is to calculate the pressure and velocity fluctuations in the near field, and secondly, use the computed fluctuations as input variables in a separate computation where the sound is transported to the far-field [3, 31]. The far field transportation can be done in different ways with *computational transport* and *analytical transport* being two examples. In the computational transport method, partial differential equations are solved as in CFD, but since the transportation is focused only on the acoustics, it generally suffices to solve more simple differential equations such as the linearised Euler equations or ordinary wave equations. The analytical transport method is based on an integral formulation where the sources are integrated along a surface or

a volume surrounding the aerodynamic area [3, 31]. There are many different analytical transport methods, e.g. the Lighthill's acoustic analogy which was further extended by Ffowcs William & Hawkings. These will be presented in more detail in section 3.2.2.1 and 3.2.2.2

3.2.2.1 Lighthill's Acoustic Analogy

Lighthill's acoustic analogy gives the acoustic radiation of sound induced by a flow field with the assumptions that the surrounding fluid is isotropic, at rest and that there are no solid boundaries present. In 1952, Sir James Lighthill published an article [30], in which he derived a inhomogeneous wave equation from the continuity equation (2.1) and momentum equation (2.2). It was derived by multiplying the continuity equation with u_i , adding it to the momentum equation, subtracting and adding the term $a_0^2 \frac{\partial \rho}{\partial x_i}$, which gives the first part as ¹

$$\frac{\partial(\rho u_i)}{\partial t} + a_0^2 \frac{\partial \rho}{\partial x_i} = \frac{\partial T_{ij}}{\partial x_i} \quad (3.11)$$

By differentiation of the continuity equation with respect to time, taking the divergence of the above equation and subtracting the results finally yields the Lighthill's equation as

$$\frac{\partial^2 \rho}{\partial t^2} - a_0^2 \frac{\partial^2 \rho}{\partial x_i \partial x_i} = \square^2 \rho = \frac{\partial^2 T_{ij}}{\partial x_i \partial x_j} \quad (3.12)$$

in which T_{ij} is the Lighthill's turbulence stress tensor that gives the acoustic field generated by a quadrupole source and is given by

$$T_{ij} = \rho u_i u_j - a_0^2 \rho \delta_{ij} + p \delta_{ij} - e_{ij} \quad (3.13)$$

To be able to obtain the propagated sound at least some knowledge about T_{ij} is needed and a few simplifications can be made [26]. Lighthill argues that for a turbulent flow field the inertia effects are typically much larger than the viscous effects, i.e. $\rho u_i u_j \gg e_{ij}$, and by assuming that the density and pressure fluctuations are small within the flow field, T_{ij} then reduces to $T_{ij} \approx \rho u_i u_j$ inside the flow field. Outside of the flow field, where one of the main assumptions was that the surrounding fluid was at rest, thus, far away from the flow field the velocity ought to be small meaning the $\rho u_i u_j \rightarrow 0$. Furthermore, the viscous stresses are also known to be small and it can therefore be concluded that T_{ij} equals to zero outside of the flow field [30]. The approximations of Lighthill's turbulent stress tensor can be summarised as seen below.

$$T_{ij} = \begin{cases} \rho u_i u_j & \text{If inside the flow field} \\ 0 & \text{Else} \end{cases}$$

By solving the Lighthill's equation one can predict the sound radiation from a flow region embedded in a quiescent fluid with no solid boundaries, or when the solid boundaries can be neglected. The solution can then be expressed through the free space Green's function as [26]

$$\rho(\mathbf{x}, t) - \rho_0 = \frac{1}{4\pi a_0^2} \frac{\partial^2}{\partial x_i \partial x_j} \int \frac{T_{ij}(\mathbf{y}, \tau)}{R} d\mathbf{y} \quad (3.14)$$

¹subscript 0 indicates constant reference values

where $R = |\mathbf{x} - \mathbf{y}|$ and denotes the distance between the sound source and the far-field observer. The integral is evaluated at the far-field location and must therefore be evaluated at a retarded time $\tau = t - R/a_0$, which is the elapsed time for the sound to propagate to the far-field observer.

3.2.2.2 Ffowcs Williams & Hawking's Acoustic Analogy

Lighthill's equation is only valid when the solid boundaries can be neglected, but in many engineering applications solid boundaries are present and directly influence the sound generation [26]. Fans is one such application when the effect of solid boundaries can not be neglected and a different sound emission theory is thus needed. Curle [32] extended the Lighthill's acoustic analogy to include stationary surface effects while Ffowcs Williams & Hawkings (FW-H) [33] included effects of surfaces with arbitrary motion. For complete derivation of the FW-H equation see [33]; the propagated sound according to FW-H can be written as

$$\left[\frac{\partial^2}{\partial t^2} - a_0^2 \frac{\partial^2}{\partial x_i \partial x_i} \right] (\rho - \rho_0) = \frac{\partial^2 T_{ij} H(f)}{\partial x_i \partial x_j} - \frac{\partial}{\partial x_i} \left[\sigma_{ij} \delta(f) \frac{\partial f}{\partial x_j} \right] + \frac{\partial}{\partial t} \left[\rho_0 v_i \delta(f) \frac{\partial f}{\partial x_i} \right] \quad (3.15)$$

where the first term on the right hand side is the quadrupole sound source from Lighthill's analogy, the second and third term are the dipole and monopole sources related to the solid boundaries. In equation (3.15), f denotes the sound source surface, and the spatial derivative equals the normal, i.e. $\frac{\partial f}{\partial x_j} = n_j$. By again using Green's free space function an analytical solution can be obtained as

$$\begin{aligned} \rho(\mathbf{x}, t) - \rho_0 = & \frac{1}{4\pi a_0^2} \left(\frac{\partial^2}{\partial x_i \partial x_j} \int \left[\frac{T_{ij}}{R|1 - M_r|} \right] d\boldsymbol{\eta} \right. \\ & - \frac{\partial}{\partial x_i} \int \left[\frac{\sigma_{ij} n_j}{R|1 - M_r|} \right] dS(\boldsymbol{\eta}) \\ & - \frac{\partial}{\partial x_i} \int_{V_0} \left[\frac{\rho_0 \dot{u}_i}{R|1 - M_r|} \right] d\boldsymbol{\eta} \\ & \left. + \frac{\partial^2}{\partial x_i \partial x_j} \int_{V_0} \left[\frac{\rho_0 u_i u_j}{R|1 - M_r|} \right] d\boldsymbol{\eta} \right) \end{aligned} \quad (3.16)$$

in which $\boldsymbol{\eta}$ is a Lagrangian coordinate system following the surface. M_i is the Mach number of the moving surface and M_r is the component of M_i in the direction of r_i . The terms included within [...] are evaluated at the far-field observer, i.e. at a retarded time [33]. The first term in equation (3.16) corresponds to the solution from Lighthill's equation, while the three remaining terms are associated with the solid boundaries. The first of these terms are the sound produced by the fluctuating force from the solid boundaries on the fluid, and the two remaining represents the generated sound from volume displacement [26].

3.3 Signal Treatment

In acoustics pressure fluctuations are usually sampled in time and thereby form a discrete signal. This section contains relevant information regarding signal treatment such as Fourier transform and sampling rates.

3.3.1 Fourier Transform

The Fourier Transform is an operator that transforms a signal from the time domain to the frequency domain through [34]

$$F(\omega) = \int_{-\infty}^{\infty} f(t)e^{-i\omega t} dt \quad (3.17)$$

The transformation can only take place if the function $f(t)$ is continuous or piece-wise continuous. In many engineering applications the function is not always continuous where an approximation of the ordinary Fourier transform named *Discrete Fourier Transform* (DFT) or *Fast Fourier Transform* (FFT) can be used instead [34].

3.3.2 Sampling Rate

To be able to reproduce a signal through sampling, the minimum sampling frequency must be at least twice the highest frequency of the function [35], see Equation 3.18. The minimum sampling frequency is known as the *Nyquist rate*.

$$f_s = 2 \cdot f_{max} \quad (3.18)$$

4

Methodology

Computational resources were limited in this study, and a hybrid approach instead of a direct approach was therefore more suited. The hybrid approach used in this study involves sampling the pressure fluctuations during a transient simulation and propagate these to the far-field observers using Ffowcs-William and Hawkings acoustic analogy. To capture the transient behaviour of the centrifugal fan a sliding mesh technique has been adopted, in which the centrifugal fan actually rotates with each time step.

4.1 Softwares

The main softwares used in this project are ANSA 16.1 for geometry cleaning and mesh generation, FLUENT 16.1 for CFD simulations and post-processing, CFD-POST 16.1 and MATLAB 2014b for further post-processing.

- ANSA is a pre-processing tool developed by BETA CAE SYSTEMS S.A. and is commonly used in the computer aided engineering industry. ANSA provides methods for cleaning CAD-geometries i.e. repairing holes and intersections, but also gives the possibility to create surface and volume meshes required for CFD-simulations.
- FLUENT is a CFD-software developed by ANSYS with the possibility to model a broad variety of flows. FLUENT is extensively used throughout the literature for simulations regarding pressure fluctuations for acoustics, [36, 37, 38], and is an appropriate choice for this study as well.
- CFD-POST is a post-processing software developed by ANSYS with the ability to easily visualise physical quantities of interest through contour plots, streamlines or tables for example.
- MATLAB is a mathematical engineering tool developed by MATHWORKS, and gives the possibility to perform various mathematical operations such as Fourier transforms, matrix manipulations and visualisation of data.

4.2 Creation of the Computational Domain

This section presents a comprehensive view on how the computational domain and the mesh was created. This includes modifications made to the domain, grid topology, number of cells and grid density in different regions.

4.2.1 Computational Domain

Swegon supplied a complete CAD-geometry of the centrifugal fan with all its surrounding parts corresponding to the actual model used in their experimental testing for aerodynamics and acoustics. The obtained model can be seen in Figure 4.1a, in which the flow enters from the top and leaves through the bottom.

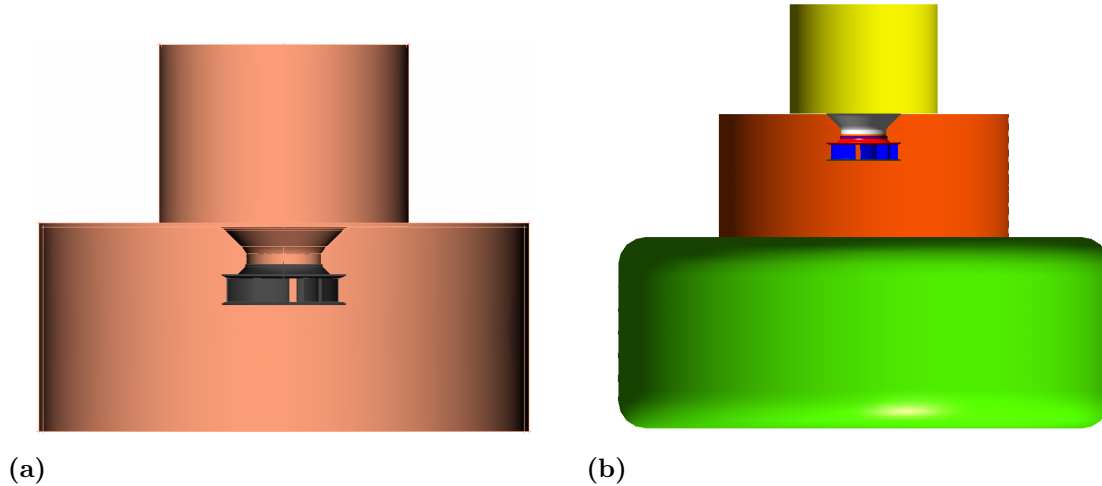


Figure 4.1: In (a), geometry of the centrifugal fan within its test casing supplied by Swegon. In (b), the extended domain to mitigate boundary effects on the flow.

As seen in Figure 4.1a, the distance between the centrifugal fan and the outlet is short. To mitigate boundary effects on the solution, the computational domain was extended as seen in Figure 4.1b. The extended part is treated as an outlet to not impose wall boundary conditions where there aren't any walls. The different colours in Figure 4.1b, represent different *Part Identities* (PIDs) in ANSA. By dividing the complete model into separate PIDs, it was possible to customise the mesh generation and to set individual boundary conditions. The PIDs used for the different parts of the centrifugal fan are visualised in Figure 4.2a. Table 4.1 gives the colour scheme for the individual PIDs.

Table 4.1: PIDs used to categorise the computational domain in Figure 4.1b and Figure 4.2.

PID	Colour
Impeller Inlet	White
Impeller Inlet Bottom	Light Orange
Blades	Blue
Shroud	Red
Shroud Top	Purple
Back plate	Dark Green
Interfaces	Cyan
Inlet Side	Yellow
Outlet Side	Dark Orange
Outlet	Light Green

To be able to run MRF and Sliding mesh simulations the domain had to be divided into a rotating and stationary domain. For the sliding mesh technique, two coinciding sliding

interfaces had to be created as well. One interface belonging to the rotating domain and one interface belonging to the stationary domain, more about the sliding interfaces can be found in Section 2.4.3. The centrifugal fan together with the rotating interfaces are shown in Figure 4.2b.

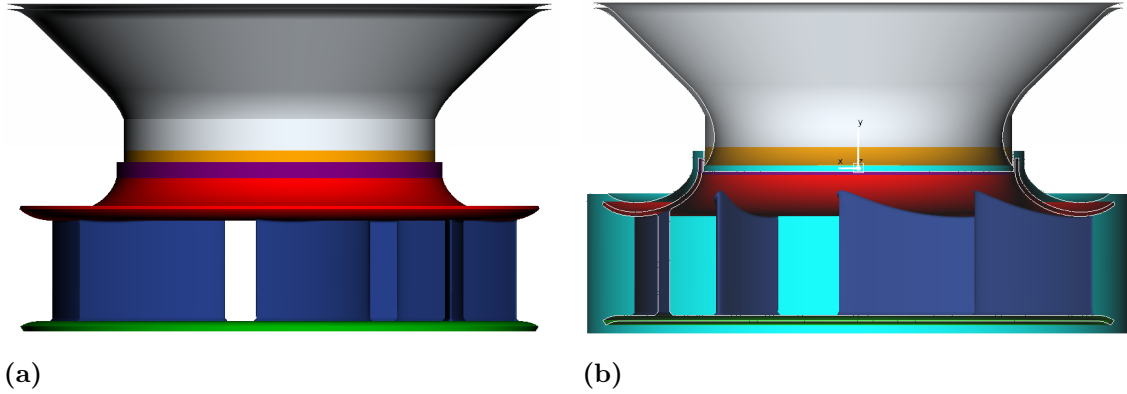


Figure 4.2: In (a), a closeup of the centrifugal fan. In (b), the centrifugal fan together with the sliding interfaces in a cut through the middle.

4.2.2 Mesh Generation

An unstructured hybrid grid topology was used to capture the complex features of the two domains. The surface mesh was generated with triangular elements, while the volume mesh contains penta elements for the boundary layers, together with pyramid and tetra elements for the remaining volume. The rotating region, containing the centrifugal fan, has a relatively high grid density which gradually decreases into a less dense grid for the stationary domain. Each fan blade has between 120 – 160 grid nodes along the profile and 38 – 48 grid nodes in the spanwise direction. The volume mesh was created in two steps, first the boundary elements were extruded from the wall surfaces, and from which, the remaining volume was grown. The first boundary layer cell on the centrifugal fan surfaces was placed at a height of 30 % of the length of the surface mesh and grew with a factor of 1.3. For the stationary boundary layers, the first height was 20 % of the surface mesh and grew with a factor of 1.3. The remaining volume for both the stationary and rotating domain were grown from the boundary elements with a factor of 1.3. The growth of the volume mesh was limited in an area surrounding the centrifugal fan. The refinement stretches from half a fan height below the fan to half a fan height above fan and all the way to the outlet side. Within this region, the element size was limited to 15 [mm]. According to reference [39], at least 10 elements are needed to accurately resolve an acoustic wave. The aim of this study was to capture the fundamental frequencies below 1700 [Hz], at which the wave length can be calculated through Equation (3.4) to 0.20 [m]. Thus, in the refined region surrounding the centrifugal fan, there are approximately 13.3 elements per highest desired acoustic wave length. Figure 4.3a, shows the computational grid in the entire domain, where the refined region surrounding the centrifugal fan is clearly seen.

Between the shroud of the fan and the impeller inlet is a small gap to ensure that rotations are possible in the real fan model. For the modelling to be as realistic as possible this gap was kept open and the sliding interfaces were placed within the gap. A coarse grid resolution with two grid nodes and a fine resolution with six grid nodes were used, see Figure 4.3.

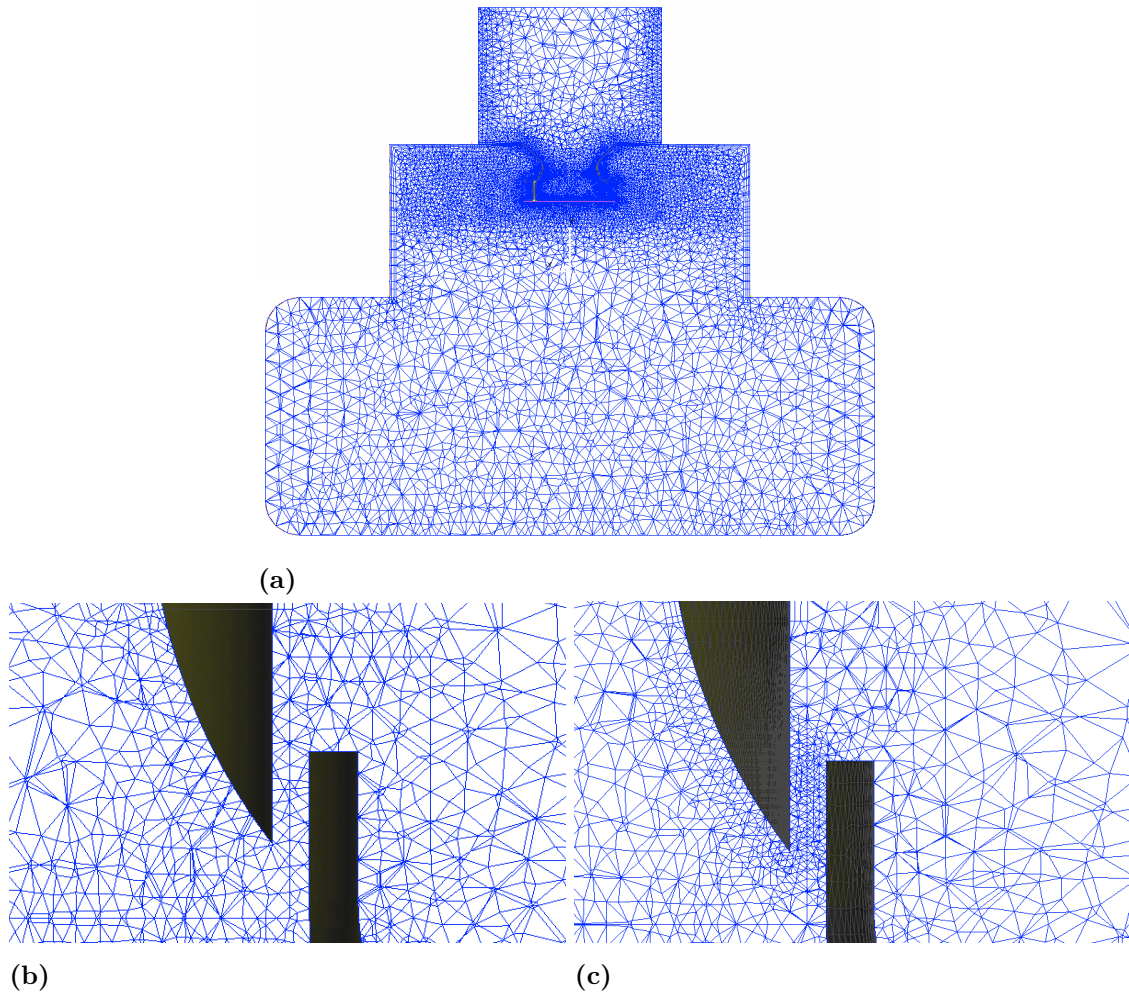


Figure 4.3: Resolution of the gap between Shroud Top and Impeller bottom for coarse grid (a) and fine grid (b).

The centrifugal fan geometry together with its surroundings are rotationally symmetric and can be divided into seven sectors. Studies such as [40, 41, 42], suggests that sector models can be used to predict the main features of the sound spectrum. By modelling only a sector, the flow and turbulent structures are assumed perfectly symmetric which is never completely satisfied. The periodic boundaries influence the creation of turbulent structures which could result in an over prediction of the sound pressure levels [40]. By using an azimuthal sector of $360/7 = 51.42857^\circ$, the computational time can be drastically reduced while grid distribution remains the same. The grid density of the sector is between the two grid densities of the complete models mentioned above, with four grid cells in the gap between shroud and impeller inlet. The sector model contains four periodic boundaries, two rotating and two stationary and the same sliding interfaces as for the full domain model. The periodic boundaries were made conformal as required by FLUENT. For specific number of cells within the three computational grids, see Table 4.2.

The quality of the computational grid was determined in terms of skewness and angles of the grid cells. The angle is calculated with equation 4.1, and should be below 0.7 for tetras, pentas and pyramid elements recommended by ANSA. The skewness is kept below 0.92 for all cells in the domain, and was below the value of 0.98 recommended by FLUENT.

$$Angle = \max \left[\frac{\max(\phi) - F}{180 - F}, \frac{F - \min(\phi)}{F} \right] \quad (4.1)$$

$F = 60$ for tria faces.
 $F = 90$ for quad faces.

Table 4.2: The number of cells in the different regions of the computational domain for the two computational domains.

Region	Type	No. Of Cells		
		Coarse	Fine	Sector
Stationary Boundary Layers	Pentas	135816	135816	20407
Stationary Remaining	Pyramids & Tetras	2291285	3166100	338664
Stationary Total		2427101	3301916	359071
Rotating Boundary Layers	Pentas	594222	511368	88161
Rotating Remaining	Pyramids & Tetras	2173790	2539631	383559
Rotating Total		2768012	3050999	471720
Total Domain		5195113	6352915	830791

4.3 Numerical Simulation

This section presents how the aerodynamics are coupled and solved together with the acoustic prediction. Firstly, the CFD-procedure is briefly described, followed by one section involving the the aerodynamics and one section regarding the acoustic prediction.

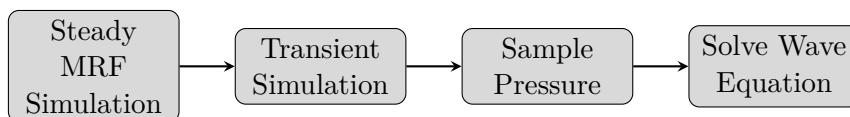


Figure 4.4: The complete computational procedure to obtaining the sound characteristics in the far-field

The complete computational procedure can be visualised in Figure 4.4 and starts with running steady MRF simulations of the centrifugal fan. By analysing the steady flow, an initial understanding of the flow can be obtained and variables such as pressure increase, torque and volume flow of the fan can be evaluated for credibility of the simulation. The steady MRF simulation also gives an excellent initialisation from which to start the transient simulations. By doing so, the time for reaching a developed state can be much reduced. During the transient simulation, a sliding mesh technique has been adopted where the impeller slides relative to the casing. In a study by [43], the sliding mesh technique was adopted for a centrifugal pump, in which good resemblance with experimental

results were found and has served as a guideline for similar studies since then. When the above mentioned variables start exhibiting a periodic behaviour, the flow is regarded as fully developed and the pressure sampling can begin. When an appropriate number of samples have been obtained the acoustic wave equation can be solved to obtain the sound characteristics in the far-field.

4.3.1 Aerodynamics

In this study, FLUENT 16.1 has been used to solve the compressible and incompressible flow equations through the finite volume method. For both cases, the fluid is treated as air with standard properties from FLUENT. When the flow was considered compressible, air was treated as an ideal gas. Incompressible flow can usually be assumed when the flow is low subsonic ($M \leq 0.3$), see Section 2.2.2. The highest mach number in the computational domain equals approximately 0.14 and is clearly subsonic. There are also multiple studies, [36, 44, 45], suggesting that the acoustic sound sources can be predicted with an incompressible flow assumption. But, if the sound source regions are not acoustically compact, the presence of the solid boundaries are felt by the hydrodynamic field as well as the acoustic field [4]. When the sources are not acoustically compact, the Green's function must be tailored to the individual geometry at hand to accurately account for surface reflections [4]. The FW-H equation makes use of the Green's free space which implies that for non compact sound sources, the flow must be obtained from a compressible flow simulation [4]. The influence of compressible/incompressible flow was investigated to find the main differences.

4.3.1.1 Pressure Velocity Coupling

A pressure based solver has been used in this study, this implies that mass conservation of the velocity field is achieved by correcting the pressure and repeating this procedure. The governing equations can either be solved sequentially or coupled, i.e. one at a time, or all together. By solving the equations sequentially, the memory usage is lower since only one equation needs to be stored in the memory at a time, but the procedure must be repeated several time yielding a low convergence rate. By instead using a coupled solver, all governing equations are solved simultaneously which requires more memory but yields higher convergence rate. The model is of relatively small size, and memory will not be the limiting factor, which is why the coupled solver was used for the benefits with a higher rate of convergence. Table A.1 and Table A.2 gives the general solution control settings used for the numerical simulations in FLUENT.

4.3.1.2 Time Step

The chosen time step is related to the angular velocity of the centrifugal fan so that 1° is rotated per time step. Similar studies related to prediction of tonal noise of centrifugal fans such as [46, 36, 45] uses 300, 400 and 363 time steps per revolution. With a rotational velocity of 3500 [rpm], a time step of $\Delta t = 4.7619 \cdot 10^{-5}$ [s] is obtained. According to the Nyquist criterion, see Section 3.3.2, such a time step will be able to resolve frequencies up to 10500 [Hz] and was far above the highest desired frequency of 1700 [Hz].

However, in reference [3], a more conservative criterion is suggested. The time step should be taken as the tenth of the inverse of the highest desired frequency as

$$\Delta t = \frac{1}{10f_{max}} \quad (4.2)$$

With the chosen time step, the highest resolved frequency according to Equation (4.2) equals $f_{max} = 2100 [Hz]$.

4.3.1.3 Discretization

In computational aeroacoustics the magnitude difference of scales between aerodynamics and aeroacoustics poses a great challenge, where the energy ratio can be in the order of [3].

$$\frac{P_{Sound}}{P_{Mech}} = 10^{-4} M^5 \quad (4.3)$$

When performing aerodynamic simulations, errors are introduced which are in the same magnitude as the acoustics. To obtain relevant sound characteristics, the diffusion and dispersion errors must be kept as low as possible, otherwise the numerical errors will introduce a numerical noise of the same magnitude [3].

Density, momentum, energy and turbulent quantities were discretized with a 2^{nd} order upwind scheme. The second order schemes were considered accurate enough while still retaining a high level of stability. Pressure on the other hand was discretized with a 2^{nd} order central difference scheme and the PRESTO (PREssure STaggering Option) scheme. The latter scheme is more accurate for interpolating face pressure values together with acoustic analogies [47]. The aforementioned pressure schemes were both included in the parameter study.

The temporal discretization scheme used was a 2^{nd} order implicit time scheme. An implicit scheme was selected due to small cell sizes in the rotating domain. For implicit schemes, the spatial grid size does not directly determine the temporal step through the CFL number as it does for explicit schemes, see Section 2.4.2. Thus, a larger time step could be used while still retaining stability. The acoustic CFL numbers for the full domain coarse, full domain fine and sector grid can be seen in Figure 4.5.

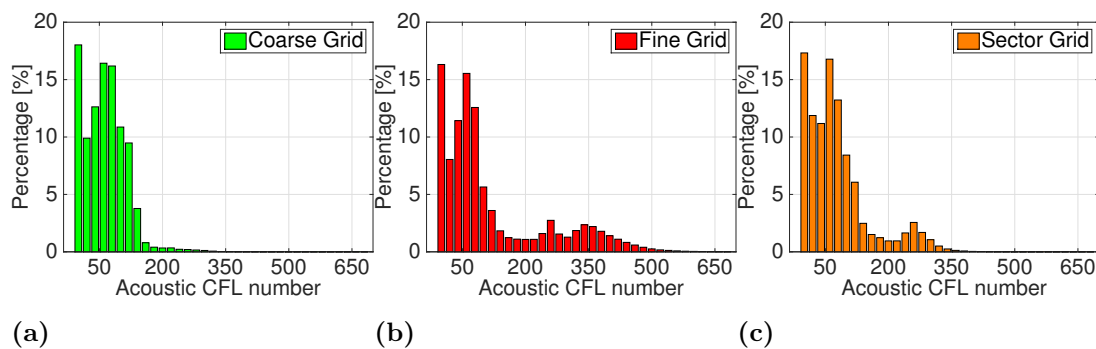


Figure 4.5: Acoustic CFL numbers divided into 50 sections for the full domain coarse (a), full domain fine (b) and sector grid (c).

4.3.1.4 Turbulence models

The flow through the centrifugal fan is highly turbulent and the turbulence needs to be resolved in an appropriate manner to be able to obtain accurate flow variables. The most accepted methods are LES or URANS, where URANS can be performed at a much lower computational effort. However, URANS only provides the possibility to capture the large scale motions and therefore only information about tonal sounds can be provided [4]. Within URANS, there is no consensus about what turbulence model that should be used for centrifugal fan acoustic simulations. Different versions of the $k - \varepsilon$ turbulence model are a common choice [37, 45], and so is the $k - \omega$ SST turbulence model [36, 7]. Seeing that both types of turbulence models are commonly used, the two types were used in this study as well. According to reference [48], the $k - \omega$ SST model displays a high performance in complex flows regarding separation and adverse pressure gradients which could be expected around the blades of the fan. While the realizable $k - \varepsilon$ as mentioned in Section 2.3.2.1, shows a higher performance compared to the normal $k - \varepsilon$ model in a variety of different flows. See Table A.3 for specific values for the closure coefficients used for the two turbulence models in FLUENT.

4.3.1.5 Boundary Conditions

In the experimental testing, the centrifugal fan was connected to a motor with a fixed rotational velocity. The pressure difference over the centrifugal fan was specified and for the given pressure difference, the volume flow was measured. The boundary conditions used for the numerical simulation are set to resemble that situation. At the inlet, the mass-flow and volume flow were specified to the measured value for the compressible and incompressible simulations respectively. At the outlet the pressure was specified to atmospheric pressure. The walls are treated as no-slip surfaces where the velocity equals zero in a local reference frame. For specific values regarding the boundary conditions see Table 4.3 for compressible flow and Table 4.4 for incompressible flow.

4.3.1.6 Turbulence Boundary Conditions

The turbulence at the inlet was defined with the assumption of fully developed flow, in which the turbulence can be characterised by intensity and length scale through equation (4.4) [23]

$$\begin{aligned} I &= 0.16 \cdot (Re_D)^{-1/8} \\ \ell &= 0.07 \cdot D \end{aligned} \tag{4.4}$$

in which Re_D is the Reynolds number based on the inlet side diameter. The back flow turbulence at the outlet was defined through the same equations as for the inlet, but here D equals the outlet side. For specific values regarding the boundary conditions see Table 4.3 and Table 4.4.

4.3.1.7 Wall Treatment

Depending on where the first cell is located different modelling approaches are needed, as explained in Section 2.4.1. By using FLUENT's *Enhanced Wall Treatment* function, FLU-

Table 4.3: Boundary conditions used for the compressible simulation.

Boundary	Boundary Condition	Boundary Values
Inlet	Mass-flow Inlet	\dot{m} = 0.4907 [m^3/s]
		T_{in} = 288.16 [$^{\circ}C$]
Outlet	Pressure Outlet	P_{out} = 101325 [Pa]
		T_{out} = 288.16 [$^{\circ}C$]
Walls	No-slip Surface	$u_{w,local}$ = 0 [m/s]
Inlet Turbulence	Intensity & Length Scale	I_{in} = 4.094 [%]
		ℓ_{in} = 0.0371 [m]
Back Flow Turbulence	Intensity & Length Scale	I_{out} = 4.34 [%]
		ℓ_{out} = 0.0728 [m]

Table 4.4: Boundary conditions used for the incompressible simulation.

Boundary	Boundary Condition	Boundary Values
Inlet	Velocity Inlet	v_{in} = 1.85 [m/s]
Outlet	Pressure Outlet	P_{out} = 101325 [Pa]
Walls	No-slip Surface	$u_{w,local}$ = 0 [m/s]
Inlet Turbulence	Intensity & Length Scale	I_{in} = 4.094 [%]
		ℓ_{in} = 0.0371 [m]
Back Flow Turbulence	Intensity & Length Scale	I_{out} = 4.34 [%]
		ℓ_{out} = 0.0728 [m]

ENT has the possibility to check the first cell height, and depending on the y^+ value apply either a low Reynolds model or a wall function. Thus, the first cell can be located either in the viscous sublayer, buffer region or log-law region without accuracy deterioration. For more information regarding the enhanced wall treatment see reference [22]. This model has to be chosen for the realizable $k - \varepsilon$ model but is default for the $k - \omega$ SST model.

4.3.1.8 Convergence

The general convergence criteria used in this study was 10^{-4} for turbulent quantities, continuity and momentum and 10^{-7} for energy. Physical quantities such as static pressure at the inlet, volume flow at the outlet and torque of the centrifugal fan are also considered when determining convergence of the solution. The steady simulations can not capture the entire transient behaviour of the rotating fan, in which all the residuals do not decrease below 10^{-4} . In these cases the above mentioned quantities were observed, and when they ceased to change with iterations the solution was deemed to be converged.

4.3.1.9 Aerodynamic Evaluation

The acoustics are built upon the aerodynamics, and for good acoustic predictions the aerodynamics must be resolved adequately enough. The aerodynamic performance of the numerical simulation was validated against experimental data through a PQ-curve where the pressure increase (P) is visualised with respect to the volume flow rate (Q). There was not enough time to perform transient sliding mesh simulations for different flow rates and the pressure increase was instead obtained through steady MRF simulations. The pressure

increase over the centrifugal fan was calculated as the pressure difference between the inlet and outlet boundary. The volume flow rate was monitored at the outlet boundary, taking into considering both the outflow and the reversed flow. The average over 100 iterations after convergence was used for obtaining the pressure and volume flow rate.

4.3.1.10 Summary of Cases

Changing turbulence models, pressure discretization, incompressible/compressible flow together with three different meshes yielded a lot of different simulations to be executed. To be able to get them all done in time only one case was simulated on all three grids, namely, compressible flow, with realizable $k - \varepsilon$ model and the PRESTO scheme as pressure discretization. The comparison between the turbulence models, pressure discretizations and compressible/incompressible flow were all performed on the sector model. A summary of the cases examined is given below.

Table 4.5: Table showing grid and modelling parameters for the various numerical cases simulated in this study.

	Grid	Turbulence Model	Pressure Discretization	Compressibility
Full Domain Models				
Case A	Coarse	Realizable $k - \varepsilon$	PRESTO	Compressible
Case B	Fine	Realizable $k - \varepsilon$	PRESTO	Compressible
Sector Models				
Case D1	Sector	Realizable $k - \varepsilon$	PRESTO	Compressible
Case D2	Sector	$k - \omega$ SST	PRESTO	Compressible
Case E1	Sector	Realizable $k - \varepsilon$	2 nd order CD	Compressible
Case E2	Sector	$k - \omega$ SST	2 nd order CD	Compressible
Case F1	Sector	Realizable $k - \varepsilon$	PRESTO	Incompressible
Case F2	Sector	$k - \omega$ SST	PRESTO	Incompressible

4.3.2 Acoustic Prediction

The acoustic predictions in the far-field have been obtained through the acoustic analogy of Ffowcs-William & Hawking (FW-H). The inhomogeneous wave equation of FW-H consists of monopole, dipole and quadrupole sources, where the monopole and dipole sources usually are mentioned as thickness and loading sources due to their physical nature. In this study, the integration formulation of Brentner and Farassat [49] has been adopted, in which the solution to the inhomogeneous FW-H equation can be written as seen in Equation (4.5). In the mentioned equation, the contribution due to quadrupoles outside of the source region has been neglected, which is a valid approximation when the flow is subsonic [49]. This can be understood more clearly by observing Equation (3.8) and Equation (3.10).

$$p'(\mathbf{x}, t) = p'_T(\mathbf{x}, t) + p'_L(\mathbf{x}, t) \quad (4.5)$$

In the above equation $p' = p - p_0$, and the thickness and loading terms are given by [49]

$$4\pi p'_T(\mathbf{x}, t) = \int_{f=0} \left[\frac{\rho_0 \left(\frac{\partial}{\partial t} (U_i n_i) - U_i \dot{n}_i \right)}{r_i (1 - M_i r_i)^2} \right] dS + \int_{f=0} \left[\frac{\rho_0 U_i n_i \left(r_i \frac{\partial}{\partial t} (M_i r_i) + a_0 (M_i r_i - M_i^2) \right)}{r_i^2 (1 - M_i r_i)^3} \right] dS \quad (4.6)$$

$$4\pi p'_L(\mathbf{x}, t) = \frac{1}{a_0} \int_{f=0} \left[\frac{\frac{\partial}{\partial t} (L_i r_i)}{r_i (1 - M_i r_i)^2} \right] dS + \int_{f=0} \left[\frac{L_i r_i - L_i M_i}{r_i^2 (1 - M_i r_i)} \right] dS + \frac{1}{a_0} \int_{f=0} \left[\frac{L_i r_i \left(r_i \frac{\partial}{\partial t} (M_i r_i) + a_0 (M_i r_i - M_i^2) \right)}{r_i^2 (1 - M_i r_i)^3} \right] dS \quad (4.7)$$

where

$$U_i = v_i + \frac{\rho}{\rho_0} (u_i - v_i)$$

$$L_i = \sigma_{ij} n_j + \rho u_i (u_n - v_n)$$

In the above equations n_i and r_i represent the unit vectors in the wall normal and radiation direction respectively. The reduced solution to the FW-H-equation proposed through equations (4.5)-(4.7) are as the complete FW-H-solution obtained by using Green's free space function. When Green's free space functions is used one neglects any surfaces between sound sources and observer points. The observer points used in this study are located 1.5 [m] above and below the centrifugal fan as seen in Figure 4.7 in scale. It should also be noted that the integrals are evaluated at a retarded time τ , explained in Section 3.2.2.2. The retarded time is dependent of the free field speed of sound. In this study $a_0 = 340$ [m/s], and is calculated through Equation (3.2) with the inlet/outlet temperature listed in Table 4.3. For the incompressible simulations when temperature is not solved for, the same propagation speed was used for a fair comparison. Depending on the study, different surfaces are used for pressure sampling to feed the acoustic analogy. A common choice is to use only the surfaces of the centrifugal fan [36, 45], and sometimes the volute tongue is also included [6, 46]. In the current study, since there is no volute tongue, the pressure was sampled on the centrifugal fan surfaces and on the surfaces related to the impeller inlet. The effects of choosing different source sources were investigated for all numerical cases.

The pressure sampling at the source surfaces could not begin until the flow had reached a quasi-steady state, i.e. when physical quantities start showing a periodic behaviour. Figure 4.6 shows the static pressure difference between inlet and outlet for Case A with respect to simulated time, where a periodic behaviour was reached after approximate 0.25 [s]. Table 4.6 gives the time and revolutions needed to reach periodic behaviour for the other numerical cases. When the flow had reached a developed state, the pressure fluctuations were sampled during six fan revolutions.

The pressure fluctuations sampled during the unsteady calculations were then used to compute the pressure signal at the location of the far-field observer points through Equation (4.5). The observer point downstream of the fan is hereafter referred to as observer point 1 (OP 1) while the observer point located upstream of the fan is referred to as observer point 2 (OP 2).

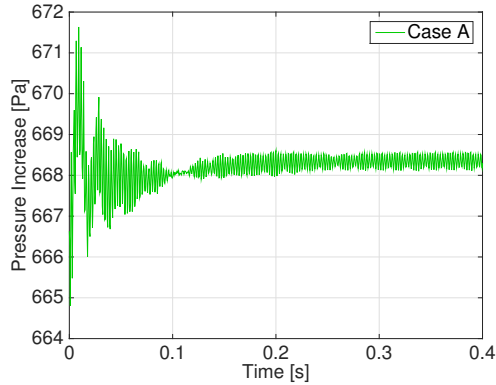


Figure 4.6: Static pressure increase with respect to simulated time for Case A.

Case		Convergence	
		Time	Revolutions
A	$k - \varepsilon$ Real.	0.25	15.16
B	$k - \varepsilon$ Real.	0.2	11.67
D - 1	$k - \varepsilon$ Real.	0.25	14.58
- 2	$k - \omega$ SST	0.2	11.67
E - 1	$k - \varepsilon$ Real.	0.2	11.67
- 2	$k - \omega$ SST	0.18	10.5
F - 1	$k - \varepsilon$ Real.	0.1714	10^1
- 2	$k - \omega$ SST	0.2	14

Table 4.6: Time and number of revolutions until developed flow for the numerical cases.

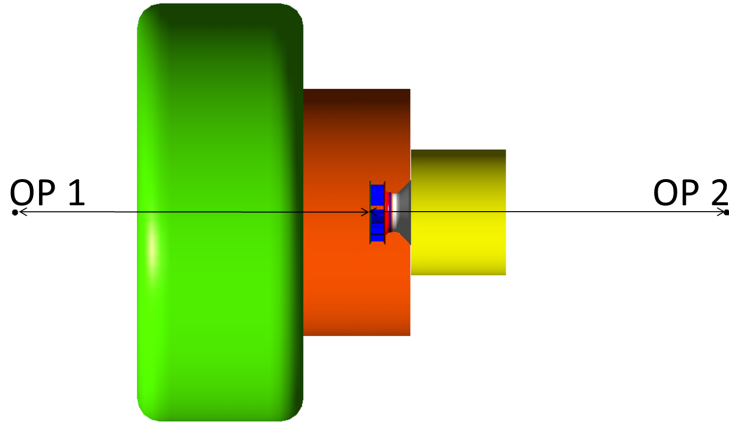


Figure 4.7: Location of OP 1 and OP 2 used in the numerical prediction as well as the experimental measurements.

4.4 Post-Processing

Post-processing involves dealing with the obtained data after the simulations have been performed. In this study, both the aerodynamics and the acoustics were analysed, and the following section gives what was analysed and how it was performed.

¹Due to convergence problems, Case F1 was started from Case F2, and could explain why a converged state could be reached in a quicker time compared to Case F2

4.4.1 Contour Plots

Contour plots were used to analyse the distribution of the mean and fluctuating pressure on the source surfaces. FLUENT has the possibility sample physical quantities during each time step to calculate the mean and *Root Mean Square Error* (RMSE) values. The RMSE value indicates how much a given quantity fluctuates from the mean, by visualising the RMSE value of pressure on the source surfaces the regions responsible for the sound can be located. The time averaging was performed during the last two revolutions of the centrifugal fan when the pressure was sampled for the FW-H propagation.

4.4.2 Frequency Resolution

The sampling of the pressure fluctuations was performed during six fan revolutions, i.e. a total sampling time of 0.10286 [s]. The sample time determines the resolution in the frequency domain through Equation (4.8). The frequency resolution for the numerical simulations can then be calculated to $\Delta f_{sim} = 9.72$ [Hz]. The sampling for the experimental pressure signal was performed during ≈ 4 [s] which yields a frequency resolution of $\Delta f_{exp} = 0.25$ [Hz].

$$\Delta f = \frac{1}{T_s} \quad (4.8)$$

For comparison between the numerical results and the experimental data, the frequency resolution must be the same. The frequency resolution can be reduced with three steps. Divide the complete signal into time segments of equal length as the numerical data, performing the Fourier transform on each time segment and take the average over all segments. With the mentioned procedure, the frequency resolution of the experimental data will match the numerical data and an accurate comparison can be made. Figure 4.8a shows the experimental signal divided into segments of equal time as the numerical simulations and Figure 4.8b shows the first time segment. Figure 4.9 shows the experimental data for the two observer points with two different frequency resolutions. The lower resolution corresponds to the resolution in the numerical simulations.

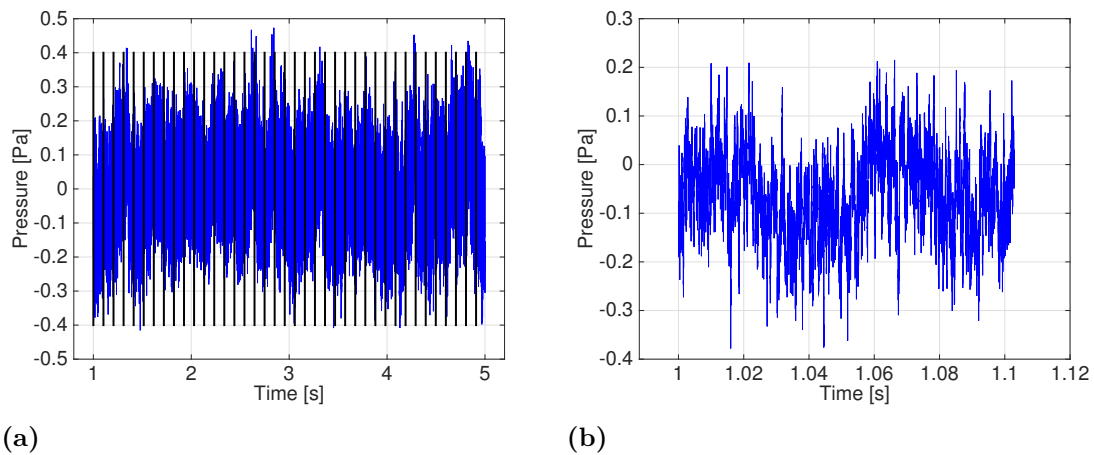


Figure 4.8: The experimental data at OP 1 divided into time segments of equal length as the numerical data (a). The first time segment of the experimental data (b).

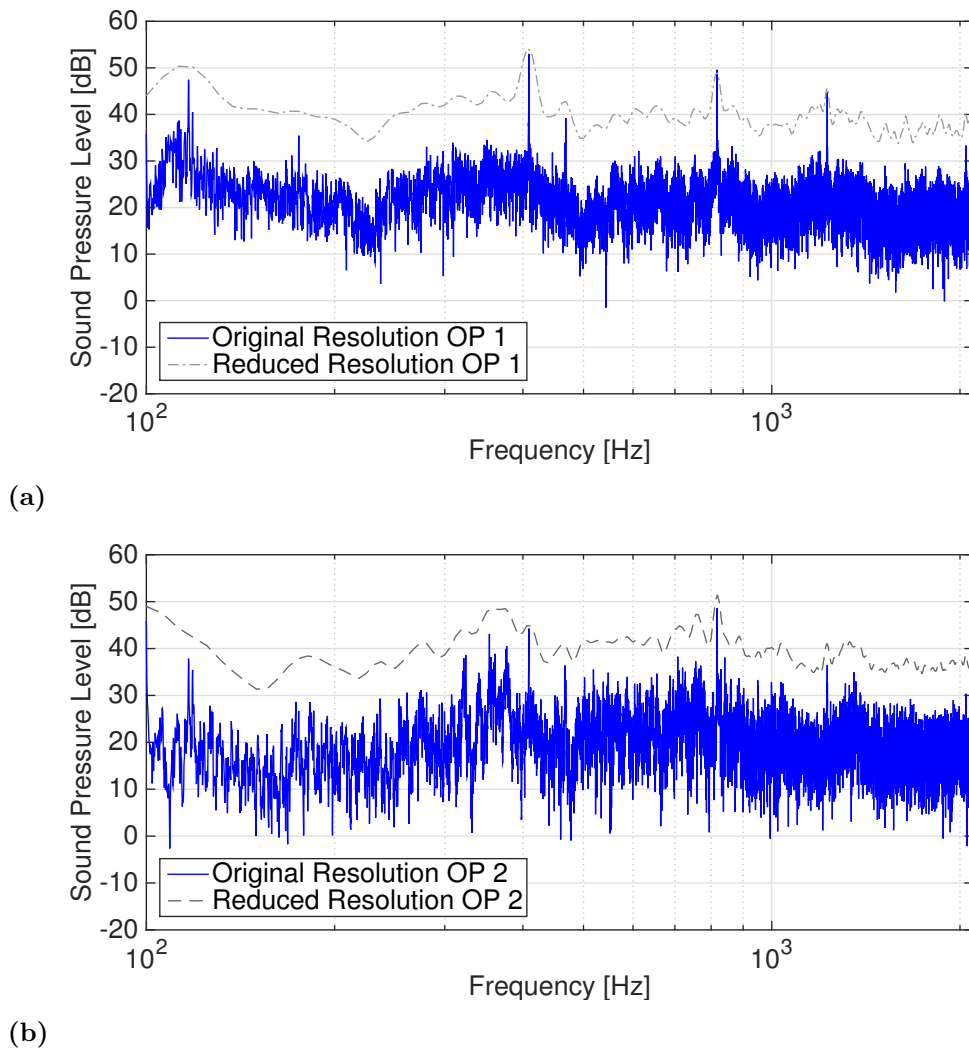


Figure 4.9: Experimental data for OP 1 (a) and OP 2 (b) with two different frequency resolutions. The blue curves have a frequency resolution of $0.25 [Hz]$ while the gray curves have a frequency resolution of $9.27 [Hz]$.

5

Results

This chapter presents the aerodynamic and aeroacoustical results from the numerical simulation cases presented in Section 4.3.1.10. To evaluate the large scale aerodynamics, a PQ-curve is presented for each numerical case and compared with experimental data. The aerodynamic result is finalised by visualising contour plots of the time averaged mean and RMSE pressure field for the three numerical grids. The aeroacoustical results involve fast Fourier transforms of the propagated pressure signals scaled by the reference pressure in air to obtain the sound pressure level. First, the difference between the numerical grids are presented, followed by a comparison between the two turbulence models with different modelling parameters such as pressure discretization and incompressible flow. At the end the two pressure discretizations, and compressible/incompressible flow are compared to each other for a better understanding of their individual effect.

5.1 Aerodynamic Results

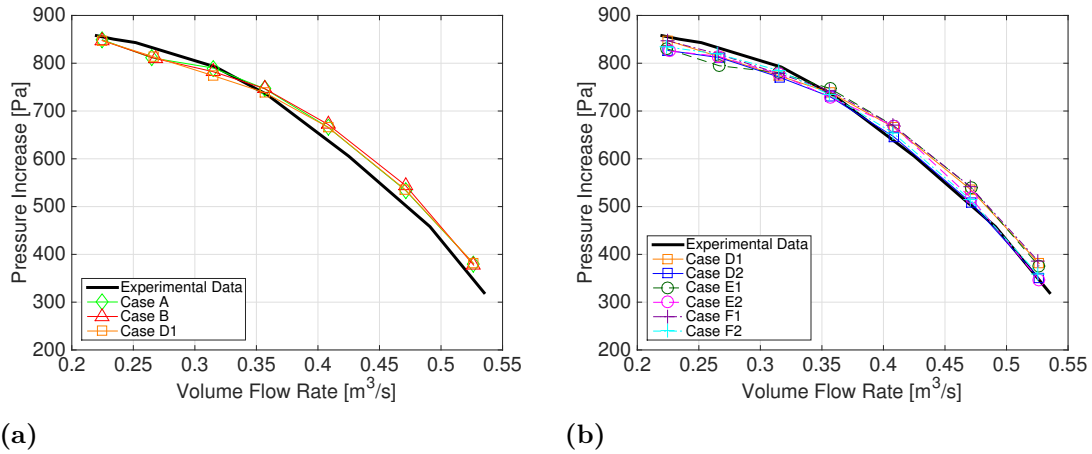


Figure 5.1: PQ curve for the different numerical cases. (a) shows Case A, Case B and Case D1, i.e. three different grids. (b) shows Case D-F, i.e. different model parameters.

Figure 5.1a, shows the PQ-curve for Case A, B and D1. The trend of the three numerical grids are similar and show good agreement with the experimental data. For all cases, the highest agreement is found for a flow rate of $0.36 \text{ [m}^3/\text{s}]$. For lower flow rates, the models under predicts the pressure increase, while at higher flow rates the models over predict the pressure increase. Figure 5.1b shows the PQ-curve for Case D-F, i.e. a comparison between the two turbulence models, pressure discretization and compressible/incompressible

flow. The pressure increase predicted by the $k - \omega$ SST turbulence model shows a higher agreement to the experimental data compared to the Realizable $k - \varepsilon$ turbulence model for most of the flow rates. The predictions made with the PRESTO scheme also shows a better agreement with the experimental data for both turbulence models when compared to the 2nd order CD scheme. The difference between compressible and incompressible flow are minor for both turbulence models. The acoustic predictions were made for the flow rate $Q = 0.408 [m^3/s]$. At the mentioned flow rate the pressure increase and percentage of over prediction is listed in Table 5.1 and visualised in Figure 5.2 ¹.

Table 5.1: Pressure increase over the centrifugal fan at a flow rate of $Q = 0.408$ where the acoustic predictions were made.

		Case									
		Exp.	A	B	D1	D2	E1	E2	F1	F2	
ΔP	[Pa]	638.2	666.1	672.1	666.2	646.6	669.3	669.0	670.2	654.7	
Error	[%]	—	4.4	5.3	4.4	1.3	4.9	4.8	5.0	2.6	

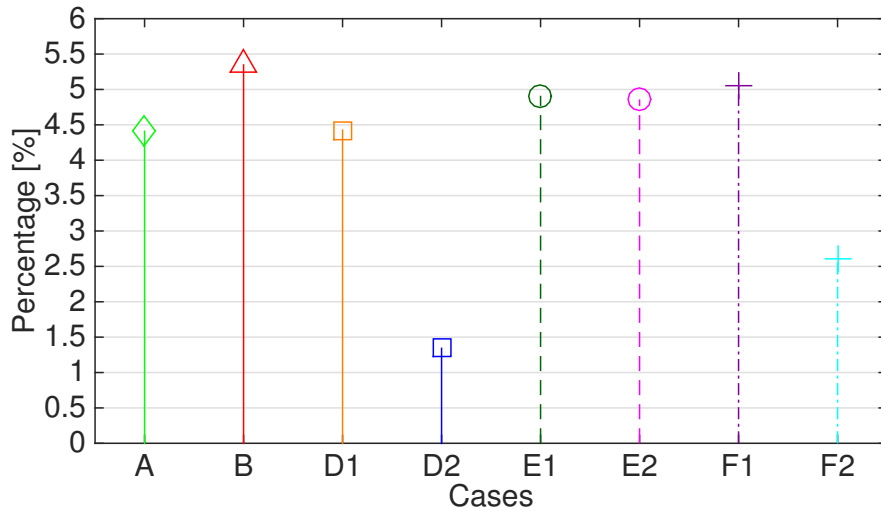


Figure 5.2: Percentage of over prediction at the flow rate where the acoustic predictions were made.

At the volume flow rate of $0.408 [m^3/s]$ the difference in predicted pressure increase between cases A, B and D1 are within 1 % of each other. Case A and D1 shows a slightly higher correspondence towards the experimental data with an over prediction of 4.4 %, while Case B over predicts the pressure increase by 5.3 %. At the mentioned flow rate, the $k - \omega$ SST turbulence model shows a higher agreement towards the experimental data for all numerical cases when compared to the realizable $k - \varepsilon$ turbulence model. The difference between the turbulence models is more pronounced when using the PRESTO scheme for pressure discretization (Case D and Case F). For the 2nd order CD scheme as pressure discretization, i.e. Case E, the difference in predicted pressure increase is negligible between the turbulence models, but worse in comparison to the PRESTO scheme. Overall, Case D2 gives the most accurate prediction with an error of 1.3 %, which increases to 2.6 % when the flow is assumed to be incompressible (Case F2). Switching discretization

¹Over prediction through the following formula, $\frac{P_{Num} - P_{Exp}}{P_{Exp}} \cdot 100$

scheme to the 2nd order CD scheme further increases the error to 4.8 % (Case E2). For the realizable $k - \varepsilon$ model, the difference between Case D1, E1 and F1 is not as pronounced as for the $k - \omega$ SST model. However, Case D1 with the PRESTO scheme yields the highest agreement with an over prediction of 4.4 % which increases to 4.9 % and 5.0 % for the 2nd order CD scheme and incompressible flow respectively.

5.1.1 Time Averaged Pressure - Case A, Case B and Case D1

Figure 5.3 shows the time averaged mean pressure field, and Figure 5.4 the RMSE pressure field at the surfaces used as source surfaces for the acoustic prediction. In the real model, the top of the shroud overlaps the bottom of the impeller inlet as can be seen in Figure 4.2b, for visualisation purposes the impeller inlet has been translated upwards. Case A, Case B and Case D1 is shown from top to bottom. For the Case D1, the entire centrifugal fan as been reconstructed through the periodic boundaries.

Observing the time averaged pressure on the inside of the centrifugal fan and impeller inlet, Figure 5.3a, 5.3c and 5.3e, it is seen that the appearance is almost identical to each other. The only notable difference is for Case A, where there is a slightly larger low pressure area on the leading edge when compared to Case B and Case D1. Observing the outside of the centrifugal fan and impeller inlet in Figure 5.3b, 5.3d and 5.3f, it is again seen that the resemblance towards each other is really high and there are almost no obvious distinctions. Case A and Case B has three distinct pressure contours at the impeller inlet, from dark orange to light orange. For Case D1 there is only two indicating that there is a higher pressure difference between the inside and outside of the impeller inlet for Case D1. It can also be noted that the mean pressure field is entirely symmetric for the full domain models, and visually there is no major difference from the sector model.

Comparing the RMSE value of pressure inside of the centrifugal fan and impeller inlet for Case A and Case B, Figure 5.4a and Figure 5.4c, it is seen that the RMSE pressure field differs on both the inside of the centrifugal fan and impeller inlet. At the impeller inlet, the pressure contours have the shape of arcs for Case A, while for Case B, the pressure field is more smooth, but both cases experience equally large pressure fluctuations at the bottom of the impeller inlet. Considering the centrifugal fan, a large difference between the RMSE pressure fields can be observed for Case A and Case B. Case B shows high RMSE values on the leading edge of the blade, especially close to the backplate, whereas Case A only shows a thin line at the leading edge and trailing edge. Case A does however have a larger area with higher values on the suction side of the blade which is not present for Case B. The pressure field on the shroud also shows a large difference, Case B show clear arcs while Case A does not. It is clearly seen that the entire RMSE pressure field is not symmetric, but the areas of large fluctuations are. Observing the outside of the centrifugal fan and impeller inlet in Figure 5.4b and Figure 5.4d, the pressure field is more alike between the two cases. Case A does however have a larger area of high RMSE values at the trailing edge of the blade that Case B does not have. The RMSE values on the pressure side of the blade are also higher for Case A when compared to Case B.

Observing the inside of the centrifugal fan for the sector model, Figure 5.4e, and comparing it with the two full domain models, Figure 5.4a and Figure 5.4c, a few things can be noted. The the largest fluctuations appear at the leading edge with a similar appearance as Case B. The RMSE pressure field is also more evenly distributed on the suction side of the blade for Case D1 which is not the case for neither Case A and Case B, it is also noted that the magnitude is generally higher with no dark blue areas indicating low fluctuations.

The impeller inlet differs greatly when compared to the full domain models, the RMSE values are higher all over the impeller inlet for Case D1 with the lowest RMSE value being in the range of $\approx 1.5 - 2.5 [Pa]$ as to $0 - 0.625 [Pa]$ for Case A and Case B. Clear high magnitude arcs can also be seen, these arcs coincide with the location of the periodic boundaries. Observing the outside on the centrifugal fan and impeller inlet in Figure 5.4f, a higher resemblance towards Case B can be seen. The high magnitude fluctuations are located at the leading and trailing edge with approximately the same magnitude. The bottom of the impeller inlet also shows high RMSE values for both Case D1 and Case B, but the appearance differs greatly. For Case B the high magnitude area is smooth with distinct transitions, whereas for Case D1, the transition is not as distinct, with arcs as before, and high magnitude "rings".

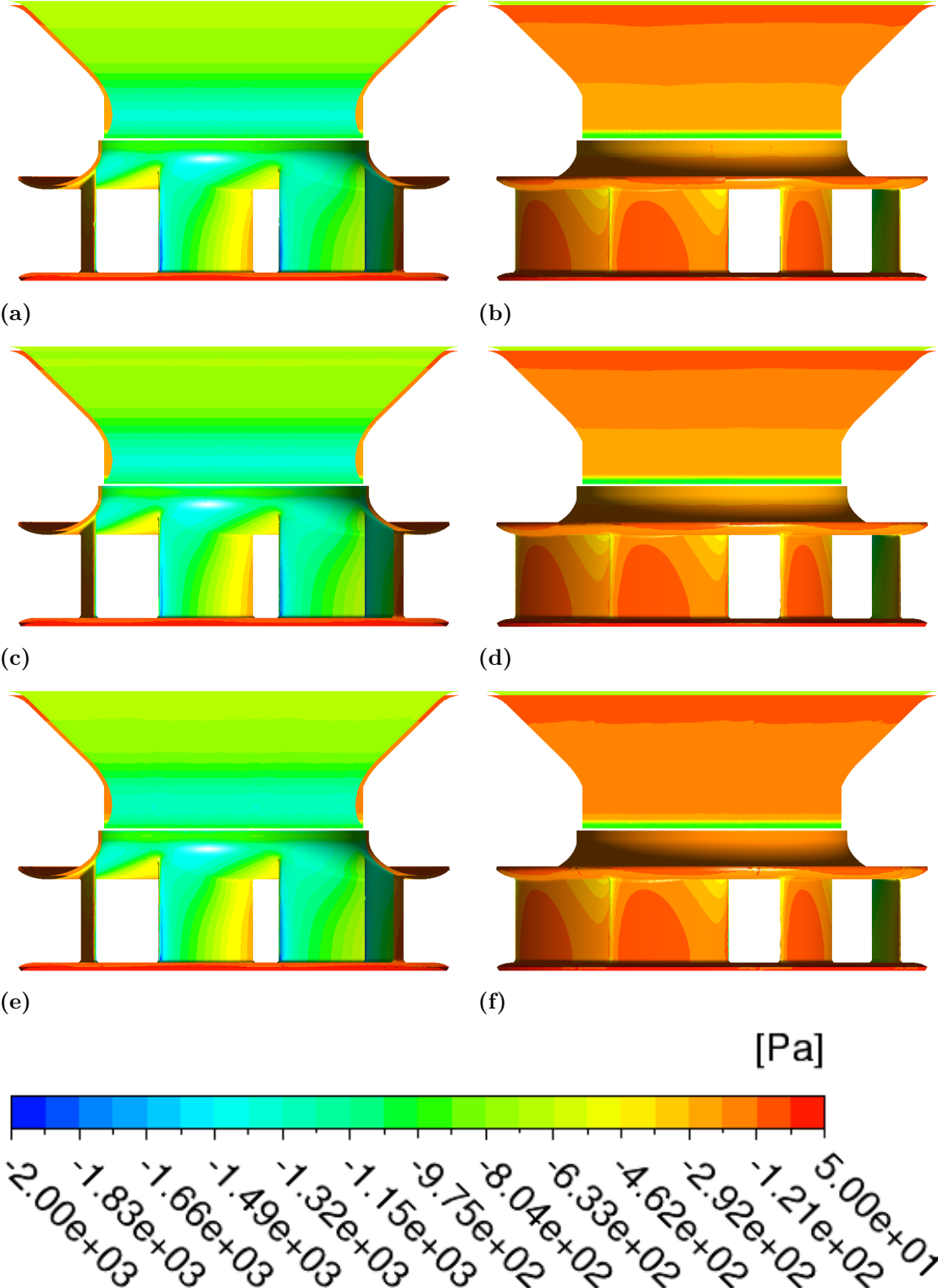


Figure 5.3: Time averaged pressure contours on the surfaces of the centrifugal fan and impeller inlet. Case A - inside (a), outside (b). Case B - inside (c), outside (d). Case D1 - inside (e), outside (f).

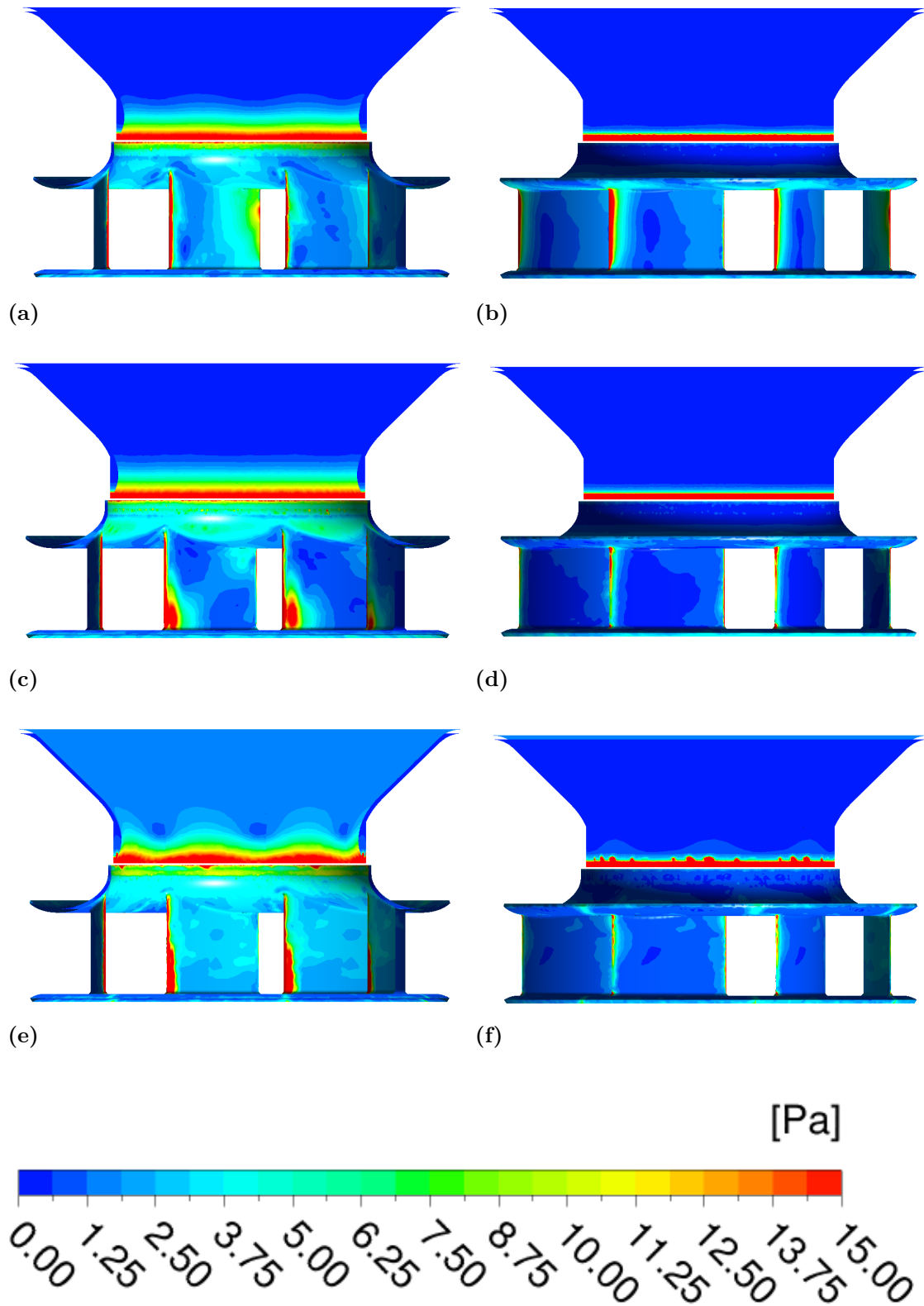


Figure 5.4: RMSE values on the surfaces of the centrifugal fan and the impeller inlet. Case A - inside (a), outside (b). Case B - inside (c), outside (d). Case D1 - inside (e), outside (f).

5.2 Acoustic Results

Figure 5.5a and Figure 5.5b shows the Fourier transform of the experimental pressure signal at the two observer points. The frequency resolution of the signal is decreased to match the numerical simulations as mentioned in Section 4.4.2. At OP 1, Figure 5.5a, the blade passage frequency and its three higher harmonics are clearly seen in the experimental data, as well as a prominent tone at 120 [Hz]. Slightly above the blade passage frequency, there is a less distinguishable but still noticeable tone as well. At OP 2, Figure 5.5b, the sound characteristics are different from OP 1. The blade passage frequency is not as pronounced as a tone at a slightly lower frequency. The first harmonic is more distinct, and the sound pressure level is even higher compared to the first harmonic at OP 1. There are two noticeable tones in the vicinity of the first harmonic, one below and one above. Both the second and third harmonic can be seen in the spectrum, but there are also several tones slightly above both harmonics. Table 5.2 gives the experimental sound pressure levels at the blade passage frequency and the three higher harmonics for the two observer points.

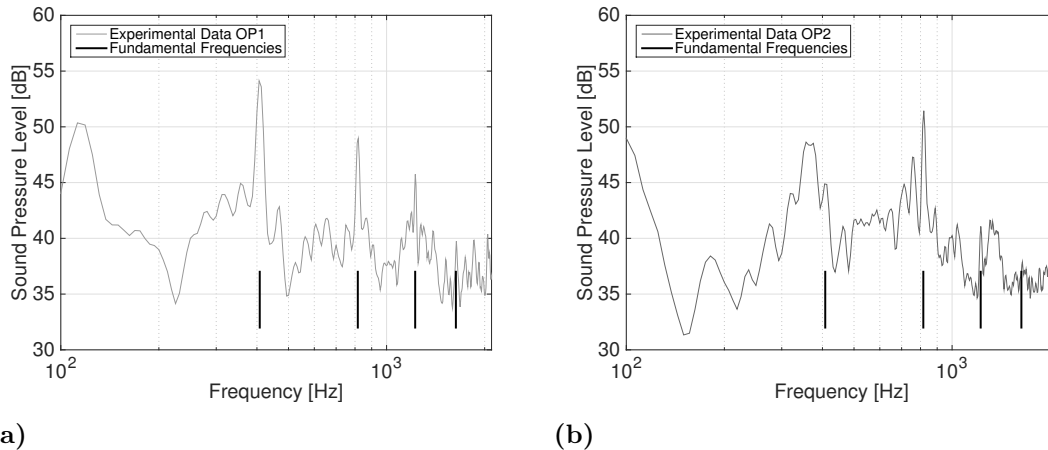


Figure 5.5: Fast fourier transform of the experimental pressure signals at OP 1 (a) and OP 2 (b).

Table 5.2: Experimental sound pressure levels at the blade passage frequency and the three higher harmonics for OP 1 and OP 2.

		BPF	1 st Harmonic	2 nd Harmonic	3 rd Harmonic
		408 [Hz]	816 [Hz]	1224 [Hz]	1632 [Hz]
Exp.	OP 1	54.13	48.95	45.75	39.74
Exp.	OP 2	44.88	51.44	41.07	37.88

5.2.1 Comparison Between the Numerical Grids

The three first cases consists of the compressible, realizable $k - \varepsilon$ turbulence model and pressure discretized with the PRESTO scheme on the three numerical grids. Figure 5.6 shows the frequency spectrum for OP 1 while Figure 5.7 shows the frequency spectrum for OP 2. Table 5.3, gives the sound pressure levels at the blade passage frequency and

the three higher harmonics for OP 1 and is visualised in Figure 5.8a-5.8b. Sound pressure levels for the blade passage frequency and the higher harmonics for OP 2 are listed in Table 5.4 and is visualised in Figure 5.8c-5.8d.

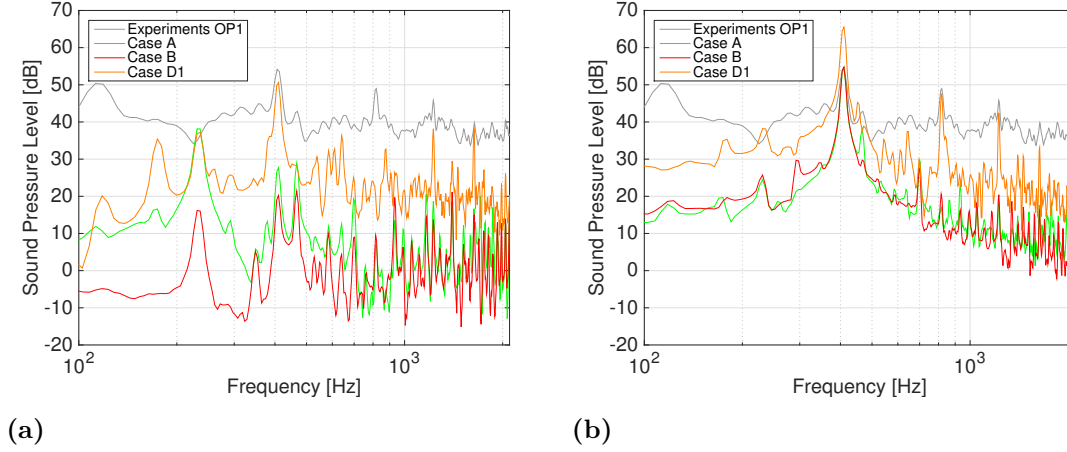


Figure 5.6: Fast Fourier transform of the propagated pressure signals at OP 1 for Case A, Case B and Case D1. In (a), only the centrifugal fan surfaces are used as source surfaces. In (b), centrifugal fan and impeller inlet are used as source surfaces.

At OP 1, using only the centrifugal fan as source surface, Figure 5.6a, the sound pressure levels are under predicted on all numerical grids. Great similarities are found between the two full domain cases, Case A and Case B. A distinct tone is found at 250 [Hz] which is not present in the experimental data. Both cases predict the blade passage frequency and the tone slightly above but with a severe under prediction of the sound pressure levels. The higher harmonics are not distinguishable and are masked together with multiple frequencies of more or less equal amplitude. The sector model, Case D1, also predicts the tone at 250 [Hz] and with similar amplitude as Case A. The blade passage frequency is accurately predicted, but the amplitude is under predicted by 3.50 [dB]. The tone just above the blade passage frequency is not predicted by the sector model as it is by the full domain models. As for Case A and Case B, Case D1 also fails to predict the first harmonic of the blade passage frequency but captures another tone slightly above which is not visible in the experimental data. The second harmonic is captured, but the amplitude is under predicted by 7.59 [dB]. The third harmonic is more accurately predicted with an under prediction of 1.69 [dB]. By using the centrifugal fan and impeller inlet as source surfaces a different result is obtained, see Figure 5.6b. With the different source surfaces, Case A and Case B now accurately predicts the blade passage frequency within 0.7 [dB] whereas Case D1 now shows an over prediction of 11.37 [dB]. Case A and case D1 also captures the tone slightly above the blade passage frequency while Case B does not. Case A and Case B still do not capture the higher harmonics with any accuracy, but Case D1 does. With the different source surfaces, Case D1 now predicts the first harmonic within 1.53 [dB], the second harmonic within 3.29 [dB] and third harmonic within 6.62 [dB].

At OP 2, using only the centrifugal fan surfaces as source surfaces, Figure 5.7a, Case A and Case B show similar behaviour as for OP 1. The two cases predict more or less the same frequencies but with different amplitudes. Neither of the mentioned cases are able to predict the prominent tone just below the blade passage frequency. Similar to OP 1, the blade passage frequency is captured by the sector model, but at this location the sound pressure level is over predicted. The first harmonic is not captured with any accuracy as

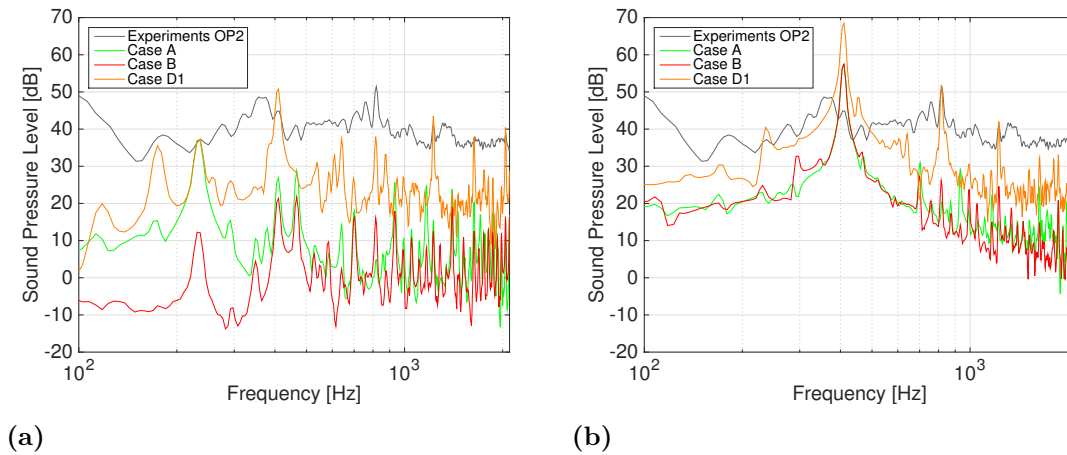


Figure 5.7: Fast Fourier transform of the propagated pressure signals at OP 2 for Case A, Case B and Case D1. In (a), only the centrifugal fan surfaces are used as source surfaces. In (b), centrifugal fan and impeller inlet are used as source surfaces.

for OP 1, however, it is noticeable for Case D1, but the amplitude is far off. The second and third harmonic are predicted with more accuracy, the second within 2.44 [dB] and the third within 0.13 [dB]. With the centrifugal fan and impeller inlet as source surfaces, Figure 5.7b, all cases severely over predict the blade passage frequency. As for OP 1, neither Case A or Case B are able to capture the higher harmonics whereas the sector model is able to predict the first, second and third harmonic within 0.13 [dB], 0.96 [dB] and 5.42 [dB] respectively.

Table 5.3: Sound pressure level at the blade passage frequency and the three higher harmonics for Case A-C at OP 1.

Source Surface		BPF	1 st Harmonic	2 nd Harmonic	3 rd Harmonic
Exp. OP 1		54.13	48.95	45.78	39.74
Case A	Fan	27.73	6.88	18.65	17.58
Case B	Fan	20.23	9.44	13.72	15.10
Case D1	Fan	50.63	23.23	38.16	38.05
Case A	Fan, Imp. Inlet	54.49	17.00	18.17	17.66
Case B	Fan, Imp. Inlet	54.81	20.58	20.41	16.23
Case D1	Fan, Imp. Inlet	65.50	47.42	42.45	33.12

Table 5.4: Sound pressure level at the blade passage frequency and the three higher harmonics for Case A-C at OP 2.

Source Surface		BPF	1 st Harmonic	2 nd Harmonic	3 rd Harmonic
Exp. OP 2		44.88	51.44	41.07	37.88
Case A	Fan	26.87	4.89	15.41	20.28
Case B	Fan	21.38	16.01	12.45	12.58
Case D1	Fan	50.78	37.93	43.47	37.76
Case A	Fan, Imp. Inlet	57.28	20.56	14.90	24.22
Case B	Fan, Imp. Inlet	57.49	26.11	24.60	14.70
Case D1	Fan, Imp. Inlet	68.41	51.31	42.03	32.46

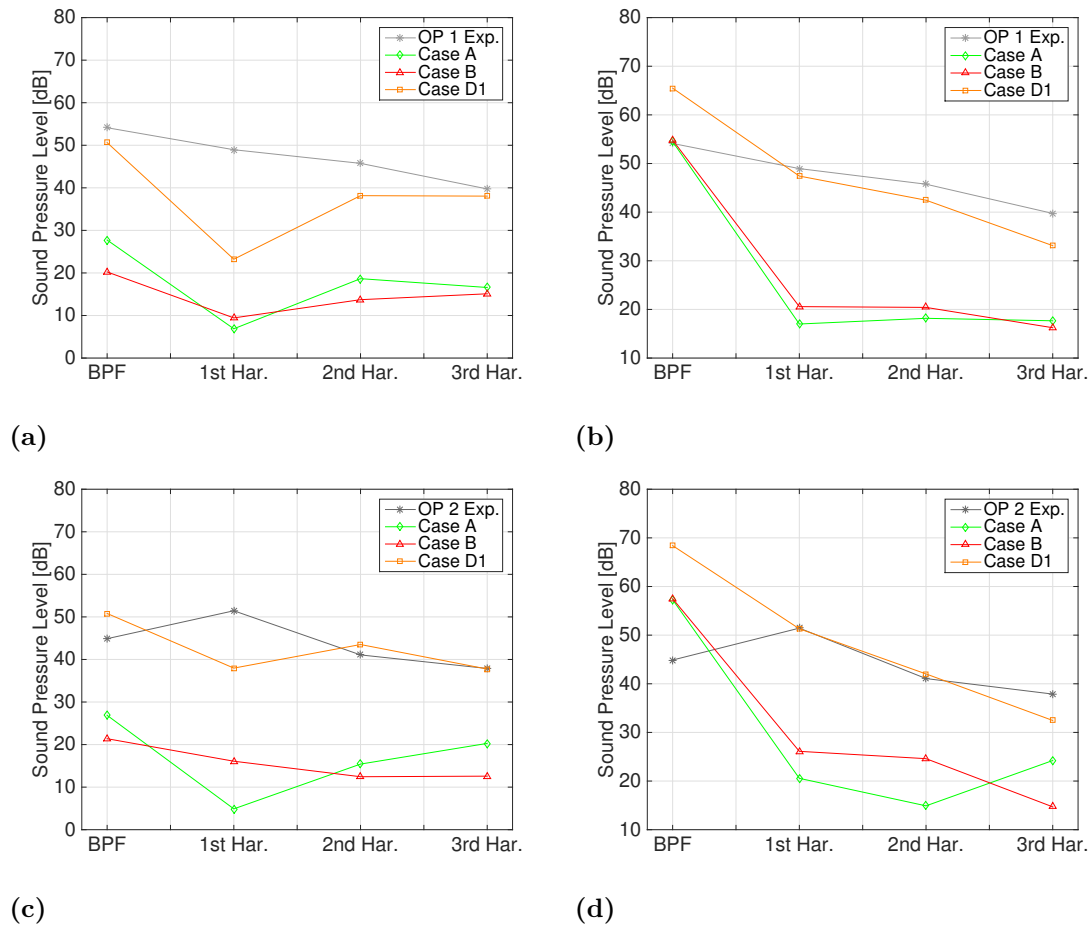


Figure 5.8: Sound pressure level at the blade passage frequency and the three higher harmonics for Case A, Case B and Case D1 at OP 1 (a-b) and OP 2 (c-d). In (a) and (c), only the centrifugal fan surfaces are used as source surfaces. In (b) and (d), centrifugal fan and impeller inlet are used as source surfaces.

Observing OP 1 in Figure 5.8a-5.8b it can be seen that the selection of source surfaces greatly influence the propagated sound. Case A and B are able to accurately predict the blade passage frequency but not the higher harmonics. Case D1 shows a major over prediction for the blade passage frequency, but the trend for the higher harmonics is satisfactory. Observing OP 2 in Figure 5.8c - 5.8d, it can be seen that neither of the numerical cases exhibit a clear resemblance towards the experimental data regarding the trend, where the sound pressure level is higher for the first harmonic than for the blade passage frequency. But for absolute values, case D1 is relatively close for the higher harmonics while Case A and Case B are not.

5.2.2 Comparison Between Case D1 and Case D2

In the following section, the $k - \omega$ SST turbulence model is introduced, (Case D2), and compared with the Realizable $k - \varepsilon$ model, (Case D1). Figure 5.9 shows the propagated sound pressure levels to OP 1, and Figure 5.10 shows the propagated sound pressure levels to OP 2. Table 5.5 gives the sound pressure level at the blade passage frequency and the three higher harmonics at OP 1 and is visualised in Figure 5.11a-5.11b. Table 5.6 gives

the sound pressure levels at the blade passage frequency and the higher harmonics at OP 2, and is visualised in Figure 5.11c-5.11d.

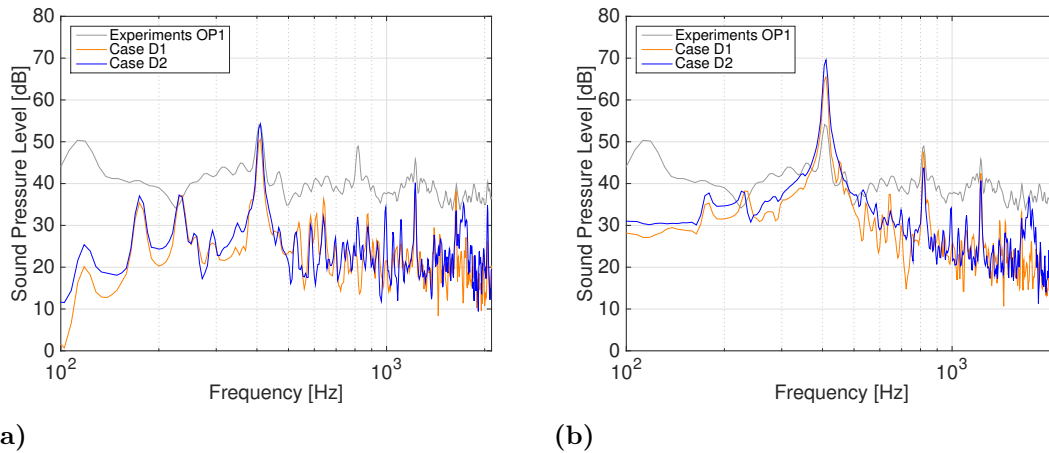


Figure 5.9: Fast Fourier transform of the propagated pressure signals at OP 1 for Case D1 and Case D2. In (a), only the centrifugal fan surfaces are used as source surfaces. In (b), centrifugal fan and impeller inlet are used as source surfaces.

Visualising the propagated sound pressure at OP 1 with the centrifugal fan as source surface, Figure 5.9a, a high resemblance between the two turbulence models can be observed. Both models predict the blade passage frequency with reasonable accuracy. The prediction by Case D2 is within $0.14 [dB]$ from the experimental data as to $3.50 [dB]$ for Case D1. Case D2 also fails to predict the first harmonic with any accuracy and both models shows results far from the experimental sound pressure level. For the second harmonic, Case D2 gives a slightly better prediction compared to Case D1, with $5.57 [dB]$ off compared to $7.59 [dB]$. For the third harmonic the predictions made by Case D1 shows a higher resemblance towards the experimental data with a prediction within $1.69 [dB]$ as compared to $6.22 [dB]$ for Case D2. When the centrifugal fan and impeller inlet are used as source surfaces, Figure 5.9b the blade passage frequency is now over predicted for both cases, and especially for Case D2. Case D2 also shows a lower resemblance for the higher harmonics when compared to Case D1, being off by more than $5 [dB]$. With only the centrifugal fan as source surface, the results by Case D2 shows a higher correspondence to the experimental data for all fundamental frequencies except the third harmonic, see Figure 5.11a, in comparison with Case D1. But with the centrifugal fan and impeller inlet as source surface, the sound pressure levels are more accurately predicted by Case D1 for all fundamental frequencies when compared to Case D2, and is clearly seen in Figure 5.11b.

Observing the sound pressure levels at OP 2 with the centrifugal fan as source surface, Figure 5.10a, the results between the two cases are equally similar as for OP 1. The two models over predicts the blade passage frequency and the second harmonic, whereas the third harmonic is over predicted by Case D2 and under predicted by Case D1. As for OP 1, neither of the two cases are able to accurately capture the first harmonic and the tone below the blade passage frequency. The error in sound pressure levels are slightly higher for Case D2 when compared to Case D1, see Figure 5.11c. The error in sound pressure levels are $9.02 [dB]$, $4.43 [dB]$ and $1.31 [dB]$ compared to $5.92 [dB]$, $2.44 [dB]$ and $0.13 [dB]$ for the blade passage frequency, the second and third harmonic for Case D2 and Case D1 respectively. Using the centrifugal fan and impeller inlet as source surfaces,

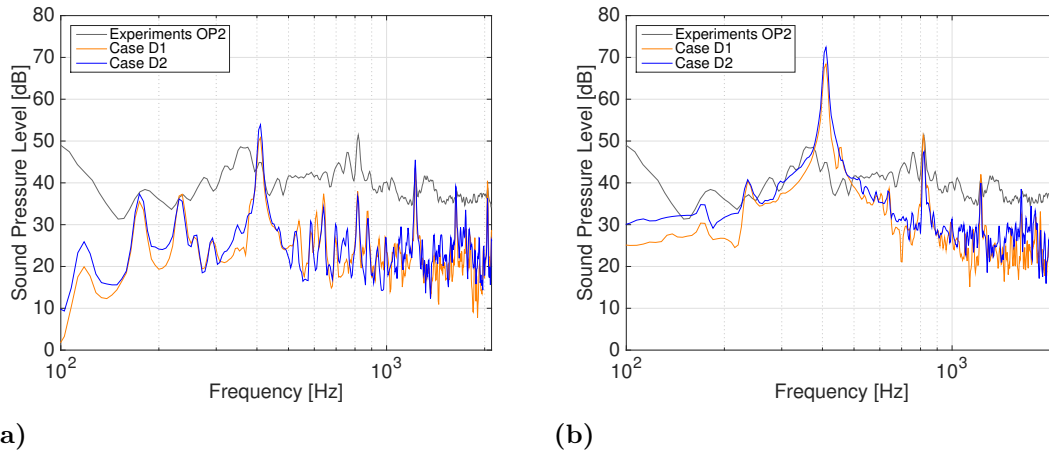


Figure 5.10: Fast Fourier transform of the propagated pressure signals at OP 2 for Case D1 and Case D2. In (a), only the centrifugal fan surfaces are used as source surfaces. In (b), centrifugal fan and impeller inlet are used as source surfaces.

Figure 5.10b, the blade passage frequency is clearly noticeable but severely over predicted for both cases, with Case D2 predicting the highest sound pressure level. The first and second harmonic are more accurately predicted by Case D1, with the sound pressure levels being predicted within 0.13 [dB] and 0.96 [dB] whilst the prediction by Case D2 are off by 3.98 [dB] and 1.09 [dB]. For the third harmonic Case D2 are closer to the experimental data with 0.65 [dB] off as to 5.42 [dB] for Case D1. Observing Figure 5.11d, it can be seen that Case D1 is closer then Case D2 for the first and second harmonic, but the general trend is more accurately captured for Case D2.

Table 5.5: Sound pressure level at the blade passage frequency and the three higher harmonics for Case D at OP 1.

Source Surface		BPF	1 st Harmonic	2 nd Harmonic	3 rd Harmonic
Exp. OP 1		54.13	48.95	45.78	39.74
Case D1	Fan	50.63	23.23	38.16	38.05
Case D2	Fan	54.27	32.03	40.18	33.52
Case D1	Fan, Imp. Inlet	65.50	47.42	42.45	33.12
Case D2	Fan, Imp. Inlet	69.55	43.73	40.69	31.71

Table 5.6: Sound pressure level at the blade passage frequency and the three higher harmonics for Case D at OP 2.

Source Surface		BPF	1 st Harmonic	2 nd Harmonic	3 rd Harmonic
Exp. OP 2		44.88	51.44	41.07	37.88
Case D1	Fan	50.81	37.97	43.51	37.75
Case D2	Fan	53.90	36.76	45.50	39.19
Case D1	Fan, Imp. Inlet	68.41	51.31	42.03	32.46
Case D2	Fan, Imp. Inlet	72.40	47.46	39.98	38.53

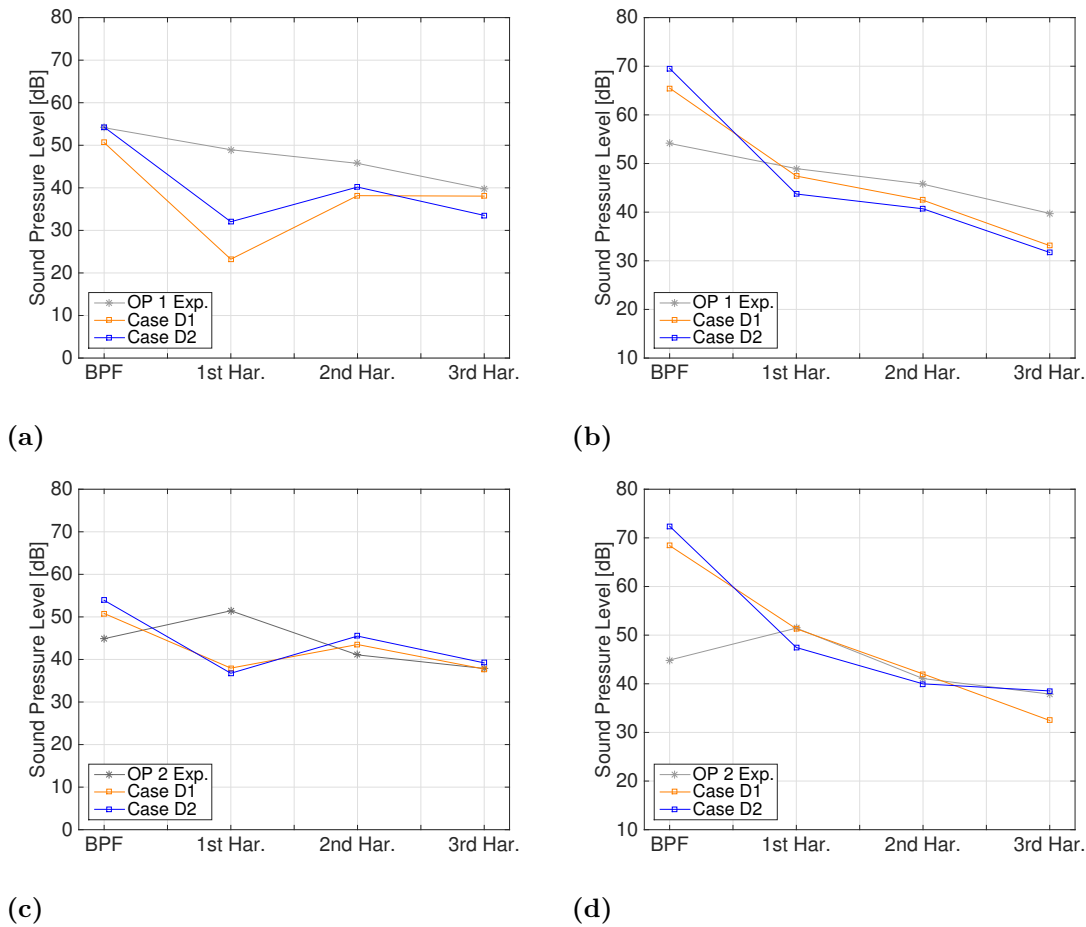


Figure 5.11: Sound pressure level at the blade passage frequency and the three higher harmonics for Case D1 and Case D2 at OP 1 (a-b) and OP 2 (c-d). In (a) and (c), only the centrifugal fan surfaces are used as source surfaces. In (b) and (d), centrifugal fan and impeller inlet are used as source surfaces.

5.2.3 Comparison Between Case E1 and Case E2

In the following section the pressure is discretized with the 2^{nd} order CD scheme for the realizable $k - \varepsilon$ model (Case E1) and $k - \omega$ SST model (Case E2). Figure 5.12 and Figure 5.13 shows the propagated sound pressure levels to OP 1 and OP 2 respectively. Table 5.7 gives the sound pressure levels at the blade passage frequency and the three higher harmonics for OP 1 and is visualised in Figure 5.14a - 5.14b for different source surfaces. Table 5.8 gives the sound pressure levels at OP 2, and is visualised in Figure 5.14c - 5.14d for different source surfaces.

Observing OP 1 in Figure 5.12a with the centrifugal fan as source surfaces, it can be seen that both models show very similar behaviour for frequencies below blade passage frequency. At the blade passage frequency the two models clearly under predicts the sound pressure level. Case E1 with approximately 5.9 [dB] and Case E2 with approximately 9.6 [dB]. The first harmonic is not noticeable for Case E1 where it is surrounded by multiple frequencies of equal amplitude. For Case E2, this is not the case and the first harmonic is clearly seen, albeit gravely under predicted. The prediction of the second harmonic shows a higher resemblance between the cases, with Case E2 showing the highest

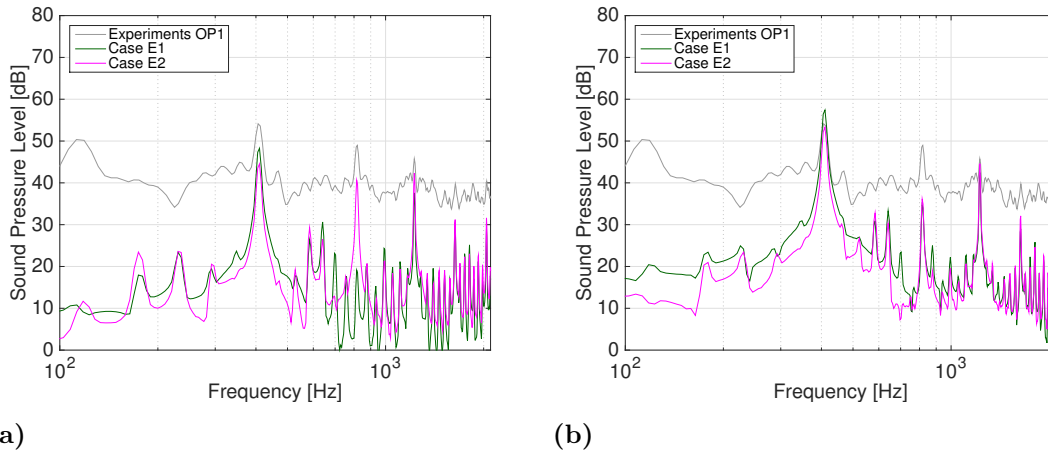


Figure 5.12: Fast Fourier transform of the propagated pressure signals at OP 1 for Case E1 and Case E2. In (a), only the fan surfaces are used as source surfaces. In (b), fan and impeller inlet are used as source surfaces.

level of correspondence with a difference of 3.43 [dB] compared to 8.18 [dB] for Case E1. For the third harmonic the two cases yields almost the same sound pressure level but differ with more than 8.5 [dB] to the experimental data. Observing Figure 5.14a, it is seen that the general trend is more accurately captured by Case E2, even though the blade passage frequency is further away from the experimental data. Switching to the centrifugal fan and impeller inlet as source surfaces, Figure 5.12b, the two cases shows a higher resemblance towards each other then with only the centrifugal fan as source surfaces. The same frequencies are predicted with only slight differences in the sound pressure levels, see Figure 5.14b. In the mentioned figure, it is seen that Case E2 shows better results for the blade passage frequency and the second harmonic, and that the two cases are equally bad for the first and third harmonic. The blade passage frequency and the second harmonic is predicted within 0.84 [dB] and 1.15 [dB] for Case E2 as to 3.28 [dB] and 3.29 [dB] respectively for Case E1. For the first harmonic, the accuracy decreases for Case E2 while it increases for Case E1, but both cases are far from the experimental data. Considering the third harmonic, changing source surfaces gives minor effects on the predicted sound pressure levels for the two cases, with differences of about 1 [dB] each.

At OP 2 with the centrifugal fan as source surface, Figure 5.13a, the similarities between Case E1 and Case E2 are higher in comparison to OP 1. The two cases predicts almost exactly the same frequencies with similar amplitudes. For the blade passage frequency Case E2 is 1.41 [dB] off as to 3.12 [dB] for Case E1, the sound pressure level of the first harmonic is almost identical between the models despite a high level of under prediction. For the second harmonic, the sound pressure levels predicted by Case E1 are closer to the experimental data and vice versa for the third harmonic, see Figure 5.14c. By switching source surfaces, Figure 5.13b, neither of the cases shows good agreement for the blade passage frequency and the first harmonic with a considerate over prediction and under prediction respectively, see Figure 5.14d. The second harmonic are more accurately predicted, especially for Case E1 with 0.72 [dB] off as to 2.8 [dB] for Case E2.

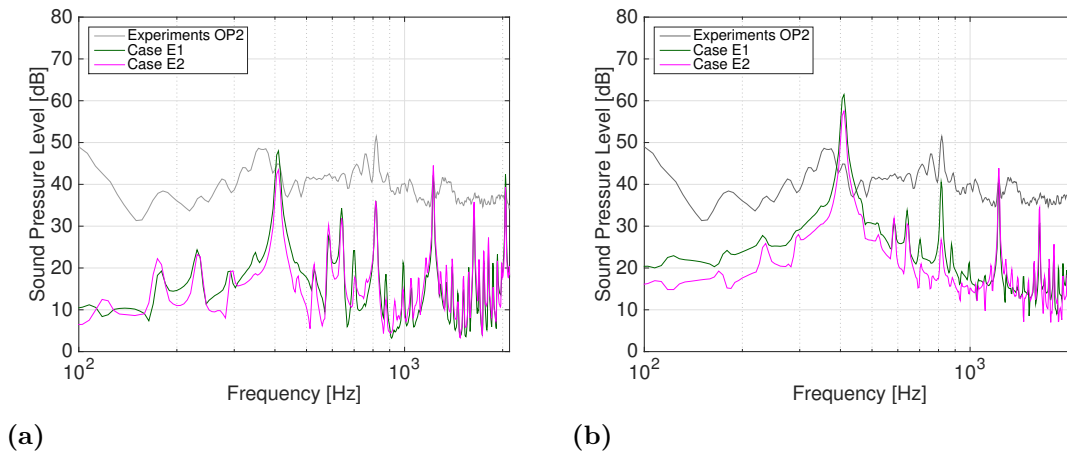


Figure 5.13: Fast Fourier transform of the propagated pressure signals at OP 2 for Case E1 and Case E2. In (a), only the centrifugal fan surfaces are used as source surfaces. In (b), centrifugal fan and impeller inlet are used as source surfaces.

Table 5.7: Sound pressure level at the blade passage frequency and the three higher harmonics for Case E at OP 1.

	Source Surface	BPF	1 st Harmonic	2 nd Harmonic	3 rd Harmonic
Exp. OP 1		54.13	48.95	45.78	39.74
Case E1	Fan	48.27	19.15	37.60	30.39
Case E2	Fan	44.53	40.65	42.35	31.21
Case E1	Fan, Imp. Inlet	57.41	34.72	42.46	29.00
Case E2	Fan, Imp. Inlet	53.29	36.11	44.59	32.10

Table 5.8: Sound pressure level at the blade passage frequency and the three higher harmonics for Case D at OP 2.

	Source Surface	BPF	1 st Harmonic	2 nd Harmonic	3 rd Harmonic
Exp. OP 2		44.88	51.44	41.07	37.88
Case E1	Fan	48.00	36.06	42.16	33.73
Case E2	Fan	43.47	36.04	44.51	35.79
Case E1	Fan, Imp. Inlet	61.45	40.51	40.35	30.81
Case E2	Fan, Imp. Inlet	57.54	26.75	43.87	34.46

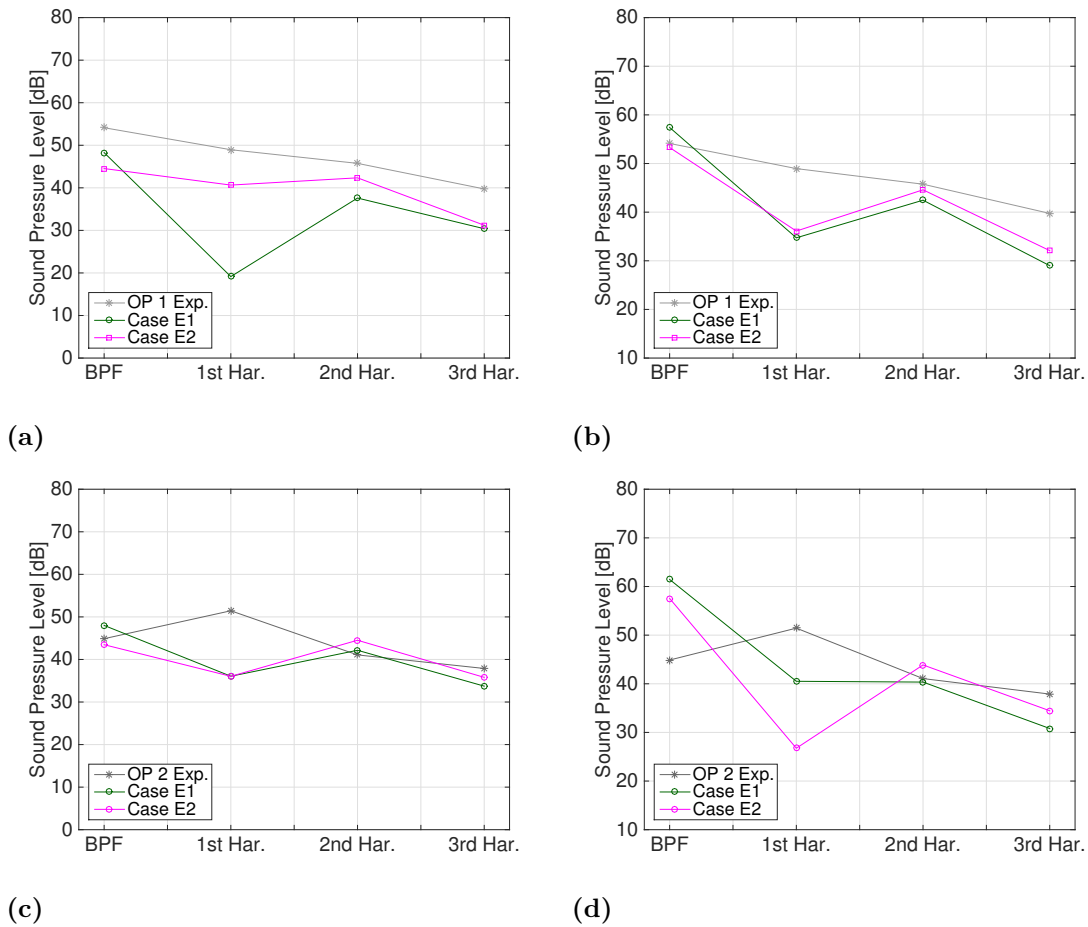


Figure 5.14: Sound pressure level at the blade passage frequency and the three higher harmonics for Case E1 and Case E2 at OP 1 (a-b) and OP 2 (c-d). In (a) and (c), only the centrifugal fan surfaces are used as source surfaces. In (b) and (d), centrifugal fan and impeller inlet are used as source surfaces.

5.2.4 Comparison Between Case F1 and Case F2

In the following section the two turbulence models, realizable $k - \varepsilon$ (Case F2) and $k - \omega$ SST (Case F2), are run with the assumption of incompressible flow. Figure 5.15 and Figure 5.16 gives the sound pressure levels with respect to frequency for OP 1 and OP 2. Table 5.9 gives the sound pressure levels for the blade passage frequency and the higher harmonics for OP 1, and is visualised in Figure 5.17a-5.17b. Table 5.10 gives the sound pressure levels for OP 2 and is visualised in Figure 5.17c-5.17d.

Observing OP 1 with the centrifugal fan as source surface, Figure 5.15a, great similarities are found between the two turbulence models. The sound pressure levels at blade passage frequency and the first harmonic are under predicted by both turbulence models, but Case F2 shows a slightly higher sound pressure level for the mentioned frequencies. For the second harmonic, the prediction in sound pressure level is almost identical between the models, approximately 2 [dB] under the experimental values. For the third harmonic, Case F1 shows an over prediction of roughly 3 [dB] while Case F2 shows an under prediction of about 5 [dB]. Including the impeller inlet as source surface, the baseline is increased, resulting in an over prediction at the blade passage frequency and an accurate prediction

at the first harmonic. It can also be noted that the tone slightly above the blade passage frequency is captured by both models. At around $1100 [Hz]$, the sound pressure levels in frequency spectrum starts to increase, and both the higher harmonics are far from the experimental values. Visualising Figure 5.17a - 5.17b, it is seen that the non of the turbulence models are able to capture the trend of the experimental data.

Observing OP 2 with the centrifugal fan as source surface, Figure 5.16a, the similarities between the models are equally great as for OP 1. The same frequencies are found throughout the spectrum and the sound pressure levels are of roughly equal amplitude. At OP 2, the sound pressure level at the blade passage frequency is accurately predicted for both models, within $1 [dB]$. But all the higher harmonics are relatively far off the experimental data, this is clearly seen in Figure 5.17c. Switching source surface, the trend is roughly about the same as for OP 1. The baseline is increased, resulting in an over prediction for the blade passage frequency but an accurate prediction for the first harmonic. The sound pressure levels start to greatly deviate from the experimental values above $1100 [Hz]$, see Figure 5.17d.

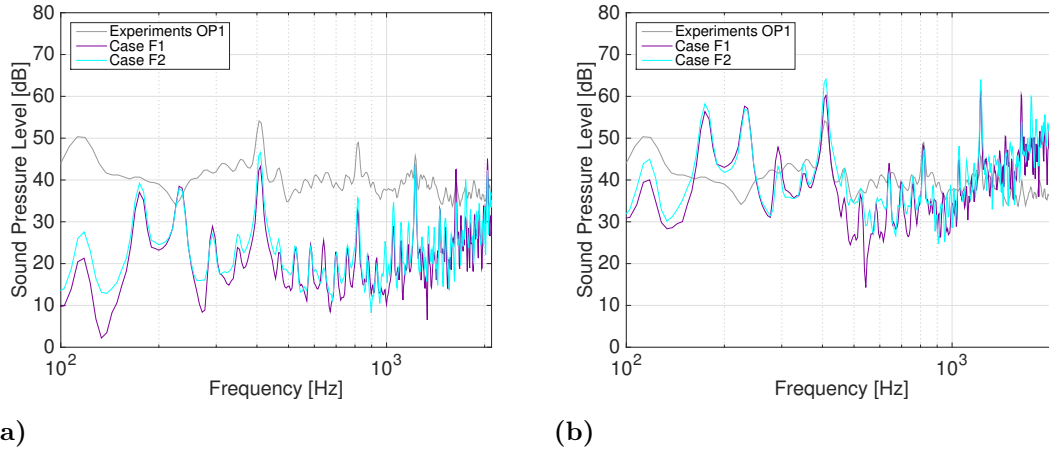


Figure 5.15: Fast Fourier transform of the propagated pressure signals at OP 1 for Case F1 and Case F2. In (a), only the centrifugal fan surfaces are used as source surfaces. In (b), centrifugal fan and impeller inlet are used as source surfaces.

Table 5.9: Sound pressure level at the blade passage frequency and the three higher harmonics for Case F at OP 1.

	Source Surface	BPF	1 st Harmonic	2 nd Harmonic	3 rd Harmonic
Exp. OP 1		54.13	48.95	45.78	39.74
Case F1	Fan	43.23	32.77	43.76	42.54
Case F2	Fan	46.59	35.75	43.89	34.58
Case F1	Fan, Imp. Inlet	60.20	48.24	61.40	60.25
Case F2	Fan, Imp. Inlet	64.06	47.05	64.03	53.93

5. Results

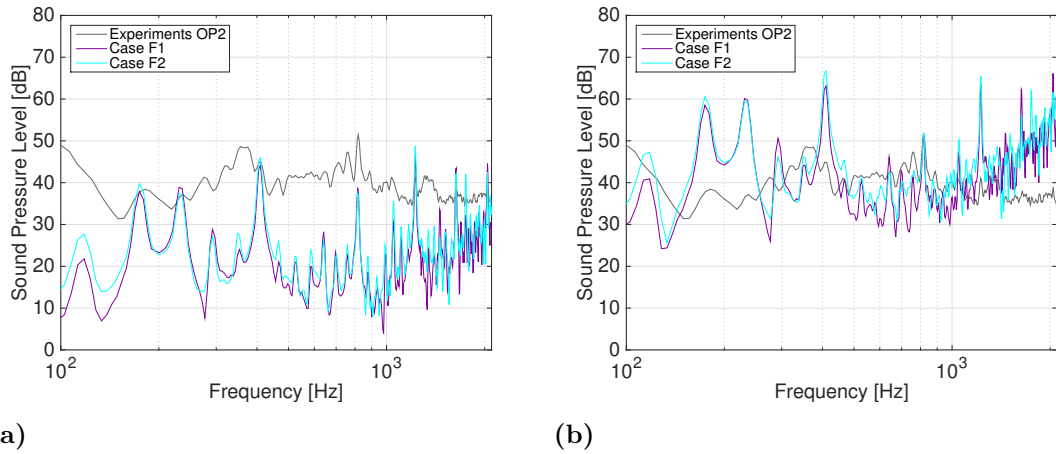


Figure 5.16: Fast Fourier transform of the propagated pressure signals at OP 2 for Case F1 and Case F2. In (a), only the centrifugal fan surfaces are used as source surfaces. In (b), centrifugal fan and impeller inlet are used as source surfaces.

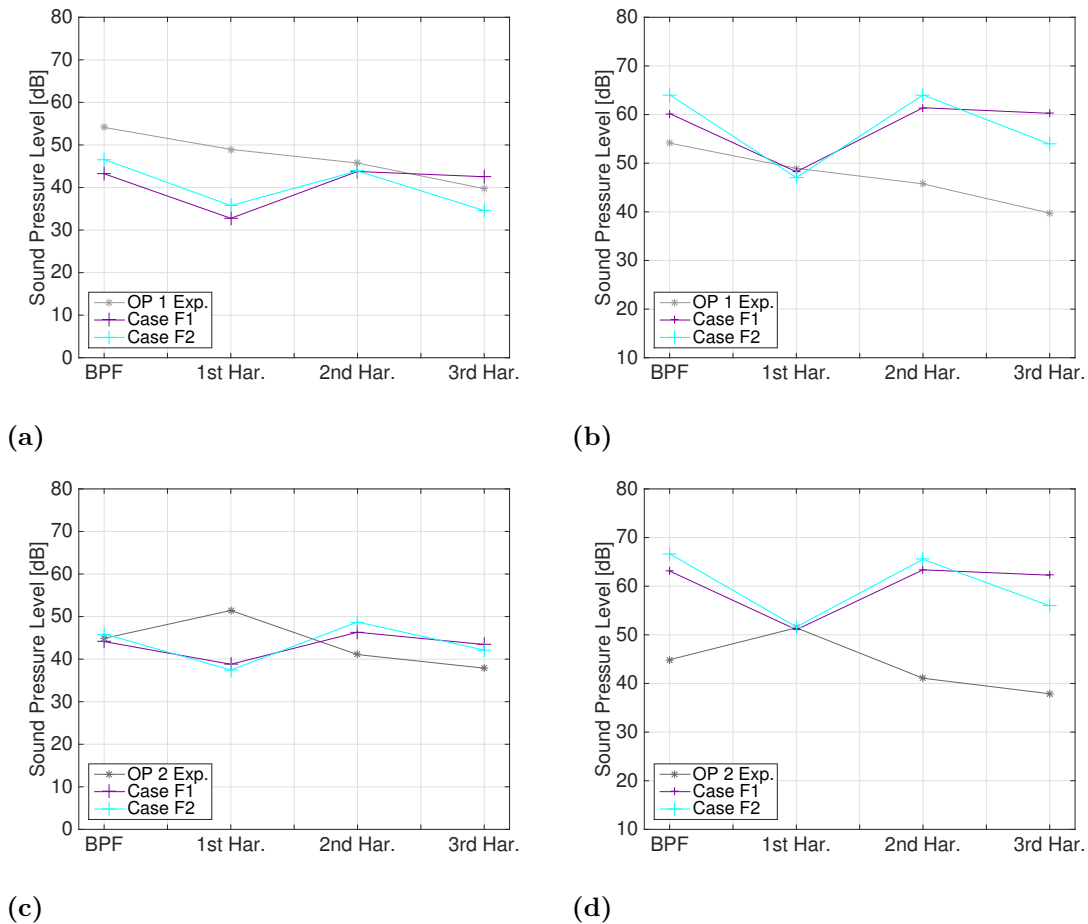


Figure 5.17: Sound pressure level at the blade passage frequency and the three higher harmonics for Case F1 and Case F2 at OP 1 (a-b) and OP 2 (c-d). In (a) and (c), only the centrifugal fan surfaces are used as source surfaces. In (b) and (d), centrifugal fan and impeller inlet are used as source surfaces.

Table 5.10: Sound pressure level at the blade passage frequency and the three higher harmonics for Case F at OP 2.

Source Surface		BPF	1 st Harmonic	2 nd Harmonic	3 rd Harmonic
Exp. OP 2		44.88	51.44	41.07	37.88
Case F1	Fan	44.13	38.80	46.32	43.43
Case F2	Fan	45.94	37.44	48.73	42.14
Case F1	Fan, Imp. Inlet	63.11	51.06	63.36	62.25
Case F2	Fan, Imp. Inlet	66.67	51.62	65.53	55.96

5.2.5 Pressure Discretization

In the following section, the effects of the pressure discretization are investigated. The PRESTO scheme is compared with the 2nd order CD scheme for the two turbulence models. For the realizable $k - \varepsilon$ model, (Case D1 and Case E1), the frequency spectra for OP 1 and OP 2 are shown in Figure 5.18, while the sound pressure levels at the fundamental frequencies for OP 1 and OP 2 are shown in Figure 5.19. For the $k - \omega$ SST model, (Case D2 and Case E2), the spectra is shown in Figure 5.20, while the sound pressure levels with respect to fundamental frequencies are shown in Figure 5.21. In the following section, the centrifugal fan and impeller inlet are used as source surfaces.

When the PRESTO scheme is used, the baseline is highly increased for both turbulence models. It is clearly seen by adding all the frequency components together which yields the *Overall Sound Pressure Level* (OASPL). The OASPL value for each case is listed in Table 5.11, where a significant increase is noted for the PRESTO scheme. The discrepancy is especially significant for the $k - \omega$ SST model, Case D2 and Case E2, where the OASPL difference is close to 15 [dB] for both observer points. For the realizable $k - \varepsilon$ model, Case D1 and E1, the discrepancy is smaller but still significant with a difference of approximate 8 [dB] and 7 [dB] for OP 1 and OP 2.

Table 5.11: Overall sound pressure levels for the two turbulence models discretized with either PRESTO (Case D) or CD (Case E). OP 1 is shown in (a) while OP 2 is shown in (b).

(a)

Case	OASPL [dB]
D1	69.94
E1	62.00
D2	73.68
E2	58.45

(b)

Case	OASPL [dB]
D1	72.83
E1	65.91
D2	76.51
E2	62.21

By observing the frequency spectra for the realizable $k - \varepsilon$ in Figure 5.18a - 5.18b a few things can be noted. With the PRESTO scheme, the sound pressure level at the blade passage frequency is greatly over predicted for both observer points, whereas it is only over predicted at OP 2 for the CD scheme. Case D1 does predict the tone slightly above the blade passage frequency which is not the case for Case E1. Observing the sound pressure levels at the fundamental frequencies in Figure 5.19a and OP 1, it can be seen that the overall trend of Case D1 shows a higher resemblance towards experimental data even though the blade passage frequency is highly over predicted. Case E1 only shows good agreement for the blade passage frequency and the second harmonic while the first and

third harmonic are severely under predicted. Considering the sound pressure levels at the fundamental frequencies at OP 2, Figure 5.19b, Case D1 shows a higher level of agreement towards the experimental data when compared to Case E1. The first and second harmonic are almost exactly predicted by Case D1, but as for OP 1, the blade passage frequency is highly over predicted, while the third harmonic is badly under predicted. Generally, the PRESTO scheme yields a higher sound pressure level for all the fundamental frequencies and shows a higher similarity with the experimental data, except for the blade passage frequency at OP 1 where the CD scheme is closer.

Observing the spectra and the sound pressure levels at the fundamental frequencies at OP 1 for the $k-\omega$ SST model in Figure 5.20a and Figure 5.21a, a similar behaviour as for the realizable $k-\varepsilon$ model is found. The PRESTO greatly over predicts the sound pressure level for the blade passage frequency and under predicts the first, second and third harmonic, but the trend is relatively accurate. As for the $k-\varepsilon$ model, the CD scheme is only close to the experimental data for the blade passage frequency and the second harmonic, but for the $k-\omega$ SST model it is almost spot on. Considering OP 2, Figure 5.20b and Figure 5.21b, Case D2 shows a higher correspondence towards the experimental data when compared to Case E2. For the first, second and third harmonic, Case D2 are very close, but with a severe over prediction for the blade passage frequency. The trend for Case E2 does not correspond to the experimental data, even though the second and third harmonic are relatively close.

Generally it can be noted that the PRESTO scheme gives a more broadband type sound, the spectrum contains multiple frequencies with equal magnitude which is not the case for the CD scheme. With the CD scheme more or less only the blade passage frequency and the higher harmonics are noticeable, i.e. more tonal type sound. The trends from PRESTO scheme for both the realizable $k-\varepsilon$ and $k-\omega$ SST model show a higher agreement to experimental data, with relatively accurate predictions of the first, second and third harmonic but with a over prediction for the blade passage frequency. The CD scheme shows good predictions for the blade passage frequency at OP 1, and good predictions for the second harmonic at both observer points.

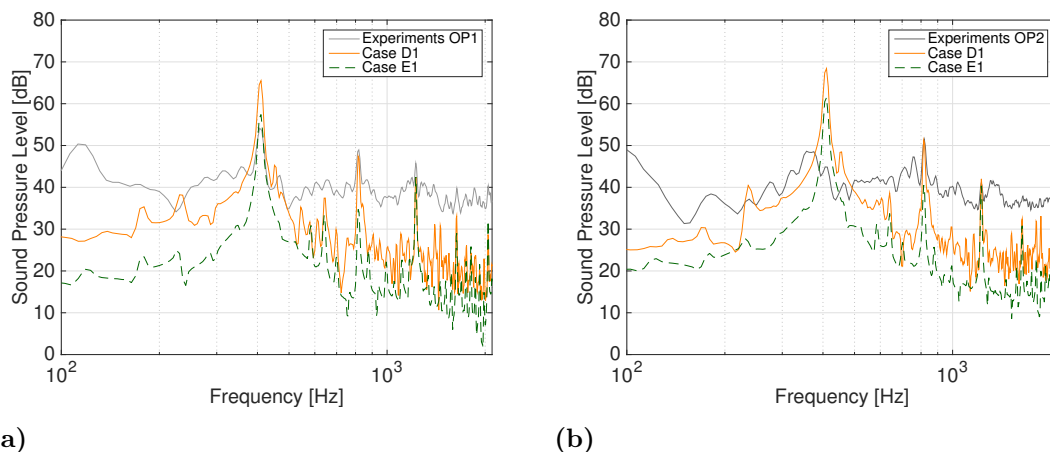


Figure 5.18: Sound pressure levels with respect to frequency for OP 1 (a) and OP 2 (b). Realizable $k-\varepsilon$ with pressure discretized with PRESTO (orange) and pressure discretized with 2^{nd} order CD scheme (green).

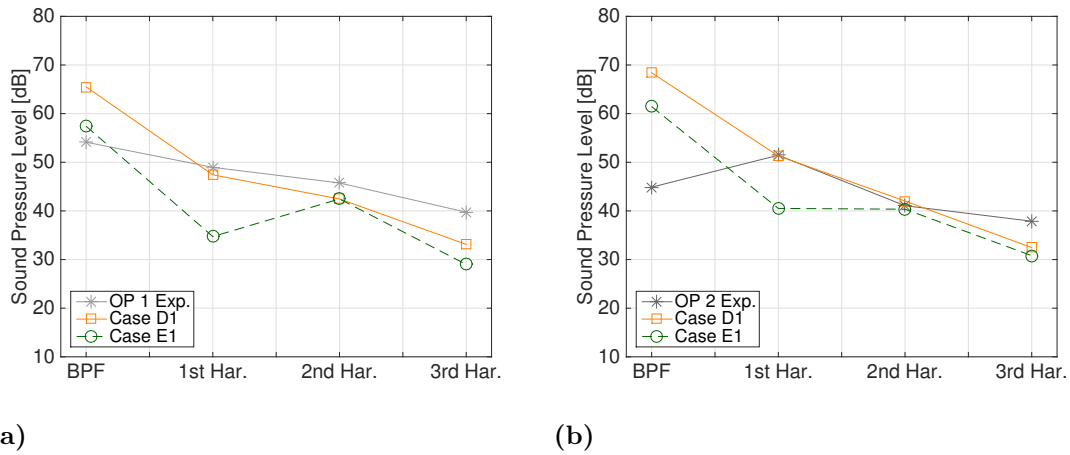


Figure 5.19: Sound pressure levels at the blade passage frequency and the higher harmonics at OP 1 (a) and OP 2 (b). Realizable $k - \varepsilon$ with pressure discretized with PRESTO (orange) and pressure discretized with 2^{nd} order CD scheme (green).

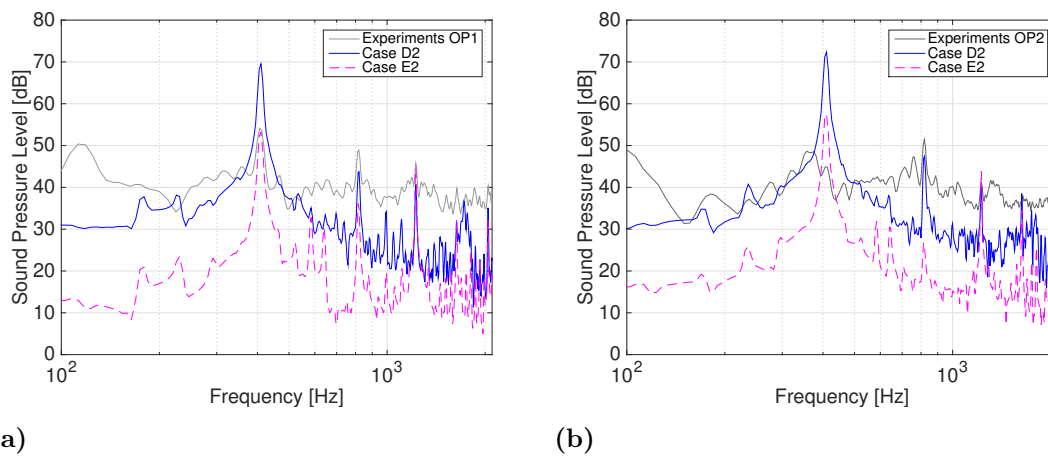


Figure 5.20: Sound pressure levels with respect to frequency for OP 1 (a) and OP 2 (b). $k - \omega$ SST with pressure discretized with PRESTO (blue) and pressure discretized with 2^{nd} order CD scheme (magenta).

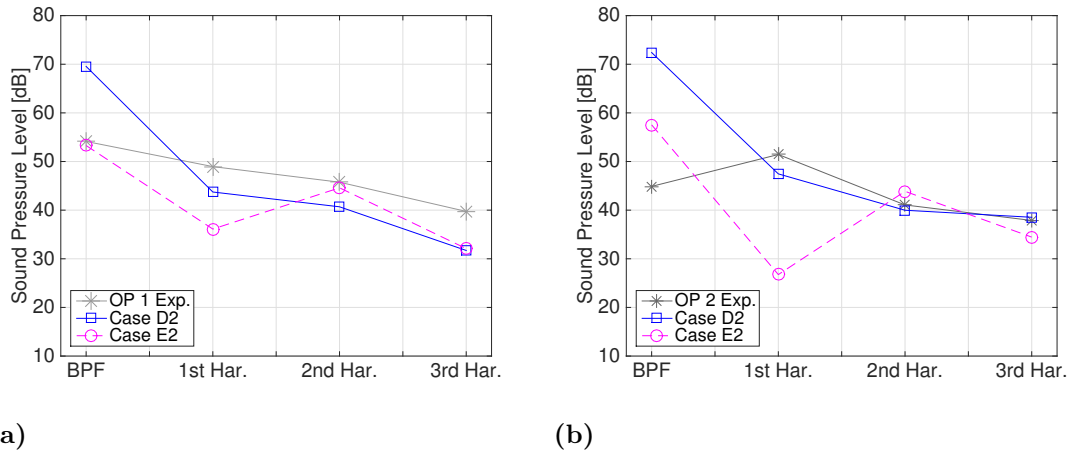


Figure 5.21: Sound pressure levels at the blade passage frequency and the higher harmonics at OP 1 (a) and OP 2 (b). $k - \omega$ SST with pressure discretized with PRESTO (blue) and pressure discretized with 2^{nd} order CD scheme (magenta).

5.2.6 Compressibility

In the following section, the effects of incompressible flow are investigated for the two turbulence models. For the realizable $k - \varepsilon$ model, (Case D1 and Case F1), the frequency spectra for OP 1 and OP 2 are shown in Figure 5.22, while the sound pressure levels at the fundamental frequencies for OP 1 and OP 2 are shown in Figure 5.23. For the $k - \omega$ SST model, (Case D2 and Case F2), the spectra are shown in Figure 5.24, while the sound pressure levels with respect to fundamental frequencies are shown in Figure 5.25. In the following section, the centrifugal fan and impeller inlet are used as source surfaces.

Observing the frequency spectra for the realizable $k - \varepsilon$ model, Figure 5.22a - 5.22b, it can be noted that by using an incompressible approach the frequencies above 1100 [Hz] start to increase. It can also be noted that the low frequency fluctuations seems to be magnified by using an incompressible flow assumption. For Case D1, there are two noticeable tones at roughly 160 [Hz] and 230 [Hz] which are greatly magnified in Case F1. Both cases over predicted the blade passage frequency, and both cases capture the first harmonic. At 1100 [Hz], Case F1 start to exhibit an increase in sound pressure levels resulting in a non accurate prediction of the higher harmonics. The trends can be seen in Figure 5.23a - 5.23b where the divergence of Case F1 is clearly visualised for the two observer points. The trends for Case D1 are more in line with the trend of the experimental data, especially for OP 1, albeit severe over prediction of the blade passage frequency and an increasing under prediction for the higher harmonics. From Figure 5.23a - 5.23b it can also be noted that the spectra for the incompressible case at OP 1 and OP 2 are very similar to each other.

Visualising the frequency spectra for the $k - \omega$ SST model Figure 5.24a - 5.24b, the same trends as for the realizable $k - \varepsilon$ model can be seen. Amplification of the low frequency tones and an increase at frequencies above 1100 [Hz]. The trends are more easily seen in Figure 5.25a - 5.25b, where it can be noted that the trend for incompressible case are far off the experimental trend, while the compressible case shows a higher resemblance. As for the realizable $k - \varepsilon$ mode, there are great similarities between the frequency spectra for OP 1 and OP 2 for the incompressible case.

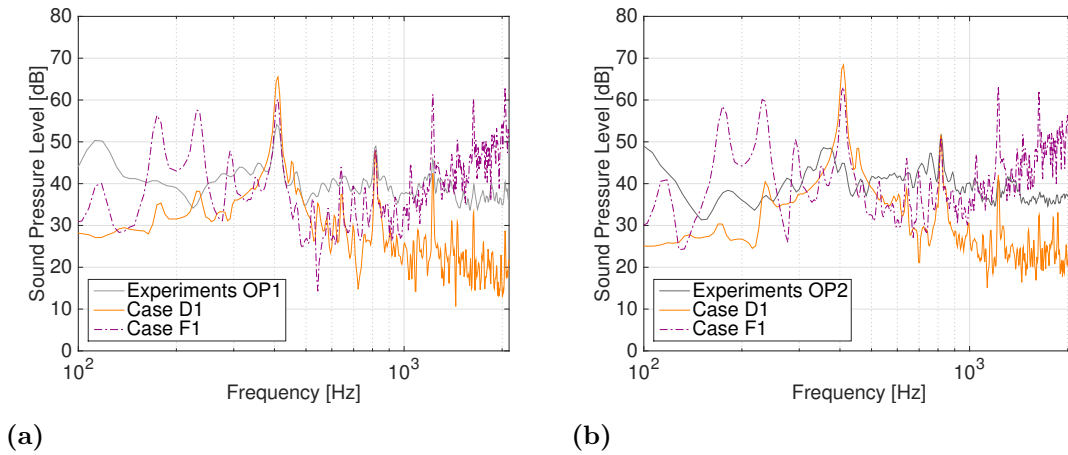


Figure 5.22: Sound pressure levels with respect to frequency for OP 1 (a) and OP 2 (b). Compressible Realizable $k - \varepsilon$ (orange) and incompressible (pink).

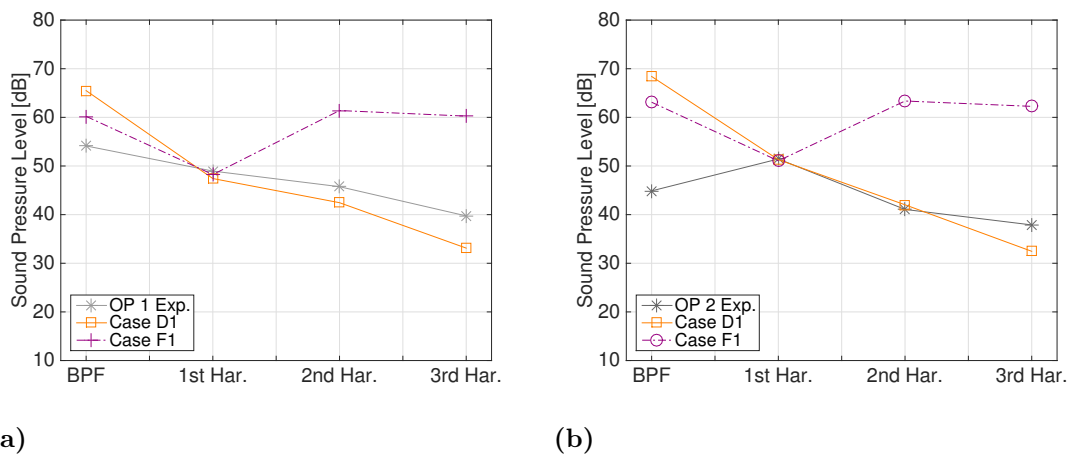
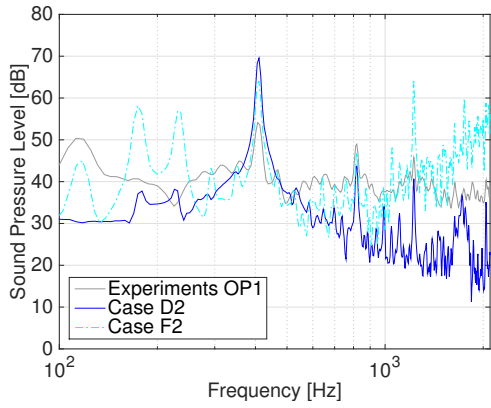
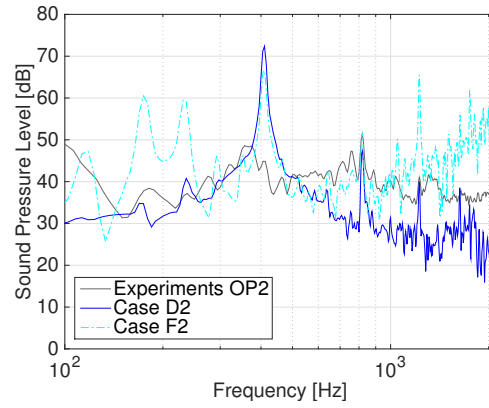


Figure 5.23: Sound pressure levels at the blade passage frequency and the higher harmonics at OP 1 (a) and OP 2 (b). Compressible Realizable $k - \varepsilon$ (orange) and incompressible (pink).

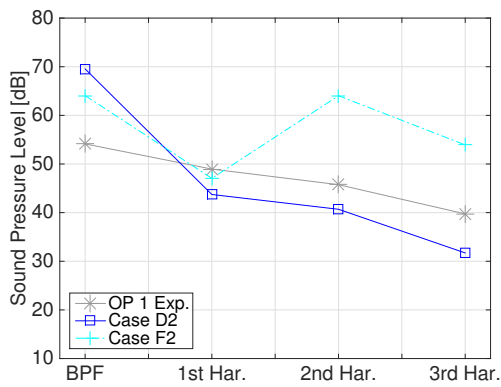


(a)

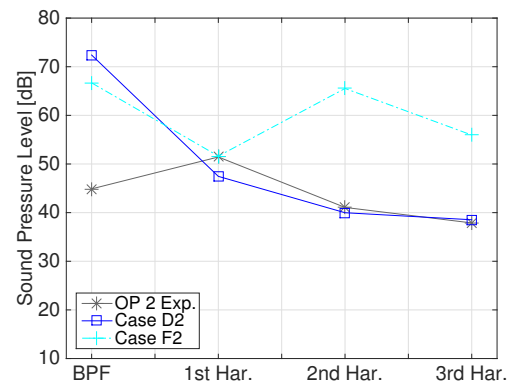


(b)

Figure 5.24: Sound pressure levels with respect to frequency for OP 1 (a) and OP 2 (b). Compressible $k - \omega$ SST (blue) and incompressible (magenta).



(a)



(b)

Figure 5.25: Sound pressure levels at the blade passage frequency and the higher harmonics at OP 1 (a) and OP 2 (b). Compressible $k - \omega$ SST (blue) and incompressible (magenta).

6

Discussion

The following chapter contains three distinct parts, the first part involves issues encountered during the methodology. After which the results are discussed and analysed with the aim to try and give possible explanations for the physical observations. Finally, different sources of error are presented and what they imply.

6.1 Methodology Related

The following section contains information regarding issues that occurred while setting up the different models. The problems are discussed and possible mitigations are suggested. These problems are related to implementation of the sector domain in FLUENT, and regarding the sampling of pressure for the FW-H acoustic analogy on parallel processors.

6.1.1 Sector Model

To set up the physical problem with sliding domains was relatively straight forward for the full domain models. No divergences or unphysical behaviour occurred, which can not be said for the sector model. The first several tries suddenly diverged at a specific time step, leaving now clue to what was causing the problems. Later it was found that the periodic boundaries, both stationary and rotating, had to be conformal and special attention was given to obtain this in ANSA. This solved the initial divergence issue but new issues regarding the coupling between the sliding interfaces and the periodic boundaries arose. When the flow was treated as compressible, for certain time steps, the temperature would drastically increase for a few cells at the sliding interface between the rotating and stationary domain causing the pressure to drastically increase through the ideal gas law, Equation (2.5), yielding erroneous results in the entire computational domain. Since the effect was only appearing for a few cells it was thought to be related to the quality of the mesh and several new meshes with different element types and sizes were generated but no improvement was found. It should be noted that the quality of the original mesh in terms of skewness and angles were far above the criteria recommended by FLUENT, and the same mesh density had already been used for a full domain model with no issues regarding the temperature. The mentioned behaviour occurred for both turbulence models and both pressure discretizations. By limiting the temperature to physical temperatures actually present in that location, the issue was mitigated and no erroneous results were obtained regarding any flow variables. This is not a completely satisfactory method since it is very case dependent and requires a trial and error approach. When the flow was treated as incompressible there was no temperature but then the pressure at the same location started to diverge. In FLUENT, the pressure can't be limited in the same way as

temperature and a different solution procedure had to be used. This complication was mitigated by reducing the under relaxation factors for momentum and pressure, leading to a higher amount of inner iterations within each time step to reach the same convergence criteria. It should be noted that this only occurred for the realizable $k - \varepsilon$ model and not for the $k - \omega$ SST model and the reason for this has not been found. There seems to be problems related to the sliding interfaces in conjunction with the periodic boundaries. A possible mitigation solution could be to use conformal interfaces, i.e. in every time step there is an exact match in all dimensions between the rotating and stationary interfaces. Due to non-planar interface surfaces and the complexity of creating such a conformal interface this was not investigated any further. The issue could also be related to the implementation of the sliding interfaces together with the periodic boundaries in FLUENT, and softwares specifically designed for rotating machinery such as CFX might be more suited.

6.1.2 Pressure Sampling on Parallel Processors

An issue that arose during the study was that the pressure sampling for the FW-H equation had to be done in one simulation when the computational domain is parallelised for multiple processors. Every time a simulation is restarted, the mesh is parallelised in a different way. This difference results in a miss match in the FW-H sampling file that expresses it self as a pressure value several magnitudes larger than the rest of the signal. After a few time steps this effect dies out and the pressure signal returns to its normal state, but for a slightly different mean value. If this miss match occurs at the beginning or the end of the pressure signal, the corrupted part is easily removed, but if it occurs in the middle, the entire signal is ruined. Since the FW-H sampling files must be read sequentially, the entire signal must be created in one simulation. This issue is the main reason for the low frequency resolution of the numerical simulation. A mitigation for this could potentially be to force the same parallelisation in the setup, so that the same parallelisation is always used.

6.2 Results Related

The current section contains a discussion about possible reasons to why specific results are obtained. The section is divided into the same main subsections as the Results chapter with an Aerodynamic and Acoustic subsections.

6.2.1 Aerodynamic

The PQ-curves were all generated from steady state MRF simulations, this is of course a simplification in comparison with the transient sliding mesh simulations. The MRF model assumes that the unsteady interactions between the stationary and rotating domains are weak, and if this is not the case the results can be erroneous as mentioned in Section 2.4.3.1. The sliding mesh technique was only used for the flow rate at which the acoustic prediction was performed. At that specific flow rate, the pressure difference was increased by only 1 – 2 [Pa] indicating good agreement between the steady MRF model and the transient sliding mesh model. But for flow scenarios close to the maximum and minimum flow limit, there might be highly unsteady flow phenomenons present, where a transient

simulation together with the sliding mesh technique might be necessary. At flow rates close to stall, i.e. minimum flow rate, there were high variations for flow variables between iterations which indicates that a transient simulation might be needed.

The $k - \omega$ SST model shows a higher correspondence towards the experimental data for almost all flow rates except the lowest close to $Q = 0.225 [m^3/s]$. But as mentioned in the previous paragraph, a transient simulation would probably alter the results for both turbulence models. When the centrifugal fan rotates, there is an adverse pressure gradient on the suction side, see Figure 5.3, of the blade which causes separation at the trailing edge. The $k - \omega$ SST model is supposed to be superior to the realizable $k - \varepsilon$ model at handling adverse pressure gradients and separation which is probably one of the main reasons for the more accurate results.

The two models are also improved by using the PRESTO scheme as compared to the 2nd CD scheme. According to FLUENT, the PRESTO scheme gives more accurate results in cases with steep pressure gradients, which is usually the case in rotating flows.

It comes as no surprise that the difference between compressible and incompressible flow is minor regarding the pressure increase over the fan. The highest mach number is approximately 0.14 and is far below the criterion of 0.3 at from which compressibility effects must be taken into consideration as mentioned in Section 2.2.2. Nonetheless, including compressibility effects shows a higher resemblance towards the experimental data, indicating that the compressible effects aren't completely negligible even though the mach number is as low as 0.14.

6.2.1.1 Time Averaged Pressure

Observing the RMSE pressure field on the centrifugal fan and impeller inlet surfaces in Figure 5.4, a difference between the two full domain cases can be seen. Between Case A and Case B, the only difference in setup is the mesh resolution within the gap between the impeller inlet and the shroud. It is likely that this change is one of the reason for the differences. When there is only two nodes within the gap, the flow could potentially be obstructed in certain time steps depending on the interpolation. This obstruction could lead to a slightly different flow field that effects the RMSE pressure field at the blades and inside of the shroud. Another potential cause could be due to development of the flow. Case A have marched further in time and the flow field may have developed further when compared to Case B. The latter explanation could also be one of the reasons to why there is such a difference between the sector model and the two full domain models. Since the sector domain is only one seventh of the full domain size, the flow could potentially develop up to seven times faster. Comparing Case A, Figure 5.4a to Case D1, Figure 5.4e, it is noted that there are arcs starting to form on the impeller inlet for Case A, and that these have already been developed for Case D1. This would support the argument that all fluctuations haven't reached a periodic state and that further time marching is necessary. The criterion for convergence was that the pressure increase over the centrifugal fan had reached a periodic state. This basically means that the large scale motions have settled, but there could still exist small scale fluctuations that haven't reached a converged state which would effect the RMSE pressure field. Since the time averaged pressure field, Figure 5.3, is so alike between all of the cases it is safe to say that the large scale fluctuations have reached a converged state.

It can't be ruled out that the distinct difference between Case A and Case D1 could be an effect of the periodic boundaries. As previously mentioned, the mean pressure field shows good agreement between the cases and the pressure field is also symmetric, indicating that periodic boundaries don't effect the mean flow to that extent. The similarity found for the time averaged pressure is not found for the RMSE pressure field, and might indicate that the periodic boundaries impose to harsh constraints on the fluctuating pressure field and potentially causes the difference seen for RMSE values for pressure.

6.2.2 Acoustic

The upcoming section follows the same structure as the acoustic result section. Comparing the different numerical grids, turbulence models, discretization scheme for pressure and treating the flow as incompressible.

6.2.2.1 Full Domain Models and Sector Model

The full domain models produce substantially lower sound pressure levels compared to sector model throughout the entire frequency spectra. Observing the pressure fluctuations in the different models, it can be noted visually that the RMSE pressure field is higher in the sector model compared to the full domain models which of course influences the propagated sound. But why there is a higher degree of pressure fluctuations in the sector model has not been found. The grid density in the sector model is in between the two full domain models and the difference in pressure fluctuations must be due to something else. Two possible causes were discussed in Section 6.2.1.1.

Another reason for the over prediction for the sector model could be related to how the source surfaces are reconstructed through the periodic boundaries for the acoustic propagation. If the source surfaces are reconstructed without taking the propagation into consideration, source surfaces will be completely in phase. In a study regarding a five bladed axial fan [50], a sector model and a full domain model is compared, where it was found that the sector model gives similar frequencies but the baseline of the spectrum is raised by roughly 7 [dB] in comparison with the full domain model. In the mentioned study, the sound sources for the five bladed model were actually incoherent, whereas the sound sources for sector model became coherent through the reconstruction which was thought to be the main reason for the higher prediction. The same argument can be applied to the current study, even though a study regarding the coherence of the sound sources haven't been investigated. If the increase is scaled with the number of blades, a seven bladed configuration would result in a prediction 9.8 [dB]¹ over the full domain models. Figure 6.1 compares the two full domain models, Case A and Case B, with Case D1 with 9.8 [dB] subtracted. It is clearly seen that by reducing the sound pressure level with the mentioned amount the correspondence between the cases is striking, except for the higher harmonics which aren't present in the full domain models.

Observing all the frequency spectra, it is clear that choosing the right surfaces as sound sources are crucial when calculating the sound pressure levels at the observer points, especially for the full domain models. Observing the pressure fluctuations in Figure 5.4, it is clearly seen that the pressure varies greatly at the impeller inlet which supports the argument that it should be included when comparing to experimental data. One should

¹ $\frac{7}{5} \frac{[dB]}{[Blades]} \cdot 7 [Blades] = 9.8 [dB]$

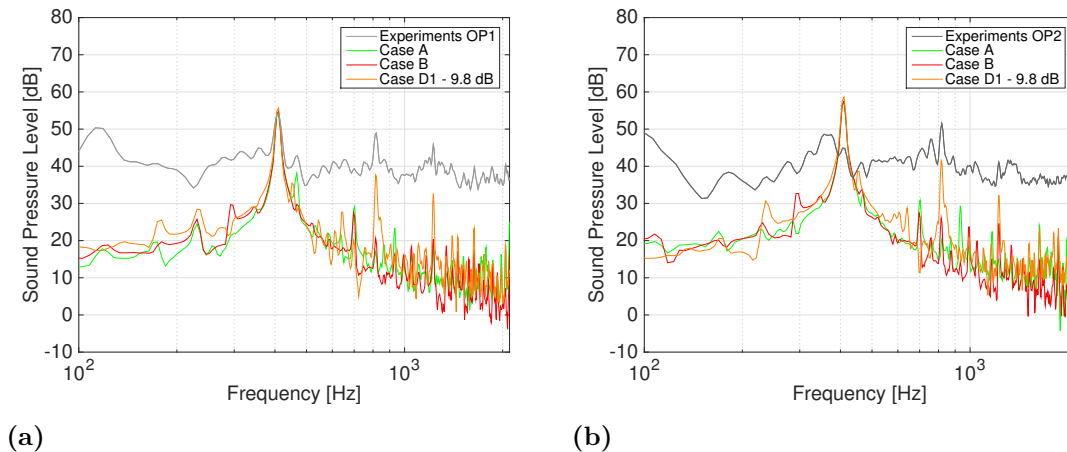


Figure 6.1: Frequency spectrum for the two full domain cases and the sector model, with 9.8 [dB] subtracted from the sector model

though be aware of the free field condition. The wave equation of FW-H is solved by the use of Green's free space function, i.e. that there is no obstruction between the sound sources and the observer points. This assumption is not completely fulfilled for any of the two observer points. The centrifugal fan is obstructing the free field for the impeller inlet for OP 1 and vice versa for OP 2.

When observing the experimental sound pressure levels at OP 2, Figure 5.5b, it can be seen that the sound pressure levels at the blade passage frequency is much lower than for OP 1, Figure 5.5a. The numerical estimation for the blade passage frequency at OP 1 is also more accurate in comparison with the estimation for OP 2. The two observer points are more or less the same distance from the sound sources, and since free field propagation is assumed, the difference in predicted sound pressure level at the two observer points is solely due to directivity of sound. This is not enough to explain the over prediction of the blade passage frequency at OP 2. The main reason for the over prediction is believed to be related to reflections and scattering effects of parts not included in the numerical model, and the inlet side. In the experimental measurements, there are several structural components present that are not included in the numerical estimation e.g. motor. The inlet side is also more narrow in comparison to the outlet side, and duct effects might therefore be more pronounced for OP 2. If this is the case, it is a phenomenon that the current methodology wont be able to capture due to the free field radiation, and this would also explain the over prediction at OP 2.

The sector models seem to be able to capture both the blade passage frequency as well as the higher harmonics, whereas the full domain models only capture the blade passage frequency. The reason for this have not been fully understood, but a possible explanation is that it is related to the development of the flow. The blade passage frequency is highly dependent on the hydrodynamic pressure whereas the higher harmonics are more dependent on smaller fluctuations related to the passing of each blade. It could be the case that the higher harmonics will emerge if the simulation of the full domain models are run for a longer time. If this assumption is found to be true, the benefits for using a sector model are huge in comparison with full domain models.

For OP 2, Figure 5.5b, there is a significant tone just below the blade passage frequency. But this tone is not one single tone as can be seen in Figure 4.9b, but due to the reduced frequency resolution they merge into one peak. None of the numerical simulations are able to capture these tones, which suggests that they appear due to a phenomenon not captured by the numerical models. Observing the entire pressure signal for OP 2 in Figure 4.9b, it can be seen that it is characterised by broadband sound, and this is explained by the measurements being made in a normal room and not in an anechoic room as OP 1. The mentioned tones could therefore be artifacts from the measurements and would therefore not be captured through the numerical model.

6.2.2.2 Turbulence Models

The two turbulence models generate very similar results in an aeroacoustic perspective. They capture the same fundamental frequencies and the sound pressure levels at the mentioned frequencies are within approximately 4 [dB] of each other. The similarities can possibly be explained by the similarities of the turbulence models. Both are two equation eddy viscosity models based on the Boussinesq assumption with turbulent kinetic energy as one of the turbulent variables. By using less alike turbulence models, e.g. based on more or less equations, or turbulence models not based on the Boussinesq assumption at all such as Reynolds Stress Models, the difference might be more pronounced. By observing the pressure increase over the centrifugal fan for the flow rate at which the acoustic prediction was performed in Figure 5.2. It can be seen that the difference between the turbulence models are very slight, at most a couple of percentage depending on the pressure discretization and flow assumption. Since the two models are alike in an aerodynamic perspective and in a model perspective, it seems reasonable that they are alike in an acoustic perspective as well. The pressure discretization and incompressible flow assumption affects the propagated sound to a higher extent than the turbulence models.

6.2.2.3 Pressure Discretization

The two pressure discretization yields very different results compared to each other for both turbulence models. Independently of the surfaces used as source sources, the PRESTO scheme captures the sound pressure level trend with respect to fundamental frequencies with more accuracy when compared to the CD scheme for both observer points, see Figure 5.18 and Figure 5.20. From the mentioned figures, it can also be seen that the PRESTO scheme is able to capture more broadband sound, which indicates that the scheme is able to resolve pressure fluctuations at a higher degree. No information about how the PRESTO scheme is implemented or it's general solution procedure have been found and the reason for the higher level of broadband sound remains unknown. Presumably, it uses more nodes in the interpolation allowing for a higher degree of freedom. Since pressure fluctuations are resolved at a higher degree for the PRESTO scheme, other important tones can be captured as well. Observing Figure 5.18a, it can be seen that by using the PRESTO scheme the tone slightly above the blade passage frequency is captured with good accuracy while it is not captured for the CD scheme.

The PRESTO scheme is recommended by FLUENT for flows with steep pressure gradients such as rotating flows, but also for using together with the acoustic analogy of FW-H and utilises a staggered grid for interpolation of the cell face values. By doing so, the requirements for memory increases due to the extra nodes in the staggered grid. During

the numerical study it was also found that the PRESTO scheme also has a lower convergence rate, requiring 30 – 50 % more iterations within each time step when compared to the CD scheme.

6.2.2.4 Compressibility

By using an incompressible flow simulation to feed the acoustic analogy there are a few notable effects on the frequency spectra, Figure 5.22 - 5.24. For both turbulence models, firstly, the low frequency tones (below 350 [Hz]) seem to be magnified, and there are also new tones present. Secondly, the magnitude of the blade passage frequency is lower for an incompressible flow approach. Thirdly, after approximately 1100 [Hz] there is a sudden increase in sound pressure levels that contaminates the entire spectrum. The latter behaviour is not seen for any of the similar studies, [36, 45], where an incompressible approach was adopted. As mentioned in the first paragraph in Section 4.3.1, the FW-H equation is solved with the Green's free space function, which requires a compressible flow approach if the sound sources are non compact. In the mentioned studies the centrifugal fans are small with a diameter of 70 and 80 [mm] each, and the sound source does thereby satisfy the compactness criterion for the frequency range in question. In this study, when the impeller inlet is used as sound source, the diameter of the sound source equals the length of an approximately 650 [Hz] wave. Suggesting that the compactness is violated at 650 [Hz] which does not correspond to what is seen in the frequency spectra. However, since the simulation is performed on a sector model where only the radius is present, the radius of the domain equals the length of an 1300 [Hz] wave which almost coincides with the frequency where the unphysical increase in sound pressure levels occur. Indicating that it is the violation of the compactness criterion of the sound sources that causes the unphysical increase in sound pressure levels. With this line of reasoning, if an incompressible approach would have been used for the full domain models, the unphysical increase in sound pressure level would have occurred for 650 [Hz] instead, rendering the incompressible approach almost unusable for the current centrifugal fan. No full domain model have been simulated with incompressible flow and mentioned reason is only a hypothesis that needs to be verified or refused.

The increased magnitude at the blade passage frequency for the compressible case can possibly be explained by the higher level of pressure information within a compressible flow simulation. Using a compressible approach, both the hydrodynamic pressure and the acoustic pressure can be obtained, whereas only the hydrodynamic pressure can be obtained by the incompressible approach.

6.3 Sources Of Error

- Due to a miss communication, the numerical study was performed at a lower volume flow rate compared to the experimental data. The volume flow rate used for the numerical simulations was 0.408 [m^3/s], while the experimental sound characteristics were measured for a volume flow rate of 0.425 [m^3/s]. With an error of 4 %, the change in sound pressure level would most likely be negligible since decibel is a logarithmic scale. However, it cannot be ruled out, that an increase of volume flow rate by 4 % could alter the flow structures which in turn could influence the propagated sound.

- In reference [23], it is mentioned that the FW-H equation is solved with the assumption that there is no acoustic interference between the acoustic sources. In reality there is most likely acoustic interference between the centrifugal fan and the impeller inlet which is not captured.
- In the experimental data, the sound will be affected by the outlet side and inlet side. But when the FW-H equation is solved with the Green's free space function, the sound is propagated as if free field conditions apply. This means that scattering and reflections of the sound towards the observer points will not be captured by the numerical model.
- There are structural components present in the experimental domain during measurements that are not included in the numerical domain.

7

Conclusion

The main objective of this thesis was to investigate and propose a methodology regarding numerical prediction of the flow induced sound generated by a centrifugal fan. The numerical prediction is supposed to replace experimental measurements at earlier development stages to quickly reach a conclusion regarding which of two fan models that shows the most promising results. In order to save computational resources and time, turbulence was only modelled through URANS.

A hybrid aeroacoustical approach was adopted, in which only the near field pressure field is solved for and used in conjunction with an acoustic analogy for propagation of the sound to the far field. The acoustic analogy of Ffowcs William & Hawkings has been used together with the integral formulation of Brentner and Farassat. In order to reach the above mentioned goal, different numerical grids have been investigated, full domain models have been compared to sector models, different turbulence models have been investigated, various pressure discretization have been tested, aeroacoustical effect of different sound sources, and finally, the assumption of compressible or incompressible flow has been explored. The concluding remarks are summarised below:

- When using a full domain model it is evident that the pressure fluctuations on the surfaces of the impeller inlet and centrifugal fan are of importance to the propagated sound, and the mentioned surfaces should be used as source sources in the FW-H equation. When using a sector model, that choice isn't as evident but it is still clear.
- Using a full domain model gives an accurate prediction of the sound pressure level at the blade passage frequency for the downstream observer point, with a prediction within 0.7 [dB] to the experimental measurements. But the higher harmonics have not been found, and one of the reason for this is probably that the flow is not fully developed. By using a sector model, sound pressure level at the blade passage frequency is over predicted by 10 [dB], but the higher harmonics are captured with higher accuracy. The over prediction of the sector model is thought to be related to the reconstruction of the acoustic sources through the periodic boundaries. The reconstruction gives seven in-phase sources which in turn cause the over prediction. By subtracting 10 [dB], the frequency spectra of the sector model coincide with those of the full domain models, except for the tones of the higher harmonics that are present in the sector models.
- The choice of turbulence model has only a slight effect of the propagated sound pressure levels, and both the realizable $k - \varepsilon$ and $k - \omega$ SST turbulence model yield a satisfactory result. The aeroacoustical effect of changing turbulence model is minor in comparison to switching discretization scheme for pressure or switching

to incompressible flow. The realizable $k - \varepsilon$ model shows the best agreement to the experimental data for the downstream observer point whereas $k - \omega$ SST shows the best agreement for the upstream observer point.

- The sound pressure level trend at the fundamental frequencies are captured with more accuracy for the PRESTO scheme, but yields a major over prediction at the blade passage frequency. The central difference scheme is able to accurately predict the amplitude of the blade passage but fails to capture the trend of the higher harmonics.
- The predicted sound pressure levels at the blade passage frequency and the first harmonic with an incompressible flow approach are very similar to the predicted sound pressure levels using a compressible flow approach. But, when using an incompressible flow approach, the sound pressure levels drastically increase after 1100 [Hz] and the higher harmonics are thereby lost. The sudden increase is thought to be related to the compactness of the source, and that the FW-H equation requires compressible flow for non-compact sources.

For a fast comparison between the sound pressure level trends between two fan models, the sector domain model is sufficient. If the absolute sound pressure level at the blade passage frequency is required, the full domain model is recommended. Turbulence can be modelled with both the realizable $k - \varepsilon$ and the $k - \omega$ SST model, but pressure should be discretized with the PRESTO scheme. The assumption of incompressible flow can be made if only the blade passage frequency is required, if higher frequencies are required the flow must be treated as compressible.

8

Future Work

A lot of work has been put into this study but there are still many things to investigate before a complete methodology regarding aeroacoustics for centrifugal fans can be obtained. The main questions are stated below:

- Why is there such a difference between the full domain model and the sector model? Firstly, why the over prediction? A few reasons for the over prediction have been discussed, but a further investigation is needed. Secondly, why does the sector model predict the higher harmonics while the full domain model does not? This was only briefly discussed and a more thorough investigation is needed.
- In this study, only two different meshes were tested, and the only difference was the number of nodes within the gap between the bottom of impeller inlet and top of the shroud. A thorough mesh study is needed, where the effects of different mesh sizes on the propagated sound are investigated.
- Investigation of the current solution procedure for different fans. The methodology proposed must be tested for a variety of fan models preferably with different sizes, increased or decreased number of fan blades, multiple flow rates etc.
- Investigate non-reflective boundary conditions. In this study, the outlet and inlet boundaries were not treated as non-reflective as the flow did not seem to fluctuate close to those boundaries. But there might have been pressure waves that bounced back into the domain and contaminated the "true" sound.
- Increasing the order of accuracy of the discretization schemes. In this study only second order schemes were used for discretization. By increasing the discretization scheme order the numerical diffusion could possibly be reduced. With a reduction in numerical diffusion, the pressure waves could possibly be less distorted which would alter the pressure fluctuations at the wall surfaces in the domain and in the end the propagated sound. Seeing that changing discretization scheme for pressure severely changed the results, the effect of changing discretization scheme for other quantities must be studied.
- In this study only URANS turbulence models have been used. It would be very interesting to carry out simulations with eddy resolving capabilities and investigate what effect this would have on the acoustic predictions. To still try to keep the simulation costs down a hybrid-LES approach such as DES could be used, but also second generation URANS models such as PANS or SAS could be used.

- It would be interesting to use an actual acoustic software for the far field propagation to validate the propagation tool in FLUENT for the full domain model. For the sector model, it seemed that one of the reasons for the over prediction was due to the reconstruction of the sector domain for the FW-H equation. With another acoustic software this effect might be mitigated.
- In the acoustic analogy by FW-H, free field radiation is assumed, and scattering and reflections are not captured. By coupling the near field pressure field with a computational transport method, these effects could be captured and a more realistic estimation could be obtained.
- Only the pressure increase over the centrifugal fan was used to validate the aerodynamics. This is a rather blunt measure, and more experimental data could increase the accuracy of the numerical model and in the end the acoustics. For example, pressure could be measured on the centrifugal fan or surrounding wall to ensure that the fluctuations in the near field are reasonable. Another option is to measure the velocity at different locations to create experimental velocity profiles to which the numerical simulations can be compared to.

Bibliography

- [1] W. T. W. Cory. *Fans & ventilation: a practical guide*. Elsevier in association with Roles & Assoc, Amsterdam;Boston;, 2005;2010;2012;.
- [2] W. Neise. Noise reduction in centrifugal fans: A literature survey. *Journal of Sound and Vibration*, 45(3):375–403, 1976.
- [3] P. Sagaut, T. Hüttl, and C. A. Wagner. *Large-eddy simulation for acoustics*, volume 20. Cambridge University Press, New York, 2007;2006;.
- [4] M. Wang, J. B. Freund, and S. K. Lele. Computational prediction of flow-generated sound. *Annual Review of Fluid Mechanics*, 38(1):483–512, 2006.
- [5] M. Younsi, F. Bakir, S. Kouidri, and R. Rey. Influence of impeller geometry on the unsteady flow in a centrifugal fan: Numerical and experimental analyses. *International Journal of Rotating Machinery*, 2007:1–10, 2007;2008;.
- [6] S. Li, W. Wang, Q. Liu, and X. Li. Validation of numerical prediction method of bpf noise for industrial centrifugal fans. *HVAC&R Research*, 20(4):435–443, 2014.
- [7] A. Zamiri, H. Joon OH, and Y. J. Moon. Spectral characterizations of centrifugal fan noise via urans-based noise prediction method. *Fan conference Fan2015*, 2015.
- [8] J. N. Reddy. *An introduction to continuum mechanics: with applications*. Cambridge University Press, Cambridge, 2008.
- [9] H. K. Versteeg and W. Malalasekera. *An introduction to computational fluid dynamics: the finite volume method*. Pearson Prentice Hall, Harlow, 2. edition, 2007.
- [10] F. M. White. *Fluid mechanics*. McGraw-Hill, Singapore, 7th in si units. edition, 2011.
- [11] S. L. Dixon and C. A. Hall. *Fluid mechanics and thermodynamics of turbomachinery*. Butterworth-Heinemann/Elsevier, Amsterdam, 7. edition, 2014;2013;.
- [12] L. Davidson. Fluid mechanics, turbulent flow and turbulence modeling, lecture notes in msc courses. Technical report, Chalmers University of Technology, Göteborg, 2010.
- [13] O. Reynolds. On the dynamical theory of incompressible viscous fluids and the determination of the criterion. *Philosophical Transactions of the Royal Society of London. A*, 186:123–164, 1895.
- [14] D. C. Wilcox. *Turbulence modeling for CFD*. DCW Industries, La Cãnada, Calif, 2. edition, 1998.
- [15] J. Blazek. *Computational fluid dynamics: principles and applications*. Elsevier, Boston, Massachusetts, 3 edition, 2015;2005;.
- [16] A. Dewan. *Tackling turbulent flows in engineering*. Springer, New York;Heidelberg;, 1 edition, 2011;2010;.

- [17] W. P. Jones and B. E. Launder. The prediction of laminarization with a two-equation model of turbulence. *International Journal of Heat and Mass Transfer*, 15(2):301–314, 1972.
- [18] B. E. Launder and D. B. Spalding. The numerical computation of turbulent flows. *Computer Methods in Applied Mechanics and Engineering*, 3(2):269–289, 1974.
- [19] T. H. Shih, W. W. Liou, A. Shabbir, Z. Yang, and J. Zhu. A new k-epsilon eddy viscosity model for high reynolds number turbulent flows. *Computers and Fluids*, 24(3):227–238, 1995.
- [20] D. C. Wilcox. Reassessment of the scale-determining equation for advanced turbulence models. *AIAA Journal*, 26(11):1299–1310, 1988.
- [21] F. R. Menter. Two-equation eddy-viscosity turbulence models for engineering applications. *AIAA Journal*, 32(8):1598–1605, 1994.
- [22] ANSYS Inc. *Fluent Theory Guide*. ANSYS Inc, Southpointe, 275 Technology Drive, Canonsburg PA 15317, 15.0 edition, 2013.
- [23] ANSYS Inc. *Fluent User Guide*. ANSYS Inc, Southpointe, 275 Technology Drive, Canonsburg PA 15317, 15.0 edition, 2013.
- [24] D. G. Crighton. Basic principles of aerodynamic noise generation. *Progress in Aerospace Sciences*, 16(1):31–96, 1975.
- [25] T. D. Rossing. *Springer Handbook of Acoustics*. Springer New York, New York, NY, 2nd 2014;2; edition, 2014;2015;.
- [26] M. E. Goldstein. *Aeroacoustics*. McGraw-Hill, New York, 1976.
- [27] M. Åbom. *An introduction to flow acoustics*. Åbom Mats, Stockholm, 2006.
- [28] F. Jacobsen and P. M. Juhl. *Fundamentals of general linear acoustics*. John Wiley & Sons Inc, Chichester, West Sussex, United Kingdom, 1 edition, 2013.
- [29] H. Bodén, U. Carlsson, R. Glav, H. P. Wallin, and M. Åbom. *Ljud och vibrationer*. Marcus Wallenberg Laboratoriet för Ljud och Vibrationsforskning, Inst. för Farkostteknik, KTH, 2001.
- [30] M. J. Lighthill. On sound generated aerodynamically. i. general theory. *Proceedings of the Royal Society of London. Series A, Mathematical and Physical Sciences*, 211(1107):564–587, 1952.
- [31] T. K. Bose. *Aerodynamic noise: an introduction for physicists and engineers*, volume 7. Springer, New York, 1. Aufl.;1; edition, 2013;2012;.
- [32] N. Curle. The influence of solid boundaries upon aerodynamic sound. *Proceedings of the Royal Society of London. Series A, Mathematical and Physical Sciences*, 231(1187):505–514, 1955.
- [33] J. E. Ffowcs Williams and D. L. Hawkings. Sound generation by turbulence and surfaces in arbitrary motion. *Philosophical Transactions of the Royal Society of London. Series A, Mathematical and Physical Sciences*, 264(1151):321–342, 1969.
- [34] G. B. Folland. *Fourier analysis and its applications*, volume 4. American Mathematical Society, Providence, R.I, 2009.
- [35] R. J. Marks. *Introduction to Shannon Sampling and Interpolation Theory*. Springer New York, New York, NY, 1991.

-
- [36] M. Younsi, F. Bakir, S. Kouidri, and R. Rey. Numerical and experimental study of unsteady flow in a centrifugal fan. *Proceedings of the Institution of Mechanical Engineers, Part A: Journal of Power and Energy*, 221(7):1025–1036, 2007.
- [37] Y. Mao, D. Qi, X. Liu, and H. Tang. Numerical prediction of aerodynamic tonal noise radiated from a centrifugal fan. *Proceedings of the Institution of Mechanical Engineers, Part A: Journal of Power and Energy*, 222(8):831–842, 2008.
- [38] R Ballesteros-Tajadura, S Velarde-Suárez, J. P. Hurtado-Cruz, and Carlos Santolaria-Morros. Numerical calculation of pressure fluctuations in the volute of a centrifugal fan. *Journal of Fluids Engineering, Transactions of the ASME*, 128(2):359–369, 2006.
- [39] X. Nogueira, S. Khelladi, I. Colominas, L. Cueto-Felgueroso, J. París, and H. Gómez. High-resolution finite volume methods on unstructured grids for turbulence and aeroacoustics. *Archives of Computational Methods in Engineering*, 18(3):315–340, 2011.
- [40] P. Traub, D. U. Broszat, J. Wellner, and T. Roeber. Exhaust (broadband) noise simulation of a realistic turbofan forced mixer by using a cfd/caa-approach. *American Institute of Aeronautics and Astronautics*, 2013.
- [41] H. Reese, T. Carolus, and C. Kato. Numerical prediction of the aeroacoustic sound sources in a low pressure axial fan with inflow distortion. *Fan conference: Fan Noise 2007*, 2007.
- [42] S. Magne, S. Moreau, and A. Berry. Subharmonic tonal noise from backflow vortices radiated by a low-speed ring fan in uniform inlet flow. *The Journal of the Acoustical Society of America*, 137(1):228, 2015.
- [43] J González, J Fernández, E Blanco, and C Santolaria. Numerical simulation of the dynamic effects due to impeller-volute interaction in a centrifugal pump. *Journal of Fluids Engineering, Transactions of the ASME*, 124(2):348–355, 2002.
- [44] Q. Liu, D. Qi, and Y. Mao. Numerical calculation of centrifugal fan noise. *Proceedings of the Institution of Mechanical Engineers*, 220(C8):1167–1177, 2006.
- [45] S. C. Lin and M. L. Tsai. An integrated performance analysis for a backward-inclined centrifugal fan. *Computers & Fluids*, 56:24–38, 2012.
- [46] R. Ballesteros-Tajadura, S. Velarde-Suarez, and J. P. Hurtado-Cruz. Noise prediction of a centrifugal fan: Numerical results and experimental validation. *Journal of Fluids Engineering*, 130(9):91102, 2008.
- [47] ANSYS Inc. Workshop for modeling flow-induced (aeroacoustic) noise, March 2013.
- [48] T. J. Coakley, P. G. Huang, and J. E. Bardina. Turbulence modelling validation, testing, and development. Technical report, NASA, 1997.
- [49] K. S. Brentner and F. Farassat. Analytical comparison of the acoustic analogy and kirchhoff formulation for moving surfaces. *AIAA Journal*, 36(8):1379–1386, 1998.
- [50] A. Zanon, M. De Gennaro, H. Kuehnelt, and D. Caridi. Broadband noise of axial fans: An experimental and computational benchmark study. *American Institute of Aeronautics and Astronautics*, 2013;.

A

Appendix 1

The first two sections involve solver settings used in all numerical simulations including Flow Courant Number, Explicit Relaxation Factors and Under Relaxation Factors. Followed by the closure coefficients used for the realizable $k - \varepsilon$ and $k - \omega$ SST turbulence models.

A.1 Flow Settings for Compressible Flow

The solver settings used when the flow was treated as compressible for both turbulence models are shown in Table A.1.

Table A.1: Solution controls for the compressible simulation cases for the two turbulence models.

	Realizable $k - \varepsilon$	$k - \omega$ SST
Flow Courant Number	200	200
Explicit Relaxation Factors		
Momentum	0.75	0.75
Pressure	0.75	0.75
Under Relaxation Factors		
Density	1	1
Body Forces	1	1
Turbulent Kinetic Energy	0.8	0.8
Turbulent Dissipation Rate	0.8	—
Specific Dissipation Rate	—	0.8
Turbulent Viscosity	0.8	0.8
Energy	1	1

A.2 Flow Settings for Incompressible Flow

The solver settings used when the flow was treated as incompressible for both turbulence models are shown in Table A.2.

Table A.2: Solution controls for the incompressible simulation cases for the two turbulence models.

	Realizable $k - \varepsilon$	$k - \omega$ SST
Flow Courant Number	200	200
Explicit Relaxation Factors		
Momentum	0.55	0.75
Pressure	0.55	0.75
Under Relaxation Factors		
Density	1	1
Body Forces	1	1
Turbulent Kinetic Energy	0.8	0.8
Turbulent Dissipation Rate	0.8	—
Specific Dissipation Rate	—	0.8
Turbulent Viscosity	0.8	0.8

A.3 Closure Coefficients

The closure coefficients used for the two turbulence models throughout the study are shown in Table A.3.

Table A.3: Closure coefficients used in the numerical simulations for the Realizable $k - \varepsilon$ turbulence model (left) and the $k - \omega$ SST turbulence model (right).

Realizable $k - \varepsilon$		$k - \omega$ SST	
Parameter	Value	Parameter	Value
$C_{\varepsilon,1}$	1.9	α_{∞}^*	1
σ_{ε}	1	α_{∞}	0.52
σ_k	1.2	β_{∞}^*	0.09
σ_E	0.85	a_1	0.31
σ_W	0.85	Inner β_i	0.075
		Outer β_i	0.0828
		Inner σ_{ε}	1.176
		Outer σ_{ε}	1
		Inner σ_{ω}	2
		Outer σ_{ω}	1.168
		σ_E	0.85
		σ_W	0.85
		Production Limiter	10